This is to certify that the
dissertation entitled

A MODE-MATCHING APPROACH TO DETERMINE
THE SHIELDING EFFECTIVENESS OF A
DOUBLY-PERIODIC ARRAY OF APERTURES IN A
THICK CONDUCTING SCREEN

presented by

DERIK CLAYTON LOVE

has been accepted towards fulfillment
of the requirements for the

Doctoral   degree in   Electrical Engineering

Edward J. Rothwell
Major Professor's Signature

12-16-04

Date

MSU is an Affirmative Action/Equal Opportunity Institution

PLACE IN RETURN BOX to remove this checkout from your record.
TO AVOID FINES return on or before date due.
MAY BE RECALLED with earlier due date if requested.

DATE DUE	DATE DUE	DATE DUE

A MODE-MATCHING APPROACH TO DETERMINE THE SHIELDING EFFECTIVENESS OF A DOUBLY-PERIODIC ARRAY OF APERTURES IN A THICK CONDUCTING SCREEN

By

Derik Clayton Love

A DISSERTATION

Submitted to
Michigan State University
in partial fulfillment of the requirements
for the degree of

DOCTOR OF PHILOSOPHY

Department of Electrical and Computer Engineering

2004

ABSTRACT

A MODE-MATCHING APPROACH TO DETERMINE THE SHIELDING EFFECTIVENESS OF A DOUBLY-PERIODIC ARRAY OF APERTURES IN A THICK CONDUCTING SCREEN

By

Derik Clayton Love

The transmission of electromagnetic waves through apertures in a conducting screen is a problem that has been examined many times before. Several techniques have been used when the apertures are periodically arranged, and computational approaches have allowed for the analysis of complex aperture shapes. However, past literature is typically concerned with screens whose thickness is comparable to or smaller than the aperture dimensions (i.e. thin screens). Further, the usual focus is on transmission within a narrow band of frequencies.

The shielding properties of planar, periodic structures have been considered in prior efforts. For a thick conducting screen of apertures, one approach for estimating the shielding effectiveness is to treat the screen as an array of cylindrical waveguides. This is referred to as the waveguide below cut-off principle. The result is dependent on the attenuation constant of the aperture and the aperture length. This technique is limited by the fact that it was developed to describe the attenuation of waves propagating in an opening whose length is at least five times its width. In addition, this approach is only relevant when the frequencies of interest are below the cut-off frequency of the dominant waveguide mode.

This dissertation uses mode-matching to determine the shielding effectiveness of a doubly-periodic conducting screen of apertures whose thickness can be several times the aperture size. This is accomplished by modeling the screen as an array of cylindrical waveguides. This study considers rectangular and circular apertures, and the

fields within them are represented using waveguide modal fields. The reflected wave above the screen and the transmitted wave below the screen are found by applying Floquet's Theorem, thereby exploiting the doubly-periodic nature of the screen of apertures. After enforcing boundary conditions and building a system of linear equations, the system is then truncated to produce a matrix equation which is solved using standard techniques. The shielding effectiveness of the screen is determined by comparing the transmitted power to the incident power carried by a plane wave. It is clear that as the thickness of the screen increases, the transmitted power is greatly reduced at frequencies below the cut-off frequency of the dominant waveguide mode. However, increasing the thickness also increases the attenuation of the higher-order waveguide modes, leading to non-convergent solutions to the matrix equation. By selectively eliminating higher-order modes from consideration, meaningful solutions are found. Results also show the effect of increasing the number of Floquet modes, varying the incidence angle, and changing the incident plane wave polarization.

The mode-matching results for rectangular apertures are very similar to data obtained by applying the waveguide below cut-off principle. However, the mode-matching approach can be used in cases where the frequencies of interest are above the cut-off frequncy of the dominant waveguide mode, when higher-order modes will begin to propagate. Comparisons are also made to previously published data using the mode-matching approach. The data curves are in strong agreement in each comparison. However, it should be noted that the previously published data considers the principal Floquet mode as the only propagating mode. That approach is inconsistent with the definition of the propagation constant for Floquet waves. Experimental data using commercial-grade aluminum honeycomb is also presented as another comparison for the mode-matching results. In each case, the curves are in good agreement in describing the transition from strong shield to weak shield.

For my two boys, Andrew and Malcolm

ACKNOWLEDGMENTS

I want to begin by acknowledging all of the guidance and support that has been provided to me by various individuals during my graduate studies here at Michigan State. I have never felt less than a tremendous amount of pride in the support that I have received within the EM research group, within the ECE department, and across the campus. I also want to thank all of the family, friends, colleagues and others that encouraged me to pursue a doctorate in order to achieve my career goals. In fact, a portion of my degree should go to my wife Amena. I can't imagine that I would have made it through this process without her supporting me in every way that she possibly could. Being a husband, father, and graduate student is busy work, but I could not have asked for a more supportive spouse.

To my guidance committee members, Dr. Edward Rothwell, Dr. Dennis Nyquist, Dr. Leo Kempel, and Dr. Byron Drachman, I want to thank you for doing just that: guiding me. I am looking forward to a long and productive career as a researcher and possibly as a teacher, and I know that my interest in both has been advanced by my experiences in your classrooms, office hour sessions, etc. Before arriving at MSU, I was told by a former co-worker that studying electromagnetics at Michigan State is special because of the people, and I completely agree. I also want to thank the faculty and staff of the ECE department, in particular Dr. Percy Pierre and Dr. Barbara O'Kelly. Their intial interest in me is what attracted me to MSU, and their constant pledge of financial and career development support is what kept me here and helped me through. NASA Goddard Space Flight Center has been instrumental

TABLE OF CONTENTS

LIST OF TABLES

LIST OF FIGURES

CHAPTER 1

INTRODUCTION

The transmission of electromagnetic waves through apertures in a conducting screen is a problem that has been examined many times before [1]-[4]. Several techniques have been used when the apertures are periodically arranged [5]-[12], and computational approaches have allowed for the analysis of complex aperture shapes [13]-[19]. However, past literature is typically concerned with screens whose thickness is comparable to or smaller than the aperture dimensions (i.e. thin screens). Further, the usual focus is on transmission within a narrow band of frequencies.

The shielding properties of planar, periodic structures have been considered in prior efforts [20]-[22]. For a thick conducting screen of apertures, one approach for estimating the shielding effectiveness is to treat the screen as an array of cylindrical waveguides. This is referred to as the waveguide below cut-off principle [23]. The result is dependent on the attenuation constant of the aperture and the aperture length. This technique is limited by the fact that it was developed to describe the attenuation of waves propagating in an opening whose length is at least five times its width [24]. In addition, this approach is only relevant when the frequencies of interest are below the cut-off frequency of the dominant waveguide mode.

This dissertation uses mode-matching to determine the shielding effectiveness of a doubly-periodic conducting screen of apertures whose thickness can be several times the aperture size. This is accomplished by modelling the screen as an array of cylindrical waveguides. This study considers rectangular and circular apertures, and the fields within them are represented using waveguide modal fields. The reflected wave above the screen and the transmitted wave below the screen are found by applying Floquet's Theorem, thereby exploiting the doubly-periodic nature of the screen of

apertures. After enforcing boundary conditions and building a system of linear equations, the system is then truncated to produce a matrix equation which is solved using standard techniques. The shielding effectiveness of the screen is determined by comparing the transmitted power to the incident power carried by a plane wave. It is clear that as the thickness of the screen increases, the transmitted power is greatly reduced at frequencies below the cut-off frequency of the dominant waveguide mode. However, increasing the thickness also increases the attenuation of the higher-order waveguide modes, leading to non-convergent solutions to the matrix equation. By selectively eliminating higher-order modes from consideration, meaningful solutions are found. Results also show the effect of increasing the number of Floquet modes, varying the incidence angle, and changing the incident plane wave polarization.

The mode-matching results for rectangular apertures are very similar to data obtained by applying the waveguide below cut-off principle. However, the mode-matching approach can be used in cases where the frequencies of interest are above the cut-off frequncy of the dominant waveguide mode, when higher-order modes will begin to propagate. Comparisons are also made to previously published data using the mode-matching approach. The data curves are in strong agreement in each comparison. However, it should be noted that the previously published data considers the principal Floquet mode as the only propagating mode. That approach is inconsistent with the definition of the propagation constant for Floquet waves. Experimental data using commercial-grade aluminum honeycomb is also presented as another comparison for the mode-matching results. In each case, the curves are in good agreement in describing the transition from strong shield to weak shield.

This dissertation describes all of the theoretical, numerical, and experimental investigations involved in this study. Chapter 2 outlines the theory, including derivations of fields produced both by the Floquet waves and within the apertures. Also included is a detailed description of the enforcement of boundary conditions on the

electric and magnetic fields, and a full explanation of how the boundary conditions were used to create a system of linear equations. Finally, the computation of shielding effectiveness will be shown. Chapter 3 outlines calculations and numerical results for both rectangular and circular apertures, including computation of the integral expressions that are described in Chapter 2. The experimental set-up and results are discussed in Chapter 4. An open set-up using horn antennas and a network analyzer was used to conduct shielding measurements on samples of aluminum honeycomb. The results confirmed the general behavior versus frequency that was expected. Chapter 5 discusses the considerations that were made in order to obtain the numerical results in Chapter 3. This involves the truncation of the matrix equation in order to solve for the unknowns. Most important was the observation that as the thickness of the screen increased, the number of waveguide modes had to be reduced in order to get convergent solutions to the matrix equation. The remaining chapters include conclusions, references, and appendices for techniques that were critical to the development of the theory.

Mode-matching applied to thin screens is not a new technique, and neither is computing and/or measuring shielding effectiveness. However, using mode-matching to determine the shielding effectiveness of thick screens across a wide range of frequencies is a new direction. To the author's knowledge, the comparison of mode-matching numerical results to experimental data for aluminum honeycomb has not been done until now. Also, the use of styrofoam boards covered in foil tape to analyze the honeycomb samples is a new approach, but similar to using large metal plates with an aperture to analyze composite materials.

CHAPTER 2

THEORETICAL FORMULATION

2.1 Floquet Waves

The layout of a screen of apertures is shown in Figure 2.1. It is considered to be of infinite extent in the x and y directions and have thickness t in the z direction. The screen contains apertures that are arranged in a doubly-periodic fashion, with the first axis of periodicity being the x-axis and the second making an angle ϕ_0 with respect to the x-axis. From Figure 2.1, the screen has a periodicity of c along the x-axis and d along the skewed axis. By representing the screen as an array of cylindrical waveguides, each element of the array is represented by a cell and the center element is regarded as the unit cell. The unit cell (S) is composed of two regions, the aperture region (Ω) and the conducting region $(S-\Omega)$, as shown in Figure 2.2 (Note: Although the figure shows a rectangular unit cell, there are other possible choices for the unit cell geometry; the rectangular cell is used as an example to graphically indicate S and Ω). A plane wave is incident on the screen with wave vector $\boldsymbol{k^i} = \hat{x}k_x^i + \hat{y}k_y^i - \hat{z}k_z^i$, where

$$k_x^i = k_1 \sin \theta_i \cos \phi_i,$$

$$k_y^i = k_1 \sin \theta_i \sin \phi_i,$$

$$k_z^i = k_1 \cos \theta_i,$$

$$k_1 = \omega\sqrt{(\mu_1 \epsilon_1)},$$

and ϵ_1 and μ_1 are the permittivity and permeability, respectively, in region I $(z > 0)$. Similarly, ϵ_2 and μ_2 are the permittivity and permeability in region II $(-t < z < 0)$, and ϵ_3 and μ_3 are the permittivity and permeability in region III $(z < -t)$. The

azimuthal angle ϕ_i is measured from the positive x-axis toward the positive y-axis, while the zenith angle θ_i is measured from the positive z-axis toward the negative z-axis.

If regions I, II, and III are assumed source-free, the fields in each region can be expressed using a TE/TM decomposition of the fields [25]. Furthermore, Hertzian potential functions can be used to determine the fields while still maintaining the wave nature of the solution [25]. The Hertzian potentials that are used are

$$\mathbf{\Pi}_e(x, y, z) = \hat{z}\Pi_e(x, y, z) \qquad \text{(TM}_z \text{ Case)},$$

$$\mathbf{\Pi}_h(x, y, z) = \hat{z}\Pi_h(x, y, z) \qquad \text{(TE}_z \text{ Case)}.$$

Due to the longitudinal nature of the potentials, their satisfaction of the wave equation simplifies to only requiring the scalar component to satisfy the scalar Helmholtz equation [25], or

$$(\nabla^2 + k^2)\Pi_{eh} = 0.$$

The fields due to the potentials are

$$\boldsymbol{E} = \nabla_t \frac{\partial \Pi_e}{\partial z} + \hat{z}\left(\frac{\partial^2}{\partial z^2} + k^2\right)\Pi_e + j\omega\mu\hat{z} \times \nabla_t\Pi_h, \qquad (2.1)$$

$$\boldsymbol{H} = \nabla_t \frac{\partial \Pi_h}{\partial z} + \hat{z}\left(\frac{\partial^2}{\partial z^2} + k^2\right)\Pi_h - j\omega\epsilon\hat{z} \times \nabla_t\Pi_e, \qquad (2.2)$$

where

$$\nabla_t = \nabla - \hat{z}\frac{\partial}{\partial z},$$

$$k^2 = \omega^2\mu\epsilon,$$

so that $k_1^2 = \omega^2\mu_1\epsilon_1$ and $k_3^2 = \omega^2\mu_3\epsilon_3$.

Because of the doubly-periodic nature of the array of apertures and the plane

wave excitation, the potentials in regions I and III must obey Floquet's Theorem, such that

$$\Pi_{eh}(x, y, z) = e^{-jk_x^i x} e^{-jk_y^i y} \Pi_{eh}^P(x, y, z).$$

Using the results from Appendix A, Π_{eh}^P can be expanded in a Fourier series such that

$$\Pi_{eh}^P(x, y, z) = \sum_{m,n=-\infty}^{\infty} \Pi_{ehmn}(z) e^{-j\frac{2\pi m}{c} x} e^{-j\frac{2\pi n}{d} \csc \phi_0 y + j\frac{2\pi m}{c} \cot \phi_0 y}.$$

Using this, Π_{eh} can be rewritten as

$$
\begin{aligned}
\Pi_{eh}(x, y, z) &= e^{-jk_x^i x} e^{-jk_y^i y} \Pi_{eh}^P(x, y, z) \\
&= \sum_{m,n=-\infty}^{\infty} \Pi_{ehmn}(z) e^{-j(\frac{2\pi m}{c} + k_x^i)x} e^{-j(\frac{2\pi n}{d} \csc \phi_0 - \frac{2\pi m}{c} \cot \phi_0 + k_y^i)y} \\
&= \sum_{m,n=-\infty}^{\infty} \Pi_{ehmn}(z) e^{-j\alpha_m x} e^{-j\beta_{mn} y}
\end{aligned}
\tag{2.3}
$$

where

$$\alpha_m = \frac{2\pi m}{c} + k_x^i, \tag{2.4}$$

$$\beta_{mn} = \frac{2\pi n}{d} \csc \phi_0 - \frac{2\pi m}{c} \cot \phi_0 + k_y^i, \tag{2.5}$$

and the indices m and n are the Floquet mode indices. Substituting Π_{eh} into the Helmholtz equation leads to

$$
\begin{aligned}
(\nabla^2 + k^2)\Pi_{eh} &= \left(\frac{\partial^2}{\partial x^2} + \frac{\partial^2}{\partial y^2} + \frac{\partial^2}{\partial z^2} + k^2 \right) \Pi_{eh} \\
&= \sum_{m,n=-\infty}^{\infty} \left(-\alpha_m^2 - \beta_{mn}^2 + k^2 + \frac{\partial^2}{\partial z^2} \right) \Pi_{ehmn}(z) e^{-j\alpha_m x} e^{-j\beta_{mn} y} \\
&= 0.
\end{aligned}
\tag{2.6}
$$

If a function $F_{mn}(z)$ is defined such that

$$F_{mn}(z) = \left(-\alpha_m^2 - \beta_{mn}^2 + k^2 + \frac{\partial^2}{\partial z^2}\right) \Pi_{ehmn}(z),$$

(2.6) can be rewritten as

$$\sum_{m,n=-\infty}^{\infty} F_{mn}(z)e^{-j\alpha_m x}e^{-j\beta_{mn}y} = 0. \tag{2.7}$$

The orthogonality of the exponentials can be used to simplify (2.7) by removing the infinite summations. This is done by multiplying (2.7) by another pair of exponential expressions and integrating over the unit cell region over which the Floquet waves are defined. This leads to

$$\int_S e^{j\alpha_a x}e^{j\beta_{ab}y}\left[\sum_{m,n=-\infty}^{\infty} F_{mn}(z)e^{-j\alpha_m x}e^{-j\beta_{mn}y}\right]ds = 0. \tag{2.8}$$

Interchanging the order of summation and integration, (2.8) becomes

$$\sum_{m,n=-\infty}^{\infty} F_{mn}(z)\left[\int_S e^{j(\alpha_a - \alpha_m)x}e^{j(\beta_{ab} - \beta_{mn})y}ds\right] = 0. \tag{2.9}$$

The orthogonality of the exponentials allows the integral in (2.9) to be evaluated such that

$$\int_S e^{j(\alpha_a - \alpha_m)x}e^{j(\beta_{ab} - \beta_{mn})y}ds = A_s\delta_{am}\delta_{bn},$$

where A_s is the area of the unit cell, and δ is the Kronecker delta function [26]. Rewriting (2.9) once more leads to

$$A_s\sum_{m,n=-\infty}^{\infty} \delta_{am}\delta_{bn}F_{mn}(z) = A_sF_{mn}(z) = 0.$$

With A_s being a constant and assumed not equal to zero, it follows that

$$F_{mn}(z) = \left(-\alpha_m^2 - \beta_{mn}^2 + k^2 + \frac{\partial^2}{\partial z^2}\right)\Pi_{ehmn}(z) = 0,$$

or

$$\left(\Gamma_{mn}^2 + \frac{\partial^2}{\partial z^2}\right)\Pi_{ehmn}(z) = 0, \qquad (2.10)$$

where

$$\Gamma_{mn}^2 = k^2 - \alpha_m^2 - \beta_{mn}^2.$$

The solution to the ordinary differential equation in (2.10) is

$$\Pi_{ehmn}(z) = a_{ehmn}^+ e^{-j\Gamma_{mn}z} + a_{ehmn}^- e^{+j\Gamma_{mn}z},$$

which represents waves either propagating or evanescent in the +z and -z directions. The potential expression in (2.3) can now be rewritten as

$$\Pi_{eh}(x,y,z) = \sum_{m,n=-\infty}^{\infty} a_{ehmn}^- e^{-j\alpha_m x} e^{-j\beta_{mn}y} e^{+j\Gamma_{mn}^{(3)}z}$$

when $z < -t$, and

$$\Pi_{eh}(x,y,z) = \sum_{m,n=-\infty}^{\infty} a_{ehmn}^+ e^{-j\alpha_m x} e^{-j\beta_{mn}y} e^{-j\Gamma_{mn}^{(1)}z}$$

when $z > 0$, where

$$\Gamma_{mn}^{(1)\,2} = k_1^2 - \alpha_m^2 - \beta_{mn}^2,$$

$$\Gamma_{mn}^{(3)\,2} = k_3^2 - \alpha_m^2 - \beta_{mn}^2,$$

and $k_1 = \omega\sqrt{(\mu_1\epsilon_1)}$ and $k_3 = \omega\sqrt{(\mu_3\epsilon_3)}$ represent the wave number in regions I and III, respectively. Also, the coefficients a_{ehmn}^+ and a_{ehmn}^- represent the complex Floquet

wave coefficients in regions I and III, respectively. Two observations are made here. The first is that the sign of $\sqrt{\Gamma_{mn}^2}$ must be chosen such that

$$\Re\left\{\sqrt{\Gamma_{mn}^2}\right\} > 0 \quad \text{and} \quad \Im\left\{\sqrt{\Gamma_{mn}^2}\right\} < 0$$

to ensure that propagating Floquet modes propagate away from the screen and evanescent Floquet waves in each region decay away from the screen. The second observation is that the potential expressions can be rewritten as

$$\Pi_{eh} = \sum_{m,n=-\infty}^{\infty} a_{ehmn}^{-} e^{-j\boldsymbol{\tau}_{mn} \cdot \boldsymbol{r}} e^{+j\Gamma_{mn}^{(3)} z} \tag{2.11}$$

when $z < -t$, and

$$\Pi_{eh} = \sum_{m,n=-\infty}^{\infty} a_{ehmn}^{+} e^{-j\boldsymbol{\tau}_{mn} \cdot \boldsymbol{r}} e^{-j\Gamma_{mn}^{(1)} z} \tag{2.12}$$

when $z > 0$, where $\boldsymbol{\tau}_{mn} = \hat{x}\alpha_m + \hat{y}\beta_{mn}$ and $\boldsymbol{r} = \hat{x}x + \hat{y}y + \hat{z}z$.

The Floquet wave fields will be matched to fields within a waveguide whose longitudinal axis is the z-axis, and thus only the transverse components of the electric and magnetic fields will be needed. The transverse electric field is taken from (2.1) as

$$\boldsymbol{E}_t = \nabla_t \frac{\partial \Pi_e}{\partial z} + j\omega\mu\hat{z} \times \nabla_t \Pi_h, \tag{2.13}$$

while the transverse magnetic field is taken from (2.2) as

$$\boldsymbol{H}_t = \nabla_t \frac{\partial \Pi_h}{\partial z} - j\omega\epsilon\hat{z} \times \nabla_t \Pi_e. \tag{2.14}$$

With complete expressions for the Hertzian potentials in regions I and III, the electric and magnetic field expressions for both regions can be determined. Substituting (2.11)

and (2.12) into (2.13) leads to the electric field, which is

$$
\boldsymbol{E}_t^{\overset{(1)}{(3)}} = \sum_{m,n=-\infty}^{\infty} \left[\mp a_{emn}^{\pm} \Gamma_{mn}^{\overset{(1)}{(3)}} \boldsymbol{\tau}_{mn} - \omega \mu_{\overset{(1)}{(3)}} a_{hmn}^{\pm} (\boldsymbol{\tau}_{mn} \times \hat{z}) \right] e^{\mp j \Gamma_{mn}^{\overset{(1)}{(3)}} z} e^{-j\boldsymbol{\tau}_{mn} \cdot \boldsymbol{r}}.
$$

Similarly, the magnetic field can be found by substituting (2.11) and (2.12) into (2.14), which leads to

$$
\boldsymbol{H}_t^{\overset{(1)}{(3)}} = \sum_{m,n=-\infty}^{\infty} \left[\mp a_{hmn}^{\pm} \Gamma_{mn}^{\overset{(1)}{(3)}} \boldsymbol{\tau}_{mn} + \omega \epsilon_{\overset{(1)}{(3)}} a_{emn}^{\pm} (\boldsymbol{\tau}_{mn} \times \hat{z}) \right] e^{\mp j \Gamma_{mn}^{\overset{(1)}{(3)}} z} e^{-j\boldsymbol{\tau}_{mn} \cdot \boldsymbol{r}}.
$$

In cases where signs, subscripts, and/or superscripts are stacked, the upper signs, subscripts and superscripts correspond to region I ($z > 0$), while the lower signs, subscripts and superscripts correspond to region III ($z < -t$). Making some substitutions for constants and taking $\hat{z} \times \boldsymbol{H}_t$, the transverse electric and magnetic fields can be expressed as

$$
\boldsymbol{E}_t = \sum_{m,n=-\infty}^{\infty} \left[\mp A_{emn}^{\pm} \boldsymbol{R}_{2mn}^{\pm} - A_{hmn}^{\pm} \boldsymbol{R}_{1mn}^{\pm} \right], \tag{2.15}
$$

$$
\hat{z} \times \boldsymbol{H}_t = \sum_{m,n=-\infty}^{\infty} \left[\pm A_{hmn}^{\pm} Y_h^{\overset{(1)}{(3)}} \boldsymbol{R}_{1mn}^{\pm} + A_{emn}^{\pm} Y_e^{\overset{(1)}{(3)}} \boldsymbol{R}_{2mn}^{\pm} \right], \tag{2.16}
$$

where

$$
A_{emn}^{\pm} = a_{emn}^{\pm} \Gamma_{mn}^{\overset{(1)}{(3)}} \tau_{mn} \sqrt{A_s},
$$

$$
A_{hmn}^{\pm} = \omega \mu_{\overset{(1)}{(3)}} a_{hmn}^{\pm} \tau_{mn} \sqrt{A_s},
$$

$$
\boldsymbol{R}_{2mn}^{\pm} = \hat{\tau}_{mn} R_{mn}^{\pm} = \boldsymbol{R}_{2mn} e^{\mp j \Gamma_{mn}^{\overset{(1)}{(3)}} z},
$$

$$
\boldsymbol{R}_{1mn}^{\pm} = (\hat{\tau}_{mn} \times \hat{z}) R_{mn}^{\pm} = \boldsymbol{R}_{1mn} e^{\mp j \Gamma_{mn}^{\overset{(1)}{(3)}} z},
$$

$$R_{mn}^{\pm} = \frac{1}{\sqrt{A_s}} e^{\mp j \overset{(1)}{\underset{(3)}{\Gamma}}_{mn} z} e^{-j\boldsymbol{\tau}_{mn} \cdot \boldsymbol{r}} = R_{mn} e^{\mp j \overset{(1)}{\underset{(3)}{\Gamma}}_{mn} z},$$

$$R_{mn} = \frac{1}{\sqrt{A_s}} e^{-j\boldsymbol{\tau}_{mn} \cdot \boldsymbol{r}},$$

$$\boldsymbol{R}_{1mn} = (\hat{\tau}_{mn} \times \hat{z}) R_{mn}, \qquad (2.17)$$

$$\boldsymbol{R}_{2mn} = \hat{\tau}_{mn} R_{mn}, \qquad (2.18)$$

$$\hat{\tau}_{mn} = \frac{\boldsymbol{\tau}_{mn}}{\tau_{mn}},$$

$$\tau_{mn} = |\boldsymbol{\tau}_{mn}| = \sqrt{\alpha_m^2 + \beta_{mn}^2},$$

and the wave admittances are given by

$$\overset{(1)}{\underset{h}{Y}_e^{(3)}} = \frac{\omega \epsilon \overset{(1)}{\underset{(3)}{}}}{\overset{(1)}{\underset{(3)}{\Gamma}}_{mn}},$$

$$\overset{(1)}{\underset{h}{Y}_h^{(3)}} = \frac{\overset{(1)}{\underset{(3)}{\Gamma}}_{mn}}{\omega \mu \overset{(1)}{\underset{(3)}{}}}.$$

2.2 Waveguide Fields

2.2.1 Modal Fields

To determine the fields within the screen, a modal expansion will be performed using Hertzian potentials. The Hertzian potentials used for this expansion are

$$\boldsymbol{\Pi}_{ep}(x, y, z) = \hat{z}\Pi_{ep}(x, y, z) \qquad (\text{TM}_z \text{ Case}),$$

$$\boldsymbol{\Pi}_{hp}(x, y, z) = \hat{z}\Pi_{hp}(x, y, z) \qquad (\text{TE}_z \text{ Case}),$$

where p is an index to represent a particular waveguide mode. Due to their longitudinal nature, these potentials must satisfy the scalar Helmholtz equation, or

$$(\nabla^2 + k_2^2)\Pi_{ehp} = 0, \tag{2.19}$$

where $k_2^2 = \omega^2 \mu_2 \epsilon_2$, and ϵ_2 and μ_2 represent the permittivity and permeability, respectively, in the aperture regions within the screen (region II). The waveguide modal electric and magnetic fields in terms of the Hertzian potentials are

$$\boldsymbol{E}_p = \nabla_t \frac{\partial \Pi_{ep}}{\partial z} + \hat{z}\left(\frac{\partial^2}{\partial z^2} + k_2^2\right)\Pi_{ep} + j\omega\mu_2\hat{z} \times \nabla_t\Pi_{hp}, \tag{2.20}$$

$$\boldsymbol{H}_p = \nabla_t \frac{\partial \Pi_{hp}}{\partial z} + \hat{z}\left(\frac{\partial^2}{\partial z^2} + k_2^2\right)\Pi_{hp} - j\omega\epsilon_2\hat{z} \times \nabla_t\Pi_{ep}. \tag{2.21}$$

The separation of variables technique can be used to express the solutions to (2.19) as [25]

$$\Pi_{ep} = \psi_{ep}(x, y)e^{\mp jk_z z},$$

$$\Pi_{hp} = \psi_{hp}(x, y)e^{\mp jk_z z},$$

where the mode functions ψ_{ep} and ψ_{hp} must satisfy

$$\nabla_t^2 \psi_{ehp} + k_c^2 \psi_{ehp} = 0, \tag{2.22}$$

and

$$k_c^2 = k_2^2 - k_z^2. \tag{2.23}$$

To complete the satisfaction of the Helmholtz equation, $Z(z) = e^{\mp jk_z z}$ satisfies

$$\frac{\partial^2 Z}{\partial z^2} + k_z^2 Z = 0.$$

As was the case with the Floquet wave derivation, the fields of interest within the waveguide are the fields transverse to the direction of wave travel, or the fields transverse to the longitudinal axis of the waveguide, which is the z-axis. Therefore, (2.20) and (2.21) can be used to obtain the transverse fields as

$$\boldsymbol{E}_{tp} = \nabla_t \frac{\partial \Pi_{ep}}{\partial z} + j\omega\mu_2 \hat{z} \times \nabla_t \Pi_{hp}, \tag{2.24}$$

$$\boldsymbol{H}_{tp} = \nabla_t \frac{\partial \Pi_{hp}}{\partial z} - j\omega\epsilon_2 \hat{z} \times \nabla_t \Pi_{ep}. \tag{2.25}$$

For the TM_z case, the potential Π_{ep} can be used in (2.24) and (2.25) to express the modal transverse field components as

$$\boldsymbol{E}_{tp} = \mp \boldsymbol{e}_{tp} e^{\mp jk_z z}, \tag{2.26}$$

$$\boldsymbol{H}_{tp} = -Y_{ep}(\hat{z} \times \boldsymbol{e}_{tp}) e^{\mp jk_z z}, \tag{2.27}$$

where

$$\boldsymbol{e}_{tp}(x, y) = jk_z \nabla_t \psi_{ep}(x, y), \tag{2.28}$$

and the complex wave admittance is

$$Y_{ep} = \frac{\omega\epsilon_2}{k_z}. $$

A modal expansion of the total transverse electric field within the waveguide in terms of sinusoidal functions and complex coefficients A_p and B_p leads to

$$\boldsymbol{E}_t^T = \sum_p [A_p \sin(k_z z) + B_p \cos(k_z z)] \boldsymbol{E}_{tp} \tag{2.29}$$

13

where

$$E_{tp} = \frac{e_{tp}}{\sqrt{f_{pe}}},$$

$$f_{pe} = \int_{\Omega} e_{tp} \cdot e_{tp} \, ds, \tag{2.30}$$

and f_{pe} is used to make the modal fields orthonormal. For a modal expansion of the transverse magnetic field ($\hat{z} \times H_t^T$), (2.26) and (2.27) can be used to reason that

$$j\omega\epsilon_2 E_t^T = \frac{\partial}{\partial z}[\hat{z} \times H_t^T]. \tag{2.31}$$

This is accomplished by taking the cross product of $\hat{z}$ and H_{tp}, and then taking a derivative with respect to z such that

$$\begin{aligned}
\frac{\partial}{\partial z}(\hat{z} \times H_{tp}) &= \frac{\partial}{\partial z}\left(-Y_{ep}(\hat{z} \times \hat{z} \times e_{tp})e^{\mp jk_z z}\right) \\
&= \frac{\partial}{\partial z}\left(\frac{\omega\epsilon_2}{k_z}e_{tp}e^{\mp jk_z z}\right) \\
&= \mp j\omega\epsilon_2 e_{tp}e^{\mp jk_z z} \\
&= j\omega\epsilon_2 E_{tp}.
\end{aligned}$$

Substituting (2.29) into (2.31) leads to

$$\begin{aligned}
j\omega\epsilon_2 E_t^T &= j\omega\epsilon_2 \sum_p [A_p \sin(k_z z) + B_p \cos(k_z z)]E_{tp} \\
&= \sum_p j\frac{\omega\epsilon_2}{k_z}k_z[A_p \sin(k_z z) + B_p \cos(k_z z)]E_{tp} \\
&= \frac{1}{\eta_2}\sum_p j\frac{k_2}{k_z}k_z[A_p \sin(k_z z) + B_p \cos(k_z z)]E_{tp} \\
&= \frac{\partial}{\partial z}[\hat{z} \times H_t^T]
\end{aligned}$$

where η_2 represents the intrinsic impedance in region II. The solution for $\hat{z} \times \boldsymbol{H}_t^T$ is

$$\hat{z} \times \boldsymbol{H}_t^T = -\frac{1}{\eta_2} \sum_p j \frac{k_2}{k_z} [A_p \cos(k_z z) - B_p \sin(k_z z)] \boldsymbol{E}_{tp}. \qquad (2.32)$$

For TE modes, a similar approach can be used to determine the fields. Π_{hp} can be used in (2.20) and (2.21) to express the modal transverse field components as

$$\boldsymbol{H}_{tp} = \mp \boldsymbol{h}_{tp} e^{\mp j k_z z}, \qquad (2.33)$$

$$\boldsymbol{E}_{tp} = Z_{hp}(\hat{z} \times \boldsymbol{h}_{tp}) e^{\mp j k_z z}, \qquad (2.34)$$

where

$$\boldsymbol{h}_{tp}(x, y) = j k_z \nabla_t \psi_{hp}(x, y), \qquad (2.35)$$

and the complex wave impedance is

$$Z_{hp} = \frac{\omega \mu_2}{k_z}.$$

The modal expansion for the total transverse electric field is

$$\boldsymbol{E}_t^T = \sum_p [C_p \sin(k_z z) + D_p \cos(k_z z)] \boldsymbol{E}_{tp} \qquad (2.36)$$

where

$$\boldsymbol{E}_{tp} = \frac{Z_{hp}(\hat{z} \times \boldsymbol{h}_{tp})}{\sqrt{f_{ph}}},$$

$$f_{ph} = \int_\Omega Z_{hp}(\hat{z} \times \boldsymbol{h}_{tp}) \cdot Z_{hp}(\hat{z} \times \boldsymbol{h}_{tp}) \, ds, \qquad (2.37)$$

C_p and D_p are complex coefficients for the TE modes, and f_{ph} is used to make the fields orthonormal. To obtain the magnetic field expansion, it can be shown using

(2.33) and (2.34) that

$$
j\omega\mu_2 \left(\hat{z} \times \boldsymbol{H}_t^T \right) = \frac{\partial}{\partial z}(\boldsymbol{E}_t^T).
\tag{2.38}
$$

This is accomplished by taking the cross product of $\hat{z}$ and $\boldsymbol{H}_{tp}$, and then multiplying by $j\omega\mu$ such that

$$
\begin{aligned}
j\omega\mu_2 \left(\hat{z} \times \boldsymbol{H}_{tp} \right) &= j\omega\mu_2 \left(\hat{z} \times \left(\mp h_{tp} e^{\mp jk_z z} \right) \right) \\
&= \mp j\omega\mu_2 \left(\hat{z} \times h_{tp} \right) e^{\mp jk_z z} \\
&= \mp j \frac{\omega\mu_2}{Z_{hp}} \boldsymbol{E}_{tp} \\
&= \mp j k_z \boldsymbol{E}_{tp} \\
&= \frac{\partial}{\partial z} \left(\boldsymbol{E}_{tp} \right).
\end{aligned}
$$

Substituting (2.36) into (2.38) leads to

$$
\begin{aligned}
\frac{\partial}{\partial z}(\boldsymbol{E}_t^T) &= \frac{\partial}{\partial z} \sum_p [C_p \sin(k_z z) + D_p \cos(k_z z)] \boldsymbol{E}_{tp} \\
&= \sum_p k_z [C_p \cos(k_z z) - D_p \sin(k_z z)] \boldsymbol{E}_{tp} \\
&= j\omega\mu_2 \left(\hat{z} \times \boldsymbol{H}_t^T \right).
\end{aligned}
$$

The solution for $\hat{z} \times \boldsymbol{H}_t^T$ is

$$
\begin{aligned}
\hat{z} \times \boldsymbol{H}_t^T &= \frac{-j}{\omega\mu_2} \sum_p k_z [C_p \cos(k_z z) - D_p \sin(k_z z)] \boldsymbol{E}_{tp} \\
&= \frac{-j}{k_2 \eta_2} \sum_p k_z [C_p \cos(k_z z) - D_p \sin(k_z z)] \boldsymbol{E}_{tp} \\
&= \frac{-1}{\eta_2} \sum_p j \frac{k_z}{k_2} [C_p \cos(k_z z) - D_p \sin(k_z z)] \boldsymbol{E}_{tp}.
\end{aligned}
\tag{2.39}
$$

2.2.2 Mode Functions for Rectangular Waveguides

For the case involving rectangular apertures, the screen is modeled as an array of rectangular waveguides. Many textbooks have analyzed the rectangular waveguide,

including [25]-[27]. Some details of determining the mode functions are repeated here.

Consider a rectangular aperture defined such that $-\frac{a}{2} \leq x \leq \frac{a}{2}$ and $-\frac{b}{2} \leq y \leq \frac{b}{2}$, and filled with a material with permittivity ϵ_2 and permeability μ_2. To properly represent the fields within the aperture, the mode functions ψ_{ep} and ψ_{hp} must satisfy (2.22) and (2.23). In addition, each mode function must also satisfy the appropriate boundary condition. For TM modes, that is the homogeneous Dirichlet boundary condition, or

$$\psi_{ep} = \psi_{ep}(x, y) = 0, \qquad x, y \in \Gamma,$$

where Γ is the contour defining the boundary of the waveguide. Also, the index p refers to the pth mode, whether it is a TM or TE mode. The well-known result is that ψ_{ep} can be represented as

$$\psi_{ep} = \sin\left[k_x\left(x + \frac{a}{2}\right)\right] \sin\left[k_y\left(y + \frac{b}{2}\right)\right], \qquad (2.40)$$

where

$$k_x = \frac{m\pi}{a}, \qquad m = 1, 2, 3, \ldots$$
$$k_y = \frac{n\pi}{b}, \qquad n = 1, 2, 3, \ldots$$

and

$$k_c^2 = k_2^2 - k_z^2 = k_x^2 + k_y^2.$$

Just to clarify, the index p refers to the pth mode combination of the indices m and n for TM and TE modes.

For TE modes the requirement is satisfaction of the homogeneous Neumann

boundary condition, or

$$\frac{\partial \psi_{hp}}{\partial n} = \frac{\partial \psi_{hp}}{\partial n}(x,y) = 0, \qquad x, y \in \Gamma,$$

where n is the variable for the normal direction to Γ. The well-known result is that ψ_{hp} can be represented as

$$\psi_{hp} = \cos\left[k_x\left(x + \frac{a}{2}\right)\right] \cos\left[k_y\left(y + \frac{b}{2}\right)\right], \qquad (2.41)$$

where

$$k_x = \frac{m\pi}{a}, \qquad m = 0, 1, 2, 3, \dots$$
$$k_y = \frac{n\pi}{b}, \qquad n = 0, 1, 2, 3, \dots$$

and

$$k_c^2 = k_2^2 - k_z^2 = k_x^2 + k_y^2.$$

Also, m and n cannot be simultaneously equal to zero for TE modes.

2.2.3 Mode Functions for Circular Waveguides

For the case involving circular apertures, the screen is modeled as an array of circular waveguides. Many textbooks have analyzed the circular waveguide, including [28][27]. Some details of determining the mode functions are repeated here.

Consider a circular aperture defined such that $0 \le r \le a$, and filled with a material with permittivity ϵ_2 and permeability μ_2. To properly represent the fields within the aperture, the mode functions ψ_{ep} and ψ_{hp} must satisfy (2.22) and (2.23). In addition, each mode function must also satisfy the appropriate boundary condition. To satisfy the homogeneous Dirichlet boundary condition for TM modes, the well-known result

is to define ψ_{ep} as

$$\psi_{ep} = J_c\left(\frac{\chi_{cd}}{a}r\right)[A_c\cos(c\phi) + B_c\sin(c\phi)], \qquad (2.42)$$

where χ_{cd} is the dth zero of the cth order Bessel function of the first kind. Also,

$$k_c^2 = k_2^2 - k_z^2 = k_r^2,$$

$$k_r = \frac{\chi_{cd}}{a}.$$

To satisfy the homogeneous Neumann boundary condition for TE modes, the well-known result is to define ψ_{hp} as

$$\psi_{hp} = J_c\left(\frac{\chi'_{cd}}{a}r\right)[A_c\cos(c\phi) + B_c\sin(c\phi)], \qquad (2.43)$$

where χ'_{cd} is the dth zero of the derivative of the cth order Bessel function of the first kind. Also,

$$k_{cmn}^2 = k_2^2 - k_{zmn}^2 = {k'_{rmn}}^2,$$

$$k'_r = \frac{\chi'_{cd}}{a}.$$

2.3 Enforcement of Boundary Conditions

In order to relate the Floquet wave and waveguide coefficients, boundary conditions are enforced at the upper and lower surfaces of the screen, which correspond to $z = 0$ and $z = -t$, respectively. This is accomplished by taking the transverse field expressions and equating them at the boundaries. Using (2.15), (2.29), and (2.36), the continuity of transverse electric field within the aperture region leads to

$$\boldsymbol{E}_t^i + \sum_{m,n}\left[-A_{emn}^+\boldsymbol{R}_{2mn} - A_{hmn}^+\boldsymbol{R}_{1mn}\right] = \sum_p G_p\boldsymbol{E}_{tp}, \qquad \boldsymbol{r} \in \Omega \qquad (2.44)$$

19

when $z = 0$ and

$$\sum_{m,n} \left[A^-_{emn} \boldsymbol{R}_{2mn} e^{-j\Gamma^{(3)}_{mn}t} - A^-_{hmn} \boldsymbol{R}_{1mn} e^{-j\Gamma^{(3)}_{mn}t} \right]$$

$$= \sum_p \left[-F_p \sin(k_z t) + G_p \cos(k_z t) \right] \boldsymbol{E}_{tp}, \qquad \boldsymbol{r} \in \Omega \qquad (2.45)$$

when $z = -t$. F_p and G_p are used here to represent the waveguide coefficients for both TM and TE modes, given the similarity between (2.29) and (2.36). It is assumed that the transverse electric field outside of the aperture but within the unit cell will go to zero at $z = -t$ due to the presence of a perfect electrical conductor in that space. The quantity $\boldsymbol{E}^i_t$ represents the transverse electric field in the plane $z = 0$ due to the incident plane wave, and it is defined as

$$\boldsymbol{E}^i_t = E^i_0(\hat{x}e_x + \hat{y}e_y)e^{-jk_0\left(x\cos\phi_i\sin\theta_i + y\sin\phi_i\sin\theta_i\right)}, \qquad (2.46)$$

where e_x and e_y are used to describe the transverse field components and E^i_0 is the incident electric field amplitude. Using (2.16), (2.32), and (2.39), the continuity of transverse magnetic field within the aperture region leads to

$$\hat{z} \times \boldsymbol{H}^i_t + \sum_{m,n} \left[A^+_{emn} Y^{(1)}_e \boldsymbol{R}_{2mn} + A^+_{hmn} Y^{(1)}_h \boldsymbol{R}_{1mn} \right] = \sum_p \left[\frac{-\nu_p}{\eta_2} F_p \boldsymbol{E}_{tp} \right], \qquad \boldsymbol{r} \in \Omega$$

$$(2.47)$$

when $z = 0$ and

$$\sum_{m,n} \left[A^-_{emn} Y^{(3)}_e \boldsymbol{R}_{2mn} e^{-j\Gamma^{(3)}_{mn}t} - A^-_{hmn} Y^{(3)}_h \boldsymbol{R}_{1mn} e^{-j\Gamma^{(3)}_{mn}t} \right]$$

$$= \sum_p \left[\frac{-\nu_p}{\eta_2} F_p \cos(k_z t) + G_p \sin(k_z t) \right] \boldsymbol{E}_{tp}, \qquad \boldsymbol{r} \in \Omega \qquad (2.48)$$

when $z = -t$. The quantity $\hat{z} \times \boldsymbol{H}_t^i$ represents the transverse part of the incident magnetic field in the plane $z = 0$, and it is defined as

$$\hat{z} \times \boldsymbol{H}_t^i = (\hat{y} h_x - \hat{x} h_y) \frac{E_0^i}{\eta_1} e^{-jk_0(x \cos\phi_i \sin\theta_i + y \sin\phi_i \sin\theta_i)}, \qquad (2.49)$$

where h_x and h_y describe the transverse field components and η_1 is the intrinsic impedance in region I. Also, ν_p is defined such that

$$\nu_p = j \frac{k_2}{k_z}$$

for TM modes and

$$\nu_p = j \frac{k_z}{k_2}$$

for TE modes.

2.4 System of Linear Equations

The Floquet waves are orthogonal such that

$$\int_S \boldsymbol{R}_{lmn} \cdot \boldsymbol{R}_{l'm'n'}^* \mathrm{d}s = \delta_{ll'} \delta_{mm'} \delta_{nn'},$$

and δ is the Kronecker delta function [26]. Having enforced the boundary conditions, the orthogonality of the Floquet waves can be used on (2.44) and (2.45) to solve for the Floquet wave coefficients. Multiplying (2.44) by $\boldsymbol{R}_{1m'n'}^*$ and integrating over S gives

$$A_{hmn}^+ = \int_S \boldsymbol{E}_t^i \cdot \boldsymbol{R}_{1mn}^* \mathrm{d}s - \sum_p G_p \int_\Omega \boldsymbol{E}_{tp} \cdot \boldsymbol{R}_{1mn}^* \mathrm{d}s. \qquad (2.50)$$

Multiplying (2.44) by $\boldsymbol{R}_{2m'n'}^*$ and integrating over S gives

$$A_{emn}^+ = \int_S \boldsymbol{E}_t^i \cdot \boldsymbol{R}_{2mn}^* \mathrm{d}s - \sum_p G_p \int_\Omega \boldsymbol{E}_{tp} \cdot \boldsymbol{R}_{2mn}^* \mathrm{d}s. \qquad (2.51)$$

Multiplying (2.45) by $\boldsymbol{R}^*_{1m'n'}$ and integrating over S gives

$$A^-_{hmn} = e^{j\Gamma^{(3)}_{mn}t} \sum_p [F_p \sin(k_z t) - G_p \cos(k_z t)] \int_\Omega \boldsymbol{E}_{tp} \cdot \boldsymbol{R}^*_{1mn} \mathrm{d}s. \qquad (2.52)$$

Multiplying (2.45) by $\boldsymbol{R}^*_{2m'n'}$ and integrating over S gives

$$A^-_{emn} = e^{j\Gamma^{(3)}_{mn}t} \sum_p [-F_p \sin(k_z t) + G_p \cos(k_z t)] \int_\Omega \boldsymbol{E}_{tp} \cdot \boldsymbol{R}^*_{2mn} \mathrm{d}s. \qquad (2.53)$$

The modal waveguide fields are orthogonal [28][29] such that

$$\int_\Omega \boldsymbol{E}_{tp} \cdot \boldsymbol{E}_{tp'} \mathrm{d}s = \delta_{pp'}.$$

In fact, they are orthonormal due to the normalization that is applied by (2.30) and (2.37). The waveguide field orthogonality can be used with (2.47) and (2.48) to obtain additional expressions involving the Floquet wave coefficients and waveguide coefficients. Multiplying (2.47) by $\boldsymbol{E}_{tp'}$ and integrating over Ω gives

$$-\sum_{m,n} \int_\Omega \boldsymbol{E}_{tp} \cdot \left[A^+_{emn} Y^{(1)}_e \boldsymbol{R}_{2mn} + A^+_{hmn} Y^{(1)}_h \boldsymbol{R}_{1mn} \right] \mathrm{d}s = \frac{\nu_p}{\eta_2} F_p + \int_\Omega [\hat{z} \times \boldsymbol{H}^i_t] \cdot \boldsymbol{E}_{tp} \mathrm{d}s. \qquad (2.54)$$

Multiplying (2.48) by $\boldsymbol{E}_{tp'}$ and integrating over Ω gives

$$\sum_{m,n} \int_\Omega e^{-j\Gamma^{(3)}_{mn}t} \boldsymbol{E}_{tp} \cdot \left[A^-_{hmn} Y^{(3)}_h \boldsymbol{R}_{1mn} - A^-_{emn} Y^{(3)}_e \boldsymbol{R}_{2mn} \right] \mathrm{d}s$$
$$= \frac{\nu_p}{\eta_2} [F_p \cos(k_z t) + G_p \sin(k_z t)]. \qquad (2.55)$$

Making some substitutions, (2.50)-(2.55) can be rewritten as

$$A^+_{hmn} = S_{1mn} - \sum_p G_p P_{1pmn}, \qquad (2.56)$$

22

$$A_{emn}^{+} = S_{2mn} - \sum_{p} G_p P_{2pmn}, \tag{2.57}$$

$$A_{hmn}^{-} = e^{j\Gamma_{mn}^{(3)}t} \sum_{p} [F_p \sin(k_z t) - G_p \cos(k_z t)] P_{1pmn}, \tag{2.58}$$

$$A_{emn}^{-} = e^{j\Gamma_{mn}^{(3)}t} \sum_{p} [-F_p \sin(k_z t) + G_p \cos(k_z t)] P_{2pmn}, \tag{2.59}$$

$$\frac{\nu_p}{\eta_2} F_p = - \sum_{m,n} [A_{emn}^{+} Y_e^{(1)} Q_{2pmn} + A_{hmn}^{+} Y_h^{(1)} Q_{1pmn}] - S_p, \tag{2.60}$$

$$\sum_{m,n} e^{-j\Gamma_{mn}^{(3)}t} [A_{hmn}^{-} Y_h^{(3)} Q_{1pmn} - A_{emn}^{-} Y_e^{(3)} Q_{2pmn}] = \frac{\nu_p}{\eta_2} [F_p \cos(k_z t) + G_p \sin(k_z t)], \tag{2.61}$$

where

$$S_{1mn} = \int_{S} \boldsymbol{E}_t^i \cdot \boldsymbol{R}_{1mn}^* ds, \tag{2.62}$$

$$S_{2mn} = \int_{S} \boldsymbol{E}_t^i \cdot \boldsymbol{R}_{2mn}^* ds, \tag{2.63}$$

$$S_p = \int_{\Omega} (\hat{z} \times \boldsymbol{H}_t^i) \cdot \boldsymbol{E}_{tp} ds, \tag{2.64}$$

$$P_{1pmn} = \int_{\Omega} \boldsymbol{E}_{tp} \cdot \boldsymbol{R}_{1mn}^* ds, \tag{2.65}$$

$$P_{2pmn} = \int_{\Omega} \boldsymbol{E}_{tp} \cdot \boldsymbol{R}_{2mn}^* ds, \tag{2.66}$$

$$Q_{1pmn} = \int_{\Omega} \boldsymbol{E}_{tp} \cdot \boldsymbol{R}_{1mn} ds, \tag{2.67}$$

$$Q_{2pmn} = \int_{\Omega} \boldsymbol{E}_{tp} \cdot \boldsymbol{R}_{2mn} ds. \tag{2.68}$$

Eliminating the Floquet coefficients by substituting (2.56) and (2.57) into (2.60), and (2.58) and (2.59) into (2.61), and making some additional substitutions, leads to

$$F_p - \sum_{i} G_i \bar{K}_{pi} = \bar{J}_p, \tag{2.69}$$

$$F_p W_p^c + G_p W_p^s - \sum_i [F_i T_{pi} - G_i U_{pi}] = 0, \tag{2.70}$$

where

$$J_p = -S_p - \sum_{m,n} [Y_e^{(1)} S_{2mn} Q_{2pmn} - Y_h^{(1)} S_{1mn} Q_{1pmn}],$$

$$K_{pi} = \sum_{m,n} [Y_h^{(1)} P_{1imn} Q_{1pmn} + Y_e^{(1)} P_{2imn} Q_{2pmn}],$$

$$T_{pi} = \sin(k_z t) \sum_{m,n} [Y_e^{(3)} P_{2imn} Q_{2pmn} + Y_e^{(1)} P_{1imn} Q_{1pmn}],$$

$$U_{pi} = \cos(k_z t) \sum_{m,n} [Y_e^{(3)} P_{2imn} Q_{2pmn} + Y_e^{(1)} P_{1imn} Q_{1pmn}],$$

$$\bar{J}_p = \frac{\eta_2}{\nu_p} J_p,$$

$$\bar{K}_{pi} = \frac{\eta_2}{\nu_p} K_{pi},$$

$$W_p^c = \frac{\nu_p}{\eta_2} \cos(k_{zp} t),$$

$$W_p^s = \frac{\nu_p}{\eta_2} \sin(k_z t).$$

Expressions (2.69) and (2.70) can be used to construct a square matrix equation of the form $Ax = b$, where the unknowns are the waveguide coefficients. Once the waveguide coefficients are known, (2.56)-(2.59) can be used to compute the Floquet coefficients.

2.5 Shielding Effectiveness

Shielding effectiveness is defined as the ratio of power carried by the Floquet waves in region III to the power carried by the incident plane wave in region I. Computing the power carried by the Floquet waves requires determining the power transmitted through the unit cell. This is computed by integrating the time-average Poynting vector,

$$P = \int_S \frac{1}{2} \Re \left(\boldsymbol{E} \times \boldsymbol{H}^* \right) \cdot \hat{z} \mathrm{d}s. \tag{2.71}$$

Using vector identities and passing the dot product inside of the $\Re$ expression, (2.71) can be rewritten in terms of the transverse components of the electric and magnetic fields, leading to

$$P = -\int_S \frac{1}{2}\Re\left(\boldsymbol{E}_t \cdot (\hat{z} \times \boldsymbol{H}_t^*)\right)\,\mathrm{d}s. \tag{2.72}$$

Recalling (2.15) and the complex conjugate of (2.16) for the fields in region III gives

$$\boldsymbol{E}_t = \sum_{m,n=-\infty}^{\infty}\left[A_{emn}^-\boldsymbol{R}_{2mn}^- - A_{hmn}^-\boldsymbol{R}_{1mn}^-\right],$$

$$\hat{z} \times \boldsymbol{H}_t^* = \sum_{p,q=-\infty}^{\infty}\left[-A_{hpq}^{-*}Y_h^{(3)*}\boldsymbol{R}_{1pq}^{-*} + A_{epq}^{-*}Y_e^{(3)*}\boldsymbol{R}_{2pq}^{-*}\right].$$

Writing out the dot product in (2.72) gives

$$\boldsymbol{E}_t \cdot (\hat{z} \times \boldsymbol{H}_t^*) = \sum_{m,n,p,q=-\infty}^{\infty}\left[A_{emn}^-A_{epq}^{-*}\boldsymbol{R}_{2mn}^- \cdot \boldsymbol{R}_{2pq}^{-*}Y_e^{(3)*} + A_{hmn}^-A_{hpq}^{-*}\boldsymbol{R}_{1mn}^- \cdot \boldsymbol{R}_{1pq}^{-*}Y_h^{(3)*}\right.$$
$$\left. -A_{emn}^-A_{hpq}^{-*}\boldsymbol{R}_{2mn}^- \cdot \boldsymbol{R}_{1pq}^{-*}Y_h^{(3)*} - A_{hmn}^-A_{epq}^{-*}\boldsymbol{R}_{1mn}^- \cdot \boldsymbol{R}_{2pq}^{-*}Y_e^{(3)*}\right]. \tag{2.73}$$

Substituting (2.73) into (2.72) leads to four integral expressions. The integrals can be evaluated using the orthogonality properties of the Floquet waves, giving

$$\int_S \boldsymbol{R}_{2mn}^- \cdot \boldsymbol{R}_{2pq}^{-*}\mathrm{d}s = e^{j\Gamma_{mn}^{(3)}z}e^{-j\Gamma_{mn}^{(3)*}z}\int_S \boldsymbol{R}_{2mn} \cdot \boldsymbol{R}_{2pq}^*\mathrm{d}s = e^{j\Gamma_{mn}^{(3)}z}e^{-j\Gamma_{mn}^{(3)*}z}\delta_{mp}\delta_{nq},$$

$$\int_S \boldsymbol{R}_{1mn}^- \cdot \boldsymbol{R}_{1pq}^{-*}\mathrm{d}s = e^{j\Gamma_{mn}^{(3)}z}e^{-j\Gamma_{mn}^{(3)*}z}\int_S \boldsymbol{R}_{1mn} \cdot \boldsymbol{R}_{1pq}^*\mathrm{d}s = e^{j\Gamma_{mn}^{(3)}z}e^{-j\Gamma_{mn}^{(3)*}z}\delta_{mp}\delta_{nq},$$

$$\int_S \boldsymbol{R}_{2mn}^- \cdot \boldsymbol{R}_{1pq}^{-*}\mathrm{d}s = e^{j\Gamma_{mn}^{(3)}z}e^{-j\Gamma_{mn}^{(3)*}z}\int_S \boldsymbol{R}_{2mn} \cdot \boldsymbol{R}_{1pq}^*\mathrm{d}s = 0,$$

$$\int_S \boldsymbol{R}_{2mn}^- \cdot \boldsymbol{R}_{2pq}^{-*}\mathrm{d}s = e^{j\Gamma_{mn}^{(3)}z}e^{-j\Gamma_{mn}^{(3)*}z}\int_S \boldsymbol{R}_{1mn} \cdot \boldsymbol{R}_{2pq}^*\mathrm{d}s = 0.$$

Equation (2.72) can now be rewritten to reflect transmitted power such that

$$P_{trans} = -\frac{1}{2}\Re\left[\sum_{m,n=-\infty}^{\infty}\left(|A_{emn}^-|^2 Y_e^{(3)*} + |A_{hmn}^-|^2 Y_h^{(3)*}\right)e^{j\Gamma_{mn}^{(3)}z}e^{-j\Gamma_{mn}^{(3)*}z}\right]. \qquad (2.74)$$

For propagating Floquet modes,

$$\Gamma_{mn}^{(3)\,2} = k_3^2 - \alpha_m^2 - \beta_{mn}^2 > 0, \qquad \Gamma_{mn}^{(3)} \text{ is real and positive,}$$

while for evanescent Floquet modes,

$$\Gamma_{mn}^{(3)\,2} = k_3^2 - \alpha_m^2 - \beta_{mn}^2 < 0, \qquad \Gamma_{mn}^{(3)} \text{ is imaginary and negative.}$$

The Floquet wave admitttances $Y_e^{(3)}$ and $Y_h^{(3)}$ are defined as

$$Y_e^{(3)} = \frac{\omega\epsilon_3}{\Gamma_{mn}^{(3)}},$$
$$Y_h^{(3)} = \frac{\Gamma_{mn}^{(3)}}{\omega\mu_3},$$

and ω, ϵ_3, and μ_3 are always real and positive. Therefore, for evanescent modes, $Y_e^{(3)}$ and $Y_h^{(3)}$ are imaginary, so these modes provide no contribution to the series, and (2.74) can be rewritten as

$$P_{trans} = -\frac{1}{2}\left[\sum_{m,n}\left(|A_{emn}^-|^2 Y_e^{(3)} + |A_{hmn}^-|^2 Y_h^{(3)}\right)\right], \qquad (2.75)$$

where m and n correspond to the indices of propagating modes. The power carried by the incident plane wave is determined by substituting (2.46) and (2.49) into (2.72), leading to

$$P_{inc} = -\int_S \frac{1}{2}\Re\left[\boldsymbol{E}_t^i \cdot \left(\hat{z} \times \boldsymbol{H}_t^{i*}\right)\right]ds = -\frac{1}{2}\int_S\left[(e_y h_x - e_x h_y)\frac{E_0^{i\,2}}{\eta_1}\right]ds$$

$$= \frac{-A_s \cos \theta_i}{2\eta_1} E_0^{i\,2}.\tag{2.76}$$

Shielding effectiveness (SE) is computed based on the ratio of transmitted power to incident power so that

$$SE_{dB} = -10 \log_{10} \left(\frac{P_{trans}}{P_{inc}} \right).\tag{2.77}$$

The transmission coefficient (T) is the negative of the shielding effectiveness in dB such that

$$T_{dB} = -SE_{dB} = 10 \log_{10} \left(\frac{P_{trans}}{P_{inc}} \right).\tag{2.78}$$
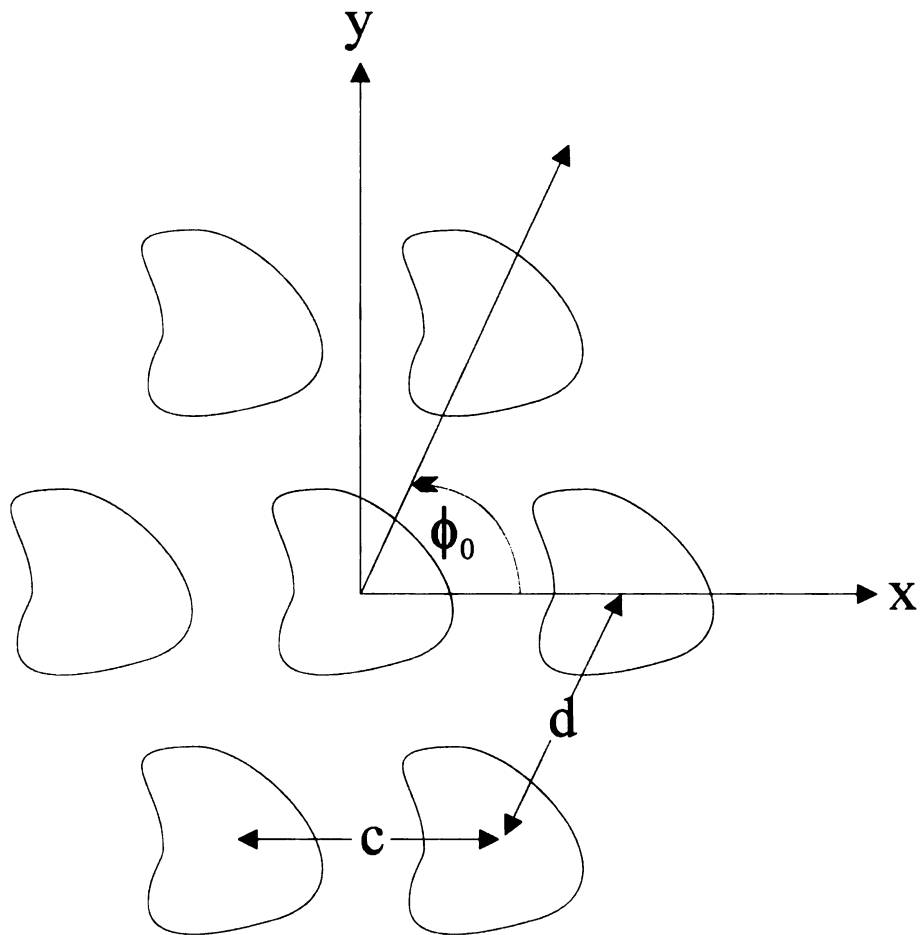
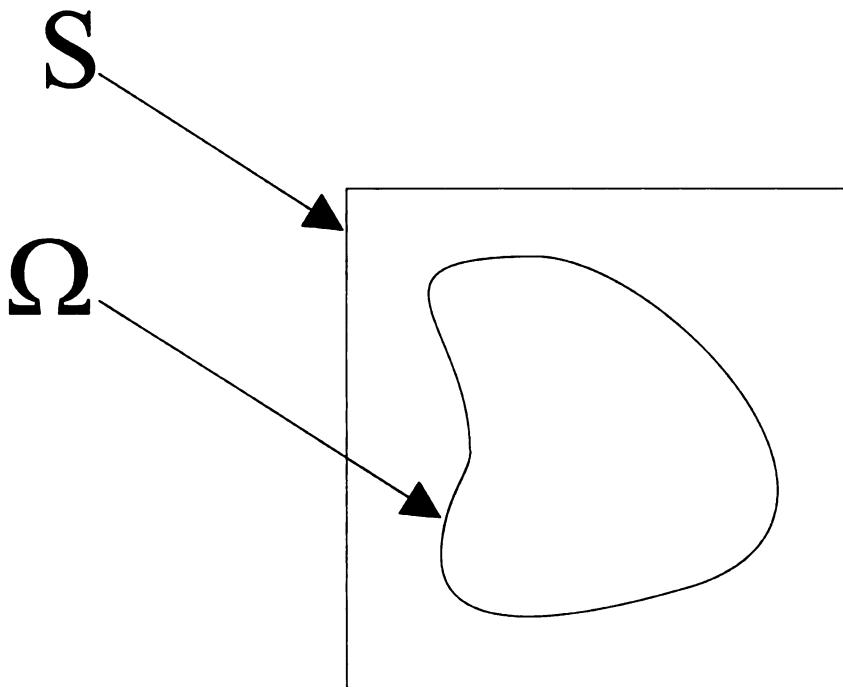Figure 2.1. Doubly-periodic conducting screen of apertures with general cross-sectional shape.

Figure 2.2. Unit cell for a doubly-periodic conducting screen of apertures with general cross-sectional shape.

CHAPTER 3

NUMERICAL RESULTS

3.1 Rectangular Apertures

The layout of the screen for the rectangular aperture case is shown in Figure 3.1, where the skew angle of the array, ϕ_0, the x-periodicity c and the skewed periodicity d are shown. Figure 3.2 shows the unit cell, where the aperture dimensions are a and b, and the unit cell dimensions are u and v.

3.1.1 Calculations

In order to compute the shielding effectiveness of a screen of rectangular apertures, a total of 14 integral calculations must be made. Four of them, (2.30), (2.37), (2.62), and (2.63), refer to TM or TE modes, or neither. By contrast, (2.64), (2.65), (2.66), (2.67), and (2.68) account for the other ten because each must be calculated for both TM and TE modes within the aperture. However, some similarities between the different formulas will lead to some redundancy in the calculations.

3.1.1.1 Computing S_{1mn} and S_{2mn}

Substituting (2.17) and (2.46) into (2.62) leads to

$$
\begin{aligned}
S_{1mn} &= \int_S \boldsymbol{E}_t^i \cdot \boldsymbol{R}_{1mn}^* \, \mathrm{d}s \\
&= \left(\frac{e_x \beta_{mn} - e_y \alpha_m}{\sqrt{\alpha_m^2 + \beta_{mn}^2}} \right) \frac{E_0^i}{\sqrt{A_s}} \\
&\quad \times \int_S e^{-jx(k_0 \cos \phi_i \sin \theta_i - \alpha_m)} e^{-jy(k_0 \sin \phi_i \sin \theta_i - \beta_{mn})} \mathrm{d}s \\
&= \left(\frac{e_x \beta_{mn} - e_y \alpha_m}{\sqrt{\alpha_m^2 + \beta_{mn}^2}} \right) \frac{4E_0^i}{\sqrt{uv}} F\left(\frac{u}{2}\right) G\left(\frac{v}{2}\right)
\end{aligned}
\tag{3.1}
$$

30

where

$$F(x) = \frac{\sin\left[x(k_0 \cos\phi_i \sin\theta_i - \alpha_m)\right]}{(k_0 \cos\phi_i \sin\theta_i - \alpha_m)},$$

$$G(y) = \frac{\sin\left[y(k_0 \sin\phi_i \sin\theta_i - \beta_{mn})\right]}{(k_0 \sin\phi_i \sin\theta_i - \beta_{mn})}.$$

Equation (3.1) is true for all combinations of the Floquet mode indices m and n except for three. If $m = n = 0$, (2.62) becomes

$$S_{1mn} = \left(\frac{e_x\beta_{mn} - e_y\alpha_m}{\sqrt{\alpha_m^2 + \beta_{mn}^2}}\right) E_0^i \sqrt{uv}. \tag{3.2}$$

If $m = 0$ only, (2.62) is expressed as

$$S_{1mn} = \left(\frac{e_x\beta_{mn} - e_y\alpha_m}{\sqrt{\alpha_m^2 + \beta_{mn}^2}}\right) \frac{2E_0^i u}{\sqrt{uv}} G\left(\frac{v}{2}\right). \tag{3.3}$$

And if $n = 0$ and $\phi_0 = 90°$, then (2.62) is found to be

$$S_{1mn} = \left(\frac{e_x\beta_{mn} - e_y\alpha_m}{\sqrt{\alpha_m^2 + \beta_{mn}^2}}\right) \frac{2E_0^i v}{\sqrt{uv}} F\left(\frac{u}{2}\right). \tag{3.4}$$

Using similar reasoning, substituting (2.18) and (2.46) into (2.63) leads to

$$\begin{aligned}
S_{2mn} &= \int_S \boldsymbol{E}_t^i \cdot \boldsymbol{R}_{2mn}^* \mathrm{d}s \\
&= \left(\frac{e_x\alpha_m + e_y\beta_{mn}}{\sqrt{\alpha_m^2 + \beta_{mn}^2}}\right) \frac{E_0^i}{\sqrt{A_s}} \\
&\quad \times \int_S e^{-jx(k_0 \cos\phi_i \sin\theta_i - \alpha_m)} e^{-jy(k_0 \sin\phi_i \sin\theta_i - \beta_{mn})} \mathrm{d}s \\
&= \left(\frac{e_x\alpha_m + e_y\beta_{mn}}{\sqrt{\alpha_m^2 + \beta_{mn}^2}}\right) \frac{4E_0^i}{\sqrt{uv}} F\left(\frac{u}{2}\right) G\left(\frac{v}{2}\right)
\end{aligned} \tag{3.5}$$

31

Equation (3.5) is also true for all combinations of the Floquet mode indices m and n except for three. If $m = n = 0$, (2.63) becomes

$$S_{2mn} = \left(\frac{e_x \alpha_m + e_y \beta_{mn}}{\sqrt{\alpha_m^2 + \beta_{mn}^2}} \right) E_0^i \sqrt{uv}. \tag{3.6}$$

If $m = 0$ only, (2.63) is expressed as

$$S_{2mn} = \left(\frac{e_x \alpha_m + e_y \beta_{mn}}{\sqrt{\alpha_m^2 + \beta_{mn}^2}} \right) \frac{2E_0^i u}{\sqrt{uv}} G\left(\frac{v}{2}\right). \tag{3.7}$$

And if $n = 0$ and $\phi_0 = 90°$, then (2.63) is found to be

$$S_{2mn} = \left(\frac{e_x \alpha_m + e_y \beta_{mn}}{\sqrt{\alpha_m^2 + \beta_{mn}^2}} \right) \frac{2E_0^i v}{\sqrt{uv}} F\left(\frac{u}{2}\right). \tag{3.8}$$

3.1.1.2 Computing f_{pe} and f_{ph}

To evaluate f_{pe}, the normalization integral for TM modes in the aperture, (2.40) is substituted into (2.28), leading to

$$e_{tp} = jk_z \left(\hat{x} k_x \cos\left[k_x\left(x + \frac{a}{2}\right)\right] \sin\left[k_y\left(y + \frac{b}{2}\right)\right] \right.$$
$$\left. + \hat{y} k_y \sin\left[k_x\left(x + \frac{a}{2}\right)\right] \cos\left[k_y\left(y + \frac{b}{2}\right)\right] \right),$$

which is then substituted into (2.30) such that

$$\begin{aligned}
f_{pe} &= \int_\Omega e_{tp} \cdot e_{tp}\, ds \\
&= -k_z^2 \int_\Omega k_x^2 \cos^2\left[k_x\left(x + \frac{a}{2}\right)\right] \sin^2\left[k_y\left(y + \frac{b}{2}\right)\right] ds \\
&\quad - k_z^2 \int_\Omega k_y^2 \sin^2\left[k_x\left(x + \frac{a}{2}\right)\right] \cos^2\left[k_y\left(y + \frac{b}{2}\right)\right] ds \\
&= -k_z^2 \left(k_x^2 + k_y^2\right) \frac{ab}{4}.
\end{aligned} \tag{3.9}$$

This result is found by using basic substitution to evaluate the integrals and discarding any terms that involve the sine of an integer multiple of π, which is always zero.

To evaluate f_{ph}, the normalization integral for TE modes in the aperture, (2.41) is substituted into (2.35), leading to

$$Z_{hp}\left(\hat{z}\times\boldsymbol{h}_{tp}\right)=jk_{z}Z_{hp}\left(\hat{x}k_{y}\cos\left[k_{x}\left(x+\frac{a}{2}\right)\right]\sin\left[k_{y}\left(y+\frac{b}{2}\right)\right]\right.$$
$$\left.-\hat{y}k_{x}\sin\left[k_{x}\left(x+\frac{a}{2}\right)\right]\cos\left[k_{y}\left(y+\frac{b}{2}\right)\right]\right),$$

which is then substituted into (2.37) such that

$$\begin{aligned}
f_{ph} &= \int_{\Omega}Z_{hp}(\hat{z}\times\boldsymbol{h}_{tp})\cdot Z_{hp}(\hat{z}\times\boldsymbol{h}_{tp})\mathrm{d}s \\
&= -\omega^{2}\mu^{2}\int_{\Omega}k_{y}^{2}\cos^{2}\left[k_{x}\left(x+\frac{a}{2}\right)\right]\sin^{2}\left[k_{y}\left(y+\frac{b}{2}\right)\right]\mathrm{d}s \\
&\quad -\omega^{2}\mu^{2}\int_{\Omega}k_{x}^{2}\sin^{2}\left[k_{x}\left(x+\frac{a}{2}\right)\right]\cos^{2}\left[k_{y}\left(y+\frac{b}{2}\right)\right]\mathrm{d}s \\
&= -\omega^{2}\mu^{2}\left(k_{x}^{2}+k_{y}^{2}\right)\frac{ab}{4}.
\end{aligned} \tag{3.10}$$

This result is also found by using basic substitution to evaluate the integrals and discarding any terms that involve the sine of an integer multiple of π, which is always zero. Equation (3.10) is valid for all TE modes in the aperture except for those involving either $k_{x}=0$ or $k_{y}=0$. If $k_{x}=0$, f_{ph} becomes

$$\begin{aligned}
f_{ph} &= \int_{\Omega}Z_{hp}(\hat{z}\times\boldsymbol{h}_{tp})\cdot Z_{hp}(\hat{z}\times\boldsymbol{h}_{tp})\mathrm{d}s \\
&= -\omega^{2}\mu^{2}\int_{\Omega}k_{y}^{2}\sin^{2}\left[k_{y}\left(y+\frac{b}{2}\right)\right]\mathrm{d}s \\
&= -\omega^{2}\mu^{2}k_{y}^{2}\frac{ab}{2}.
\end{aligned} \tag{3.11}$$

If $k_y = 0$, f_{ph} becomes

$$
\begin{aligned}
f_{ph} &= \int_\Omega Z_{hp}(\hat{z} \times \boldsymbol{h}_{tp}) \cdot Z_{hp}(\hat{z} \times \boldsymbol{h}_{tp}) \mathrm{d}s \\
&= -\omega^2 \mu^2 \int_\Omega k_x^2 \sin^2\left[k_x\left(x + \frac{a}{2}\right)\right] \mathrm{d}s \\
&= -\omega^2 \mu^2 k_x^2 \frac{ab}{2}.
\end{aligned}
\tag{3.12}
$$

3.1.1.3 Computing S_p

Using (2.26), (2.28), (2.40), and (2.49) in (2.64) and making some substitutions gives

$$
\begin{aligned}
S_p^{TM} &= \int_\Omega (\hat{z} \times \boldsymbol{H}_t^i) \cdot \boldsymbol{E}_{tp} \mathrm{d}s \\
&= G_0 \int_\Omega e^{u_x x} e^{v_y y} \sin\left[k_x\left(x + \frac{a}{2}\right)\right] \cos\left[k_y\left(y + \frac{b}{2}\right)\right] \mathrm{d}s \\
&\quad - H_0 \int_\Omega e^{u_x x} e^{v_y y} \cos\left[k_x\left(x + \frac{a}{2}\right)\right] \sin\left[k_y\left(y + \frac{b}{2}\right)\right] \mathrm{d}s \\
&= G_0 G_1\left(\frac{a}{2}\right) G_2\left(\frac{b}{2}\right) - H_0 H_1\left(\frac{a}{2}\right) H_2\left(\frac{b}{2}\right)
\end{aligned}
\tag{3.13}
$$

for TM modes, where

$$
G_0 = \frac{jk_z E_0^i}{\eta_1 \sqrt{f_{pe}}} h_x k_y,
$$

$$
H_0 = \frac{jk_z E_0^i}{\eta_1 \sqrt{f_{pe}}} h_y k_x,
$$

$$
G_1(x) = \frac{-k_x e^{u_x x}[1 - 2\sin^2(k_x x)] + k_x e^{-u_x x}}{u_x^2 + k_x^2},
\tag{3.14}
$$

$$
G_2(y) = \frac{v_y e^{v_y y}[1 - 2\sin^2(k_y y)] - v_y e^{-v_y y}}{v_y^2 + k_y^2},
\tag{3.15}
$$

$$
H_1(x) = \frac{u_x e^{u_x x}[1 - 2\sin^2(k_x x)] - u_x e^{-u_x x}}{u_x^2 + k_x^2},
\tag{3.16}
$$

$$H_2(y) = \frac{-k_y e^{v_y y}[1 - 2\sin^2(k_y y)] + k_y e^{-v_y y}}{v_y^2 + k_y^2}, \tag{3.17}$$

$$u_x = -jk_0 \cos\phi_i \sin\theta_i, \tag{3.18}$$

$$v_y = -jk_0 \sin\phi_i \sin\theta_i. \tag{3.19}$$

There are a couple of special situations that should be noted for making these calculations. If either $u_x = 0$ or $k_x = 0$, the effect on (3.14) and (3.16) can be found directly from those expressions. However, if $u_x = k_x = 0$, (3.13) becomes

$$S_p^{TM} = -H_0 a H_2\left(\frac{b}{2}\right). \tag{3.20}$$

Similarly, if $v_y = k_y = 0$, (3.13) simplifies to

$$S_p^{TM} = G_0 G_1\left(\frac{a}{2}\right) b. \tag{3.21}$$

The effect of either $v_y = 0$ or $k_y = 0$ can be found by directly evaluating (3.15) and (3.17).

For TE modes, using (2.34), (2.35), (2.41), and (2.49) in (2.64) and making some substitutions gives

$$
\begin{aligned}
S_p^{TE} &= \int_\Omega (\hat{z} \times \boldsymbol{H}_t^i) \cdot \boldsymbol{E}_{tp} \mathrm{d}s \\
&= -G_0 \int_\Omega e^{u_x x} e^{v_y y} \sin\left[k_x\left(x + \frac{a}{2}\right)\right] \cos\left[k_{yn}\left(y + \frac{b}{2}\right)\right] \mathrm{d}s \\
&\quad - H_0 \int_\Omega e^{u_x x} e^{v_y y} \cos\left[k_x\left(x + \frac{a}{2}\right)\right] \sin\left[k_{yn}\left(y + \frac{b}{2}\right)\right] \mathrm{d}s \\
&= -G_0 G_1\left(\frac{a}{2}\right) G_2\left(\frac{b}{2}\right) - H_0 H_1\left(\frac{a}{2}\right) H_2\left(\frac{b}{2}\right),
\end{aligned}
\tag{3.22}
$$

where $G_1(x)$, $G_2(y)$, $H_1(x)$, $H_2(y)$, u_x, and v_y are defined by (3.14), (3.15), (3.16),

(3.17), (3.18), and (3.19) respectively, just as they were for the TM case. The change is in the definition of G_0 and H_0, where

$$G_0 = \frac{jk_z Z_{hp} E_0^i}{\eta_1 \sqrt{f_{ph}}} h_x k_x,$$

$$H_0 = \frac{jk_z Z_{hp} E_0^i}{\eta_1 \sqrt{f_{ph}}} h_y k_y,$$

for TE modes. Similar to the TM case, if $u_x = k_x = 0$, (3.22) becomes

$$S_p^{TE} = -H_0 a H_2 \left(\frac{b}{2}\right). \tag{3.23}$$

If $v_y = k_y = 0$, (3.22) simplifies to

$$S_p^{TE} = -G_0 G_1 \left(\frac{a}{2}\right) b. \tag{3.24}$$

3.1.1.4 Computing P_{1pmn}, P_{2pmn}, Q_{1pmn}, and Q_{2pmn}

In order to evaluate P_{1pmn}, P_{2pmn}, Q_{1pmn}, and Q_{2pmn}, the same computations that were carried out previously for S_p are repeated. In fact, the formulas to be shown will include the functions $G_1(x)$, $G_2(y)$, $H_1(x)$, and $H_2(y)$, which are defined by (3.14), (3.15), (3.16), and (3.17), respectively.

To calculate P_{1pmn} for TM modes, substituting (2.4), (2.5), (2.17), (2.26), (2.28), and (2.40) into (2.65) gives

$$
\begin{aligned}
P_{1pmn}^{TM} &= \int_{\Omega} \boldsymbol{E}_{tp} \cdot \boldsymbol{R}_{1mn}^* \mathrm{d}s \\
&= -G_0 \int_{\Omega} e^{u_x x} e^{v_y y} \sin\left[k_x\left(x + \frac{a}{2}\right)\right] \cos\left[k_y\left(y + \frac{b}{2}\right)\right] \mathrm{d}s \\
&\quad + H_0 \int_{\Omega} e^{u_x x} e^{v_y y} \cos\left[k_x\left(x + \frac{a}{2}\right)\right] \sin\left[k_y\left(y + \frac{b}{2}\right)\right] \mathrm{d}s
\end{aligned}
$$

36

$$= -G_0 G_1 \left(\frac{a}{2}\right) G_2 \left(\frac{b}{2}\right) - H_0 H_1 \left(\frac{a}{2}\right) H_2 \left(\frac{b}{2}\right), \tag{3.25}$$

where

$$G_0 = \frac{j k_z k_y \alpha_m}{\sqrt{A_s} \sqrt{f_{pe}} \sqrt{\alpha_m^2 + \beta_{mn}^2}},$$

$$H_0 = \frac{j k_z k_x \beta_{mn}}{\sqrt{A_s} \sqrt{f_{pe}} \sqrt{\alpha_m^2 + \beta_{mn}^2}},$$

$$u_x = j \alpha_m, \tag{3.26}$$

$$v_y = j \beta_{mn}. \tag{3.27}$$

If $u_x = k_{xm} = 0$, (3.25) becomes

$$P_{1pmn}^{TM} = H_0 a H_2 \left(\frac{b}{2}\right). \tag{3.28}$$

If $v_y = k_{yn} = 0$, (3.25) simplifies to

$$P_{1pmn}^{TM} = -G_0 G_1 \left(\frac{a}{2}\right) b. \tag{3.29}$$

For TE modes, P_{1pmn} is found by substituting (2.4), (2.5), (2.17), (2.34), (2.35), and (2.41) into (2.65), giving

$$
\begin{aligned}
P_{1pmn}^{TE} &= \int_\Omega \boldsymbol{E}_{tp} \cdot \boldsymbol{R}_{1mn}^* \mathrm{d}s \\
&= G_0 \int_\Omega e^{u_x x} e^{v_y y} \sin\left[k_x \left(x + \frac{a}{2}\right)\right] \cos\left[k_y \left(y + \frac{b}{2}\right)\right] \mathrm{d}s \\
&\quad + H_0 \int_\Omega e^{u_x x} e^{v_y y} \cos\left[k_x \left(x + \frac{a}{2}\right)\right] \sin\left[k_y \left(y + \frac{b}{2}\right)\right] \mathrm{d}s \\
&= G_0 G_1 \left(\frac{a}{2}\right) G_2 \left(\frac{b}{2}\right) + H_0 H_1 \left(\frac{a}{2}\right) H_2 \left(\frac{b}{2}\right), \tag{3.30}
\end{aligned}
$$

where

$$G_0 = \frac{jk_z k_x \alpha_m Z_{hp}}{\sqrt{A_s}\sqrt{f_{ph}}\sqrt{\alpha_m^2 + \beta_{mn}^2}},$$

$$H_0 = \frac{jk_z k_y \beta_{mn} Z_{hp}}{\sqrt{A_s}\sqrt{f_{ph}}\sqrt{\alpha_m^2 + \beta_{mn}^2}}.$$

If $u_x = k_x = 0$, (3.30) becomes

$$P_{1pmn}^{TE} = H_0 a H_2\left(\frac{b}{2}\right). \tag{3.31}$$

If $v_y = k_y = 0$, (3.30) simplifies to

$$P_{1pmn}^{TE} = G_0 G_1\left(\frac{a}{2}\right) b. \tag{3.32}$$

To calculate P_{2pmn} for TM modes, substituting (2.4), (2.5), (2.18), (2.26), (2.28), and (2.40) into (2.66) gives

$$
\begin{aligned}
P_{2pmn}^{TM} &= \int_\Omega \boldsymbol{E}_{tp} \cdot \boldsymbol{R}_{2mn}^* \mathrm{d}s \\
&= G_0 \int_\Omega e^{u_x x} e^{v_y y} \sin\left[k_x\left(x + \frac{a}{2}\right)\right] \cos\left[k_y\left(y + \frac{b}{2}\right)\right] \mathrm{d}s \\
&\quad + H_0 \int_\Omega e^{u_x x} e^{v_y y} \cos\left[k_x\left(x + \frac{a}{2}\right)\right] \sin\left[k_y\left(y + \frac{b}{2}\right)\right] \mathrm{d}s \\
&= G_0 G_1\left(\frac{a}{2}\right) G_2\left(\frac{b}{2}\right) + H_0 H_1\left(\frac{a}{2}\right) H_2\left(\frac{b}{2}\right),
\end{aligned}
\tag{3.33}
$$

where

$$G_0 = \frac{jk_z k_y \beta_{mn}}{\sqrt{A_s}\sqrt{f_{pe}}\sqrt{\alpha_m^2 + \beta_{mn}^2}},$$

$$H_0 = \frac{jk_z k_x \alpha_m}{\sqrt{A_s}\sqrt{f_{pe}}\sqrt{\alpha_m^2 + \beta_{mn}^2}},$$

and (3.39) and (3.40) still apply. If $u_x = k_x = 0$, (3.33) becomes

$$P_{2pmn}^{TM} = H_0 a H_2 \left(\frac{b}{2}\right). \tag{3.34}$$

If $v_y = k_y = 0$, (3.33) simplifies to

$$P_{2pmn}^{TM} = G_0 G_1 \left(\frac{a}{2}\right) b. \tag{3.35}$$

When calculating P_{2pmn} for TE modes, substituting (2.4), (2.5), (2.18), (2.27), (2.35), and (2.41) into (2.66) gives

$$
\begin{aligned}
P_{2pmn}^{TE} &= \int_\Omega \boldsymbol{E}_{tp} \cdot \boldsymbol{R}_{1mn}^* \mathrm{d}s \\
&= G_0 \int_\Omega e^{u_x x} e^{v_y y} \sin\left[k_x \left(x + \frac{a}{2}\right)\right] \cos\left[k_y \left(y + \frac{b}{2}\right)\right] \mathrm{d}s \\
&\quad + H_0 \int_\Omega e^{u_x x} e^{v_y y} \cos\left[k_x \left(x + \frac{a}{2}\right)\right] \sin\left[k_y \left(y + \frac{b}{2}\right)\right] \mathrm{d}s \\
&= G_0 G_1 \left(\frac{a}{2}\right) G_2 \left(\frac{b}{2}\right) + H_0 H_1 \left(\frac{a}{2}\right) H_2 \left(\frac{b}{2}\right),
\end{aligned} \tag{3.36}
$$

where

$$G_0 = \frac{j k_z k_x \alpha_m Z_{hp}}{\sqrt{A_s}\sqrt{f_{ph}}\sqrt{\alpha_m^2 + \beta_{mn}^2}},$$

$$H_0 = \frac{j k_z k_y \beta_{mn} Z_{hp}}{\sqrt{A_s}\sqrt{f_{ph}}\sqrt{\alpha_m^2 + \beta_{mn}^2}}.$$

If $u_x = k_x = 0$, (3.30) becomes

$$P_{2pmn}^{TE} = H_0 a H_2 \left(\frac{b}{2}\right). \tag{3.37}$$

If $v_y = k_y = 0$, (3.30) simplifies to

$$P_{2pmn}^{TE} = G_0 G_1 \left(\frac{a}{2}\right) b. \tag{3.38}$$

In order to compute Q_{1pmn} and Q_{2pmn} for TM and TE modes, the formulas are almost identical to what has been shown for P_{1pmn} and P_{2pmn}. The only difference is that (3.39) and (3.40) are defined such that

$$u_x = -j\alpha_m, \tag{3.39}$$

$$v_y = -j\beta_{mn}, \tag{3.40}$$

which are the complex conjugates of the versions used in computing P_{1pmn} and P_{2pmn}. Otherwise, the formulas and constants are exactly the same.

3.1.2 Discussion of Results

Figure 3.3 shows a plot of transmission coefficient versus frequency, where each curve represents a different value of screen thickness. The transmission coefficient is the negative of the shielding effectiveness in dB. The aperture is square shaped with dimensions a = b = 3.6 mm, while the unit cell is also square shaped with dimensions u = v = 3.6254 mm. The difference accounts for the thickness of the conducting region. These aperture dimensions were chosen because they are typical of the dimensions of aluminum honeycomb, samples of which were used for an experimental comparison to the numerical data. The excitation is a normally incident plane wave with magnetic field perpendicular to the $y - z$ plane, and the array of apertures is unskewed, i.e. $\phi_0 = 90°$. Because the array is unskewed, the periodicity and the unit cell dimensions along each direction are the same, i.e. $c = u$ and $d = v$. It is clear that increasing the thickness of the screen decreases the transmission of power through the screen at the lower frequencies. It is also important to note that once

the frequency reaches approximately 41 GHz, the shielding effectiveness approaches 0 dB irrespective of the screen thickness. This is expected given that the aperture size in this case is 3.6 mm, which corresponds to a cut-off frequency of 41.64 GHz for the dominant TE_{10} and TE_{01} modes of a square waveguide. For a normally incident plane wave with electric field perpendicular to the $x-z$ plane, the results are virtually identical. To compute the curves in Figure 3.3, 882 Floquet modes were used. 60 waveguide modes (mode indices ≤ 5) were used to compute the curves for the 1.1 mm, 2.2 mm, and 4.4 mm curves. For the larger thickness values, the curves for the shielding effectiveness did not provide meaningful data when using 60 waveguide modes. The trends that were observed in increasing from 1.1 mm to 2.2 mm to 4.4 mm were not apparent. However, using less waveguide modes did produce useful results that showed a continuing trend toward better shielding performance at lower frequencies when thickness was increased. The reasoning behind the use of less waveguide modes for higher thickness values is explained in Chapter 5, including the techniques that were used to evaluate problems with high thickness values. The number of waveguide modes used to compute the other curves in Figure 3.3 are shown in Table 3.1. All 60 waveguide modes and their corresponding cut-off frequencies are shown in Table 3.2.

Figure 3.4 shows the impact of changing the incidence angle θ_i for a TM-polarized, incident plane wave with a screen thickness of 5.5 mm. Results for 15° and 30° were computed, but are omitted due to their similarity to the 0° case. The dips in the higher frequency region are due to forced resonances that occur just prior to the onset of grating lobes. These points are known as Wood's anomalies [5][9], and they occur at the point in frequency where the separation between the apertures is about a wavelength. For the TE-polarized incident plane wave case, the curves in Figure 3.5 show more modest differences for the change in incidence angle. However, this case does indicate a downward shift in the resonant frequency as θ_i is increased, as was noted in [5]. Here, the resonant frequency is considered the point at which full

transmission is achieved. This is somewhat different from the TM-incidence case, where the increase in θ_i has no effect on the resonant frequency. Similar to the TM-incidence plot, results for 15° and 30° were omitted due to their similarity to the 0° case.

In getting numerical results for the rectangular aperture case, the choice for the number of Floquet modes was $(2 \times 10 + 1)^2 \times 2 = 882$, where each mode index (m and n) ranges from -10 to $+10$ and there are TM and TE sets of modes. This was the number of modes used in [19], and it represents the starting point for this study. Some consideration was given to the idea that using more Floquet modes, while more time-consuming for computations, might provide more accurate data. Figure 3.6 shows the comparison between using 882 Floquet modes and 1922 Floquet modes while holding the number of waveguide modes at 60. No appreciable difference was seen between the two cases when t=4.4 mm, and all curves were computed using 882 Floquet modes. A similar consideration was made with regard to the number of waveguide modes being used. Increasing the thickness beyond 6.6 mm prevents the use of 60 waveguide modes, but Figure 3.7 shows that just using the two dominant modes (TE_{10} and TE_{01}) of the square waveguide gives virtually the same curves as using 60 modes when t=4.4 mm. However, it should be noted that if the apertures were larger, higher-order modes would contribute at a lower point in frequency.

Figure 3.8 - Figure 3.14 show comparisons between mode-matching results and data using the waveguide below cut-off formula at different thicknesses. The waveguide below cut-off formula for transmission coefficient is given by

$$T_{dB} = 20 \log_{10} \left(e^{-\alpha d} \right) \tag{3.41}$$

where

$$\alpha = \omega \sqrt{\mu_2 \epsilon_2} \sqrt{\left(\frac{f_c}{f} \right)^2 - 1}. \tag{3.42}$$

42

The quantity d is the length of the aperture, and f_c is the cut-off frequency of the dominant rectangular waveguide mode, which in this case is given by $f_c = 41.64$ GHz. As the thickness of the screen is increased to five times the aperture width and larger, the agreement between the curves gets stronger. In fact, the waveguide below cutoff formula was developed to describe the attenuation of waves propagating in an opening whose length is at least five times its width [24]. The mode-matching approach is not limited to a certain ratio between aperture width and aperture length/screen thickness, making it more flexible for making shielding effectiveness calculations. In addition, the mode-matching approach can be used for frequencies above the cut-off frequency of the dominant waveguide mode.

Figure 3.15 and Figure 3.16 show mode-matching results using the proposed approach in comparison to past published results for mode-matching from [10]. Also, Figure 3.17, Figure 3.18, and Figure 3.19 compare results to published data from [19]. In each figure, both sets of data are very closely related. However, it should be noted that in [10] and [19], only the (m = 0, n = 0) Floquet mode was considered to be propagating. The curves are in very good agreement if that consideration is taken into account. However, if the frequencies of interest are high enough, other Floquet modes will become propagating and should therefore be included in the analysis [21][30]. In fact, the transmission nulls in Figure 3.15, Figure 3.16, and Figure 3.19 are due to the Wood's anomaly mentioned earlier. And in each case, the next propagating Floquet mode occurs very close in frequency to the location of the Wood's anomaly.

3.2 Circular Apertures

The layout of the screen for the circular aperture case is shown in Figure 3.20, where the skew angle of the array, ϕ_0, the x-periodicity c and the skewed periodicity d are shown. Figure 3.21 shows the unit cell, where the circular aperture radius is a, and the hexagonal unit cell dimension is u.

3.2.1 Calculations

In order to compute the shielding effectiveness of a screen of circular apertures, a total of 14 integral calculations must be made. Four of them, (2.30), (2.37), (2.62), and (2.63), refer to TM or TE modes, or neither. By contrast, (2.64), (2.65), (2.66), (2.67), and (2.68) account for the other ten because each must be calculated for both TM and TE modes within the aperture. In addition, due to the mode functions used for the circular aperture case, calculations must be done seperately for even and odd modes. However, some similarities between the different formulas will lead to some redundancy in the calculations.

3.2.1.1 Computing S_{1mn} and S_{2mn}

Substituting (2.17) and (2.46) into (2.62) leads to

$$
\begin{aligned}
S_{1mn} &= \int_S \boldsymbol{E}_t^i \cdot \boldsymbol{R}_{1mn}^* \mathrm{d}s \\
&= \left(\frac{e_x \beta_{mn} - e_y \alpha_m}{\sqrt{\alpha_m^2 + \beta_{mn}^2}} \right) \frac{E_0^i}{\sqrt{A_s}} \\
&\quad \times \int_S e^{-jx(k_0 \cos \phi_i \sin \theta_i - \alpha_m)} e^{-jy(k_0 \sin \phi_i \sin \theta_i - \beta_{mn})} \mathrm{d}s \\
&= \left(\frac{e_x \beta_{mn} - e_y \alpha_m}{\sqrt{\alpha_m^2 + \beta_{mn}^2}} \right) \frac{4E_0^i}{\sqrt{A_s}} \left[F_1(u) + F_2(u) \right]
\end{aligned}
\tag{3.43}
$$

where

$$
F_1(u) = \frac{e^{-j\rho_y \frac{2u}{\sqrt{3}}}}{\rho_y \left(\frac{\rho_y}{\sqrt{3}} + \rho_x \right)} \left(e^{j\left(\frac{\rho_y}{\sqrt{3}} + \rho_x \right)u} - 1 \right) - \frac{e^{j\rho_y \frac{2u}{\sqrt{3}}}}{\rho_y \left(\frac{\rho_y}{\sqrt{3}} - \rho_x \right)} \left(1 - e^{-j\left(\frac{\rho_y}{\sqrt{3}} - \rho_x \right)u} \right),
\tag{3.44}
$$

$$
F_2(u) = \frac{e^{-j\rho_y \frac{2u}{\sqrt{3}}}}{\rho_y \left(\frac{\rho_y}{\sqrt{3}} - \rho_x \right)} \left(e^{j\left(\frac{\rho_y}{\sqrt{3}} - \rho_x \right)u} - 1 \right) - \frac{e^{j\rho_y \frac{2u}{\sqrt{3}}}}{\rho_y \left(\frac{\rho_y}{\sqrt{3}} + \rho_x \right)} \left(1 - e^{-j\left(\frac{\rho_y}{\sqrt{3}} + \rho_x \right)u} \right),
\tag{3.45}
$$

$$
\rho_x = k_0 \cos \phi_i \sin \theta_i - \alpha_m,
$$

44

$$\rho_y = k_0 \sin \phi_i \sin \theta_i - \beta_{mn}.$$

This result is obtained by forming linear equations for the unit cell boundaries and integrating over the limits. The equations are

$$y_1(x) = \frac{-1}{\sqrt{3}}x - \frac{2u}{\sqrt{3}},$$

$$y_2(x) = \frac{1}{\sqrt{3}}x + \frac{2u}{\sqrt{3}},$$

$$y_3(x) = \frac{1}{\sqrt{3}}x - \frac{2u}{\sqrt{3}},$$

$$y_4(x) = \frac{-1}{\sqrt{3}}x + \frac{2u}{\sqrt{3}},$$

and $F_1(x)$ and $F_2(x)$ are expressed as

$$F_1(x) = \int_{-u}^{0} e^{-j\rho_x x} \left[\int_{y_1(x)}^{y_2(x)} e^{-j\rho_y y} dy \right] dx,$$

$$F_2(x) = \int_{0}^{u} e^{-j\rho_x x} \left[\int_{y_3(x)}^{y_4(x)} e^{-j\rho_y y} dy \right] dx.$$

Equation (3.43) is true for almost all combinations of the Floquet mode indices. If $m = n = 0$, (3.43) becomes

$$S_{1mn} = \left(\frac{e_x \beta_{mn} - e_y \alpha_m}{\sqrt{\alpha_m^2 + \beta_{mn}^2}} \right) E_0^i \sqrt{A_s}. \tag{3.46}$$

If the mode indices are such that $\rho_y = \rho_x \sqrt{3}$, (3.43) still applies with (3.44) and (3.45) simplifying to

$$F_1(u) = \frac{e^{-j\rho_y \frac{2u}{\sqrt{3}}}}{\rho_y \left(\frac{\rho_y}{\sqrt{3}} + \rho_x \right)} \left(e^{j(\frac{\rho_y}{\sqrt{3}} + \rho_x)u} - 1 \right) - j \frac{e^{j\rho_y \frac{2u}{\sqrt{3}}}}{\rho_y} u, \tag{3.47}$$

$$F_2(u) = \frac{e^{-j\rho_y \frac{2u}{\sqrt{3}}}}{\rho_y \left(\frac{\rho_y}{\sqrt{3}} + \rho_x\right)} \left(e^{-j\left(\frac{\rho_y}{\sqrt{3}} + \rho_x\right)u} - 1\right) + j\frac{e^{-j\rho_y \frac{2u}{\sqrt{3}}}}{\rho_y}u. \tag{3.48}$$

Using similar reasoning, substituting (2.18) and (2.46) into (2.63) leads to

$$
\begin{aligned}
S_{2mn} &= \int_S \boldsymbol{E}_t^i \cdot \boldsymbol{R}_{2mn}^* ds \\
&= \left(\frac{e_x\alpha_m + e_y\beta_{mn}}{\sqrt{\alpha_m^2 + \beta_{mn}^2}}\right) \frac{E_0^i}{\sqrt{A_s}} \\
&\quad \times \int_S e^{-jx(k_0\cos\phi_i\sin\theta_i - \alpha_m)}e^{-jy(k_0\sin\phi_i\sin\theta_i - \beta_{mn})} ds \\
&= \left(\frac{e_x\alpha_m + e_y\beta_{mn}}{\sqrt{\alpha_m^2 + \beta_{mn}^2}}\right) \frac{4E_0^i}{\sqrt{A_s}} \left[F_1(u) + F_2(u)\right], \tag{3.49}
\end{aligned}
$$

with $F_1(u)$ and $F_2(u)$ given by (3.44) and (3.45), respectively, for most Floquet mode index combinations. If $m = n = 0$, (3.49) becomes

$$S_{2mn} = \left(\frac{e_x\alpha_m + e_y\beta_{mn}}{\sqrt{\alpha_m^2 + \beta_{mn}^2}}\right) E_0^i \sqrt{A_s}. \tag{3.50}$$

If the mode indices are such that $\rho_y = \rho_x\sqrt{3}$, (3.49) still applies with (3.47) and (3.48) defining $F_1(u)$ and $F_2(u)$, respectively.

3.2.1.2 Computing f_{pe} and f_{ph}

To evaluate f_{pe}, the normalization integral for TM modes in the aperture, (2.42) is substituted into (2.28), leading to

$$e_{tp} = jk_z \left(\hat{r}k_r J_c'(k_r r)\cos(c\phi) - \hat{\phi}\frac{c}{r}J_c(k_r r)\sin(c\phi)\right), \tag{3.51}$$

for even TM modes, and

$$e_{tp} = jk_z \left(\hat{r}k_r J_c'(k_r r)\sin(c\phi) + \hat{\phi}\frac{c}{r}J_c(k_r r)\cos(c\phi)\right), \tag{3.52}$$

for odd TM modes. Substituting either (3.51) or (3.52) into (2.30) gives

$$
\begin{aligned}
f_{pe} &= \int_\Omega \boldsymbol{e}_{tp} \cdot \boldsymbol{e}_{tp} \, ds \\
&= -k_z^2 k_r^2 \int_\Omega [J_c'(k_r r)]^2 [\cos(c\phi)]^2 ds - k_z^2 c^2 \int_\Omega \frac{1}{r^2} [J_c(k_r r)]^2 [\sin(c\phi)]^2 ds \\
&= -\pi k_z^2 k_r^2 \int_0^a r[J_c'(k_r r)]^2 dr - \pi k_z^2 c^2 \int_0^a \frac{1}{r} [J_c(k_r r)]^2 dr,
\end{aligned}
\tag{3.53}
$$

as long as $c \neq 0$. If $c = 0$,

$$
\begin{aligned}
f_{pe} &= \int_\Omega \boldsymbol{e}_{tp} \cdot \boldsymbol{e}_{tp} \, ds \\
&= -k_z^2 k_r^2 \int_\Omega [J_c'(k_r r)]^2 ds \\
&= -2\pi k_z^2 k_r^2 \int_0^a r[J_c'(k_r r)]^2 dr
\end{aligned}
\tag{3.54}
$$

for even TM modes, and $f_{pe} = 0$ for odd TM modes. The integrals in (3.53) and (3.54) can be computed in closed form, or they can be determined numerically.

To evaluate f_{ph}, the normalization integral for TE modes in the aperture, (2.43) is substituted into (2.35), leading to

$$
Z_{hp} \left(\hat{z} \times \boldsymbol{h}_{tp} \right) = j k_z Z_{hp} \left(\hat{\phi} k_r J_c'(k_r' r) \cos(c\phi) + \hat{r} \frac{c}{r} J_c(k_r' r) \sin(c\phi) \right),
\tag{3.55}
$$

for even TE mdoes, and

$$
Z_{hp} \left(\hat{z} \times \boldsymbol{h}_{tp} \right) = j k_z Z_{hp} \left(\hat{\phi} k_r J_c'(k_r' r) \sin(c\phi) - \hat{r} \frac{c}{r} J_c(k_r' r) \cos(c\phi) \right),
\tag{3.56}
$$

for odd TE modes. Substituting either (3.55) or (3.56) into (2.37) gives

$$
f_{ph} = \int_\Omega Z_{hp}(\hat{z} \times \boldsymbol{h}_{tp}) \cdot Z_{hp}(\hat{z} \times \boldsymbol{h}_{tp}) ds
$$

47

$$
= -(k_z k_r' Z_{hp})^2 \int_\Omega [J_c'(k_r' r)]^2 [\cos(c\phi)]^2 \mathrm{d}s - c^2 (k_z Z_{hp})^2 \int_\Omega \frac{1}{r^2} [J_c(k_r' r)]^2 [\sin(c\phi)]^2 \mathrm{d}s
$$

$$
= -\pi (k_z k_r' Z_{hp})^2 \int_0^a r[J_c'(k_r' r)]^2 \mathrm{d}r - \pi c^2 (k_z Z_{hp})^2 \int_0^a \frac{1}{r} [J_c(k_r' r)]^2 \mathrm{d}r \qquad (3.57)
$$

as long as $c \neq 0$. If $c = 0$,

$$
\begin{aligned}
f_{ph} &= \int_\Omega Z_{hp}(\hat{z} \times \boldsymbol{h}_{tp}) \cdot Z_{hp}(\hat{z} \times \boldsymbol{h}_{tp}) \mathrm{d}s \\
&= -(k_z k_r' Z_{hp})^2 \int_\Omega [J_c'(k_r' r)]^2 \mathrm{d}s \\
&= -\pi (k_z k_r' Z_{hp})^2 \int_0^a r[J_c'(k_r' r)]^2 \mathrm{d}r \qquad (3.58)
\end{aligned}
$$

for even TE modes, and $f_{ph} = 0$ for odd TE modes. The integrals in (3.57) and (3.58) can be computed in closed form, or they can be determined numerically.

3.2.1.3 Computing S_p

Using (2.26), (2.28), (2.42), and (2.49) in (2.64) and making some substitutions gives

$$
\begin{aligned}
S_p^{TM} &= \int_\Omega (\hat{z} \times \boldsymbol{H}_t^i) \cdot \boldsymbol{E}_{tp} \mathrm{d}s \\
&= +G_0 \int_0^a r J_c'(k_r r) \left[\int_0^{2\pi} \cos(c\phi)\sin(\phi) e^{-jk_0 r \sin\theta_i \cos(\phi - \phi_i)} \mathrm{d}\phi \right] \mathrm{d}r \\
&\quad -G_1 \int_0^a J_c(k_r r) \left[\int_0^{2\pi} \sin(c\phi)\cos(\phi) e^{-jk_0 r \sin\theta_i \cos(\phi - \phi_i)} \mathrm{d}\phi \right] \mathrm{d}r \\
&\quad -G_2 \int_0^a r J_c'(k_r r) \left[\int_0^{2\pi} \cos(c\phi)\cos(\phi) e^{-jk_0 r \sin\theta_i \cos(\phi - \phi_i)} \mathrm{d}\phi \right] \mathrm{d}r \\
&\quad -G_3 \int_0^a J_c(k_r r) \left[\int_0^{2\pi} \sin(c\phi)\sin(\phi) e^{-jk_0 r \sin\theta_i \cos(\phi - \phi_i)} \mathrm{d}\phi \right] \mathrm{d}r \\
&= +[G_0 G_4 - G_2 G_6] \int_0^a r J_c'(k_r r) J_{c+1}(k_0 r \sin\theta_i) \mathrm{d}r \\
&\quad -[G_0 G_5 + G_2 G_7] \int_0^a r J_c'(k_r r) J_{c-1}(k_0 r \sin\theta_i) \mathrm{d}r
\end{aligned}
$$

$$- [G_1 G_5 + G_3 G_7] \int\limits_0^a J_c(k_r r) J_{c+1}(k_0 r \sin \theta_i) \mathrm{d}r$$

$$- [G_1 G_4 - G_3 G_6] \int\limits_0^a J_c(k_r r) J_{c-1}(k_0 r \sin \theta_i) \mathrm{d}r \tag{3.59}$$

for even TM modes, and

$$
\begin{aligned}
S_p^{TM} &= \int\limits_\Omega (\hat{z} \times \boldsymbol{H}_t^i) \cdot \boldsymbol{E}_{tp} \mathrm{d}s \\
&= +G_0 \int\limits_0^a r J_c'(k_r r) \left[\int\limits_0^{2\pi} \sin(c\phi) \sin(\phi) e^{-jk_0 r \sin \theta_i \cos(\phi - \phi_i)} \mathrm{d}\phi \right] \mathrm{d}r \\
&\quad + G_1 \int\limits_0^a J_c(k_r r) \left[\int\limits_0^{2\pi} \cos(c\phi) \cos(\phi) e^{-jk_0 r \sin \theta_i \cos(\phi - \phi_i)} \mathrm{d}\phi \right] \mathrm{d}r \\
&\quad - G_2 \int\limits_0^a r J_c'(k_r r) \left[\int\limits_0^{2\pi} \sin(c\phi) \cos(\phi) e^{-jk_0 r \sin \theta_i \cos(\phi - \phi_i)} \mathrm{d}\phi \right] \mathrm{d}r \\
&\quad + G_3 \int\limits_0^a J_c(k_r r) \left[\int\limits_0^{2\pi} \cos(c\phi) \sin(\phi) e^{-jk_0 r \sin \theta_i \cos(\phi - \phi_i)} \mathrm{d}\phi \right] \mathrm{d}r \\
&= -[G_0 G_6 + G_2 G_4] \int\limits_0^a r J_c'(k_r r) J_{c+1}(k_0 r \sin \theta_i) \mathrm{d}r \\
&\quad + [G_0 G_7 - G_2 G_5] \int\limits_0^a r J_c'(k_r r) J_{c-1}(k_0 r \sin \theta_i) \mathrm{d}r \\
&\quad + [G_1 G_6 + G_3 G_4] \int\limits_0^a J_c(k_r r) J_{c+1}(k_0 r \sin \theta_i) \mathrm{d}r \\
&\quad + [G_1 G_7 - G_3 G_5] \int\limits_0^a J_c(k_r r) J_{c-1}(k_0 r \sin \theta_i) \mathrm{d}r \tag{3.60}
\end{aligned}
$$

for odd TM modes, where

$$G_0 = \frac{j k_z k_r E_0^i}{\eta_1 \sqrt{f_{pe}}} h_x,$$

$$G_1 = \frac{j k_z c E_0^i}{\eta_1 \sqrt{f_{pe}}} h_x,$$

$$G_2 = \frac{jk_z k_r E_0^i}{\eta_1 \sqrt{f_{pe}}} h_y,$$

$$G_3 = \frac{jk_z c E_0^i}{\eta_1 \sqrt{f_{pe}}} h_y,$$

$$G_4 = \pi j^{c+1} \sin[(c+1)\phi_i], \tag{3.61}$$

$$G_5 = \pi j^{c-1} \sin[(c-1)\phi_i], \tag{3.62}$$

$$G_6 = \pi j^{c+1} \cos[(c+1)\phi_i], \tag{3.63}$$

$$G_7 = \pi j^{c-1} \cos[(c-1)\phi_i]. \tag{3.64}$$

(3.59) and (3.60) are valid as long as $c \neq 0$. If $c = 0$,

$$
\begin{aligned}
S_p^{TM} &= \int_\Omega (\hat{z} \times \boldsymbol{H}_t^i) \cdot \boldsymbol{E}_{tp} \mathrm{d}s \\
&= +G_0 \int_0^a r J_0'(k_r r) \left[\int_0^{2\pi} \sin(\phi) e^{-jk_0 r \sin\theta_i \cos(\phi - \phi_i)} \mathrm{d}\phi \right] \mathrm{d}r \\
&\quad -G_2 \int_0^a r J_0'(k_r r) \left[\int_0^{2\pi} \cos(\phi) e^{-jk_0 r \sin\theta_i \cos(\phi - \phi_i)} \mathrm{d}\phi \right] \mathrm{d}r \\
&= j2\pi [G_0 \sin\phi_i - G_2 \cos\phi_i] \int_0^a r J_0'(k_r r) J_1(k_0 r \sin\theta_i) \mathrm{d}r
\end{aligned}
\tag{3.65}
$$

for even TM modes, and $S_p^{TM} = 0$ for odd TM modes. The integrals in (3.59), (3.60), and (3.65) must be determined numerically.

For TE modes, using (2.34), (2.35), (2.43), and (2.49) in (2.64) and making some substitutions gives

$$
\begin{aligned}
S_p^{TE} &= \int_\Omega (\hat{z} \times \boldsymbol{H}_t^i) \cdot \boldsymbol{E}_{tp} \mathrm{d}s \\
&= +G_0 \int_0^a J_c(k_r' r) \left[\int_0^{2\pi} \sin(c\phi) \sin(\phi) e^{-jk_0 r \sin\theta_i \cos(\phi - \phi_i)} \mathrm{d}\phi \right] \mathrm{d}r
\end{aligned}
$$

50

$$+G_1 \int_0^a rJ_c'(k_r'r)\left[\int_0^{2\pi}\cos(c\phi)\cos(\phi)e^{-jk_0r\sin\theta_i\cos(\phi-\phi_i)}\mathrm{d}\phi\right]\mathrm{d}r$$

$$-G_2 \int_0^a J_c(k_r'r)\left[\int_0^{2\pi}\sin(c\phi)\cos(\phi)e^{-jk_0r\sin\theta_i\cos(\phi-\phi_i)}\mathrm{d}\phi\right]\mathrm{d}r$$

$$+G_3 \int_0^a rJ_c'(k_r'r)\left[\int_0^{2\pi}\cos(c\phi)\sin(\phi)e^{-jk_0r\sin\theta_i\cos(\phi-\phi_i)}\mathrm{d}\phi\right]\mathrm{d}r$$

$$= +[G_1G_6+G_3G_4]\int_0^a rJ_c'(k_rr)J_{c+1}(k_0r\sin\theta_i)\mathrm{d}r$$

$$+[G_1G_7-G_3G_5]\int_0^a rJ_c'(k_rr)J_{c-1}(k_0r\sin\theta_i)\mathrm{d}r$$

$$-[G_0G_6+G_2G_4]\int_0^a J_c(k_rr)J_{c+1}(k_0r\sin\theta_i)\mathrm{d}r$$

$$+[G_0G_7-G_2G_5]\int_0^a J_c(k_rr)J_{c-1}(k_0r\sin\theta_i)\mathrm{d}r \qquad (3.66)$$

for even TE modes, and

$$S_p^{TE} = \int_\Omega (\hat{z}\times \boldsymbol{H}_t^i)\cdot \boldsymbol{E}_{tp}\mathrm{d}s$$

$$= -G_0 \int_0^a rJ_c'(k_rr)\left[\int_0^{2\pi}\cos(c\phi)\sin(\phi)e^{-jk_0r\sin\theta_i\cos(\phi-\phi_i)}\mathrm{d}\phi\right]\mathrm{d}r$$

$$+G_1 \int_0^a J_c(k_rr)\left[\int_0^{2\pi}\sin(c\phi)\cos(\phi)e^{-jk_0r\sin\theta_i\cos(\phi-\phi_i)}\mathrm{d}\phi\right]\mathrm{d}r$$

$$+G_2 \int_0^a rJ_c'(k_rr)\left[\int_0^{2\pi}\cos(c\phi)\cos(\phi)e^{-jk_0r\sin\theta_i\cos(\phi-\phi_i)}\mathrm{d}\phi\right]\mathrm{d}r$$

$$+G_3 \int_0^a J_c(k_rr)\left[\int_0^{2\pi}\sin(c\phi)\sin(\phi)e^{-jk_0r\sin\theta_i\cos(\phi-\phi_i)}\mathrm{d}\phi\right]\mathrm{d}r$$

$$= +[G_1G_4-G_3G_6]\int_0^a rJ_c'(k_rr)J_{c+1}(k_0r\sin\theta_i)\mathrm{d}r$$

$$+[G_1G_5+G_3G_7]\int_0^a rJ_c'(k_rr)J_{c-1}(k_0r\sin\theta_i)\mathrm{d}r$$

$$- [G_0 G_4 - G_2 G_6] \int_0^a J_c(k_r r) J_{c+1}(k_0 r \sin \theta_i) dr$$

$$+ [G_0 G_5 + G_2 G_7] \int_0^a J_c(k_r r) J_{c-1}(k_0 r \sin \theta_i) dr \qquad (3.67)$$

for odd TE modes, where

$$G_0 = \frac{j k_z Z_{hp} c E_0^i}{\eta_1 \sqrt{f_{ph}}} h_x,$$

$$G_1 = \frac{j k_z Z_{hp} k_r' E_0^i}{\eta_1 \sqrt{f_{ph}}} h_x,$$

$$G_2 = \frac{j k_z Z_{hp} c E_0^i}{\eta_1 \sqrt{f_{ph}}} h_y,$$

$$G_3 = \frac{j k_z Z_{hp} k_r' E_0^i}{\eta_1 \sqrt{f_{ph}}} h_y,$$

and $G_4, G_5, G_6,$ and G_7 are defined by (3.61), (3.62), (3.63), and (3.64), respectively. (3.66) and (3.67) are valid as long as $c \neq 0$. If $c = 0$,

$$
\begin{aligned}
S_p^{TE} &= \int_\Omega (\hat{z} \times \boldsymbol{H}_t^i) \cdot \boldsymbol{E}_{tp} ds \\
&= +G_1 \int_0^a r J_0'(k_r' r) \left[\int_0^{2\pi} \cos(\phi) e^{-j k_0 r \sin \theta_i \cos(\phi - \phi_i)} d\phi \right] dr \\
&\quad + G_3 \int_0^a r J_0'(k_r' r) \left[\int_0^{2\pi} \sin(\phi) e^{-j k_0 r \sin \theta_i \cos(\phi - \phi_i)} d\phi \right] dr \\
&= j 2\pi [G_1 \cos \phi_i + G_3 \sin \phi_i] \int_0^a r J_0'(k_r' r) J_1(k_0 r \sin \theta_i) dr \qquad (3.68)
\end{aligned}
$$

for even TE modes, and $S_p^{TE} = 0$ for odd TE modes. The integrals in (3.66), (3.67), and (3.68) must be determined numerically.

3.2.1.4   Computing P_{1pmn}, P_{2pmn}, Q_{1pmn}, and Q_{2pmn}

In order to evaluate P_{1pmn}, P_{2pmn}, Q_{1pmn}, and Q_{2pmn}, the same computations that were carried out previously for S_p are repeated.

To calculate P_{1pmn} for TM modes, using (2.4), (2.5), (2.17), (2.26), (2.28), and (2.42) in (2.65) gives

$$
\begin{aligned}
P_{1pmn}^{TM} &= \int_{\Omega} \boldsymbol{E}_{tp} \cdot \boldsymbol{R}_{1mn}^{*} ds \\
&= +G_2 \int_0^a r J_c'(k_r r) \left[\int_0^{2\pi} \cos(c\phi)\cos(\phi) e^{jr\zeta_{mn}\cos(\phi-\nu_{mn})} d\phi \right] dr \\
&\quad -G_0 \int_0^a r J_c'(k_r r) \left[\int_0^{2\pi} \cos(c\phi)\sin(\phi) e^{jr\zeta_{mn}\cos(\phi-\nu_{mn})} d\phi \right] dr \\
&\quad +G_3 \int_0^a J_c(k_r r) \left[\int_0^{2\pi} \sin(c\phi)\sin(\phi) e^{jr\zeta_{mn}\cos(\phi-\nu_{mn})} d\phi \right] dr \\
&\quad +G_1 \int_0^a J_c(k_r r) \left[\int_0^{2\pi} \sin(c\phi)\cos(\phi) e^{jr\zeta_{mn}\cos(\phi-\nu_{mn})} d\phi \right] dr \\
&= +[G_2 G_7 + G_0 G_5] \int_0^a r J_c'(k_r r) J_{c-1}(\zeta_{mn}r) dr \\
&\quad +[G_2 G_6 - G_0 G_4] \int_0^a r J_c'(k_r r) J_{c+1}(\zeta_{mn}r) dr \\
&\quad -[G_3 G_6 - G_1 G_4] \int_0^a J_c(k_r r) J_{c+1}(\zeta_{mn}r) dr \\
&\quad +[G_3 G_7 + G_1 G_5] \int_0^a J_c(k_r r) J_{c-1}(\zeta_{mn}r) dr
\end{aligned}
\tag{3.69}
$$

for even TM modes, and

$$
\begin{aligned}
P_{1pmn}^{TM} &= \int_{\Omega} \boldsymbol{E}_{tp} \cdot \boldsymbol{R}_{1mn}^{*} ds \\
&= +G_2 \int_0^a r J_c'(k_r r) \left[\int_0^{2\pi} \sin(c\phi)\cos(\phi) e^{jr\zeta_{mn}\cos(\phi-\nu_{mn})} d\phi \right] dr \\
&\quad -G_0 \int_0^a r J_c'(k_r r) \left[\int_0^{2\pi} \sin(c\phi)\sin(\phi) e^{jr\zeta_{mn}\cos(\phi-\nu_{mn})} d\phi \right] dr \\
&\quad -G_3 \int_0^a J_c(k_r r) \left[\int_0^{2\pi} \cos(c\phi)\sin(\phi) e^{jr\zeta_{mn}\cos(\phi-\nu_{mn})} d\phi \right] dr
\end{aligned}
$$

$$-G_1 \int_0^a J_c(k_r r) \left[\int_0^{2\pi} \cos(c\phi) \cos(\phi) e^{jr\zeta_{mn} \cos(\phi - \nu_{mn})} d\phi \right] dr$$

$$= + [G_2 G_5 - G_0 G_7] \int_0^a r J_c'(k_r r) J_{c-1}(\zeta_{mn} r) dr$$

$$+ [G_2 G_4 + G_0 G_6] \int_0^a r J_c'(k_r r) J_{c+1}(\zeta_{mn} r) dr$$

$$- [G_3 G_4 + G_1 G_6] \int_0^a J_c(k_r r) J_{c+1}(\zeta_{mn} r) dr$$

$$+ [G_3 G_5 - G_1 G_7] \int_0^a J_c(k_r r) J_{c-1}(\zeta_{mn} r) dr \tag{3.70}$$

for odd TM modes, where

$$G_0 = \frac{jk_z k_r \alpha_m}{\sqrt{A_s} \zeta_{mn} \sqrt{f_{pe}}},$$

$$G_1 = \frac{jk_z c \alpha_m}{\sqrt{A_s} \zeta_{mn} \sqrt{f_{pe}}},$$

$$G_2 = \frac{jk_z k_r \beta_{mn}}{\sqrt{A_s} \zeta_{mn} \sqrt{f_{pe}}},$$

$$G_3 = \frac{jk_z c \beta_{mn}}{\sqrt{A_s} \zeta_{mn} \sqrt{f_{pe}}},$$

$$G_4 = \pi j^{c+1} \sin[(c+1)\nu_{mn}], \tag{3.71}$$

$$G_5 = \pi j^{c-1} \sin[(c-1)\nu_{mn}], \tag{3.72}$$

$$G_6 = \pi j^{c+1} \cos[(c+1)\nu_{mn}], \tag{3.73}$$

$$G_7 = \pi j^{c-1} \cos[(c-1)\nu_{mn}], \tag{3.74}$$

$$\zeta_{mn} = \sqrt{\alpha_m^2 + \beta_{mn}^2},$$

$$\nu_{mn} = \arctan \frac{\beta_{mn}}{\alpha_m}.$$

(3.69) and (3.70) are valid as long as $c \neq 0$. If $c = 0$,

$$
\begin{aligned}
P_{1pmn}^{TM} &= \int_\Omega \boldsymbol{E}_{tp} \cdot \boldsymbol{R}_{1mn}^* \mathrm{d}s \\
&= +G_2 \int_0^a r J_0'(k_r r) \left[\int_0^{2\pi} \cos(\phi) e^{jr\zeta_{mn}\cos(\phi - \nu_{mn})} \mathrm{d}\phi \right] \mathrm{d}r \\
&\quad -G_0 \int_0^a r J_0'(k_r r) \left[\int_0^{2\pi} \sin(\phi) e^{jr\zeta_{mn}\cos(\phi - \nu_{mn})} \mathrm{d}\phi \right] \mathrm{d}r \\
&= j2\pi [G_0 \sin(\nu_{mn}) - G_2 \cos(\nu_{mn})] \int_0^a r J_0'(k_r r) J_1(k_0 r \sin\theta_i) \mathrm{d}r \quad (3.75)
\end{aligned}
$$

for even TM modes, and $P_{1pmn}^{TM} = 0$ for odd TM modes. The integrals in (3.69), (3.70), and (3.75) must be determined numerically.

For TE modes, using (2.4), (2.5), (2.17), (2.34), (2.35), and (2.43) in (2.65) gives

$$
\begin{aligned}
P_{1pmn}^{TE} &= \int_\Omega \boldsymbol{E}_{tp} \cdot \boldsymbol{R}_{1mn}^* \mathrm{d}s \\
&= -G_0 \int_0^a r J_c'(k_r' r) \left[\int_0^{2\pi} \cos(c\phi) \sin(\phi) e^{jr\zeta_{mn}\cos(\phi - \nu_{mn})} \mathrm{d}\phi \right] \mathrm{d}r \\
&\quad -G_2 \int_0^a r J_c'(k_r' r) \left[\int_0^{2\pi} \cos(c\phi) \cos(\phi) e^{jr\zeta_{mn}\cos(\phi - \nu_{mn})} \mathrm{d}\phi \right] \mathrm{d}r \\
&\quad +G_1 \int_0^a J_c(k_r' r) \left[\int_0^{2\pi} \sin(c\phi) \cos(\phi) e^{jr\zeta_{mn}\cos(\phi - \nu_{mn})} \mathrm{d}\phi \right] \mathrm{d}r \\
&\quad -G_3 \int_0^a J_c(k_r' r) \left[\int_0^{2\pi} \sin(c\phi) \sin(\phi) e^{jr\zeta_{mn}\cos(\phi - \nu_{mn})} \mathrm{d}\phi \right] \mathrm{d}r \\
&= +[G_0 G_5 - G_2 G_7] \int_0^a r J_c'(k_r r) J_{c-1}(\zeta_{mn} r) \mathrm{d}r \\
&\quad -[G_0 G_4 + G_2 G_6] \int_0^a r J_c'(k_r r) J_{c+1}(\zeta_{mn} r) \mathrm{d}r \\
&\quad +[G_1 G_4 + G_3 G_6] \int_0^a J_c(k_r r) J_{c+1}(\zeta_{mn} r) \mathrm{d}r
\end{aligned}
$$

$$+ [G_1 G_5 - G_3 G_7] \int_0^a J_c(k_r r) J_{c-1}(\zeta_{mn} r) dr \qquad (3.76)$$

for even TE modes, and

$$\begin{aligned}
P^{TE}_{1pmn} &= \int_\Omega \boldsymbol{E}_{tp} \cdot \boldsymbol{R}^*_{1mn} ds \\[2mm]
&= -G_0 \int_0^a r J'_c(k'_r r) \left[\int_0^{2\pi} \sin(c\phi) \sin(\phi) e^{jr\zeta_{mn} \cos(\phi - \nu_{mn})} d\phi \right] dr \\[2mm]
&\quad -G_2 \int_0^a r J'_c(k'_r r) \left[\int_0^{2\pi} \sin(c\phi) \cos(\phi) e^{jr\zeta_{mn} \cos(\phi - \nu_{mn})} d\phi \right] dr \\[2mm]
&\quad -G_1 \int_0^a J_c(k'_r r) \left[\int_0^{2\pi} \cos(c\phi) \cos(\phi) e^{jr\zeta_{mn} \cos(\phi - \nu_{mn})} d\phi \right] dr \\[2mm]
&\quad +G_3 \int_0^a J_c(k'_r r) \left[\int_0^{2\pi} \cos(c\phi) \sin(\phi) e^{jr\zeta_{mn} \cos(\phi - \nu_{mn})} d\phi \right] dr \\[2mm]
&= -[G_0 G_7 + G_2 G_5] \int_0^a r J'_c(k_r r) J_{c-1}(\zeta_{mn} r) dr \\[2mm]
&\quad + [G_0 G_6 - G_2 G_4] \int_0^a r J'_c(k_r r) J_{c+1}(\zeta_{mn} r) dr \\[2mm]
&\quad - [G_1 G_6 - G_3 G_4] \int_0^a J_c(k_r r) J_{c+1}(\zeta_{mn} r) dr \\[2mm]
&\quad - [G_1 G_7 + G_3 G_5] \int_0^a J_c(k_r r) J_{c-1}(\zeta_{mn} r) dr \qquad (3.77)
\end{aligned}$$

for odd TE modes, where

$$G_0 = \frac{jk_z k'_r Z_{hp} \beta_{mn}}{\sqrt{A_s} \zeta_{mn} \sqrt{f_{ph}}},$$

$$G_1 = \frac{jk_z Z_{hp} c \beta_{mn}}{\sqrt{A_s} \zeta_{mn} \sqrt{f_{ph}}},$$

$$G_2 = \frac{jk_z k'_r Z_{hp} \alpha_m}{\sqrt{A_s} \zeta_{mn} \sqrt{f_{ph}}},$$

$$G_3 = \frac{jk_z Z_{hp} c \alpha_m}{\sqrt{A_s} \zeta_{mn} \sqrt{f_{ph}}},$$

and $G_4, G_5, G_6,$ and G_7 are defined by (3.71), (3.72), (3.73), and (3.74), respectively. (3.76) and (3.77) are valid as long as $c \neq 0$. If $c = 0$,

$$
\begin{aligned}
P_{1pmn}^{TE} &= \int_\Omega \boldsymbol{E}_{tp} \cdot \boldsymbol{R}_{1mn}^* \mathrm{d}s \\
&= -G_0 \int_0^a r J_0'(k_r' r) \left[\int_0^{2\pi} \sin(\phi) e^{jr\zeta_{mn}\cos(\phi - \nu_{mn})} \mathrm{d}\phi \right] \mathrm{d}r \\
&\quad -G_2 \int_0^a r J_0'(k_r' r) \left[\int_0^{2\pi} \cos(\phi) e^{jr\zeta_{mn}\cos(\phi - \nu_{mn})} \mathrm{d}\phi \right] \mathrm{d}r \\
&= -j2\pi[G_0 \sin(\nu_{mn}) + G_2 \cos(\nu_{mn})] \int_0^a r J_0'(k_r' r) J_1(\zeta_{mn} r) \mathrm{d}r \quad (3.78)
\end{aligned}
$$

for even TE modes, and $P_{1pmn}^{TE} = 0$ for odd TE modes. The integrals in (3.76), (3.77), and (3.78) must be determined numerically.

To calculate P_{2pmn} for TM modes, using (2.4), (2.5), (2.18), (2.26), (2.28), and (2.42) in (2.66) gives

$$
\begin{aligned}
P_{2pmn}^{TM} &= \int_\Omega \boldsymbol{E}_{tp} \cdot \boldsymbol{R}_{2mn}^* \mathrm{d}s \\
&= +G_2 \int_0^a r J_c'(k_r r) \left[\int_0^{2\pi} \cos(c\phi) \cos(\phi) e^{jr\zeta_{mn}\cos(\phi - \nu_{mn})} \mathrm{d}\phi \right] \mathrm{d}r \\
&\quad +G_0 \int_0^a r J_c'(k_r r) \left[\int_0^{2\pi} \cos(c\phi) \sin(\phi) e^{jr\zeta_{mn}\cos(\phi - \nu_{mn})} \mathrm{d}\phi \right] \mathrm{d}r \\
&\quad -G_1 \int_0^a J_c(k_r r) \left[\int_0^{2\pi} \sin(c\phi) \cos(\phi) e^{jr\zeta_{mn}\cos(\phi - \nu_{mn})} \mathrm{d}\phi \right] \mathrm{d}r \\
&\quad +G_3 \int_0^a J_c(k_r r) \left[\int_0^{2\pi} \sin(c\phi) \sin(\phi) e^{jr\zeta_{mn}\cos(\phi - \nu_{mn})} \mathrm{d}\phi \right] \mathrm{d}r \\
&= -[G_0 G_5 - G_2 G_7] \int_0^a r J_c'(k_r r) J_{c-1}(\zeta_{mn} r) \mathrm{d}r
\end{aligned}
$$

$$+ \left[G_2 G_6 + G_0 G_4\right] \int\limits_0^a r J_c'(k_r r) J_{c+1}(\zeta_{mn} r) \mathrm{d}r$$

$$- \left[G_1 G_4 + G_3 G_6\right] \int\limits_0^a J_c(k_r r) J_{c+1}(\zeta_{mn} r) \mathrm{d}r$$

$$- \left[G_1 G_5 - G_3 G_7\right] \int\limits_0^a J_c(k_r r) J_{c-1}(\zeta_{mn} r) \mathrm{d}r \qquad (3.79)$$

for even TM modes, and

$$
\begin{aligned}
P_{2pmn}^{TM} &= \int\limits_\Omega \boldsymbol{E}_{tp} \cdot \boldsymbol{R}_{2mn}^* \mathrm{d}s \\
&= +G_2 \int\limits_0^a r J_c'(k_r r) \left[\int\limits_0^{2\pi} \sin(c\phi)\cos(\phi) e^{jr\zeta_{mn}\cos(\phi - \nu_{mn})} \mathrm{d}\phi\right] \mathrm{d}r \\
&\quad +G_0 \int\limits_0^a r J_c'(k_r r) \left[\int\limits_0^{2\pi} \sin(c\phi)\sin(\phi) e^{jr\zeta_{mn}\cos(\phi - \nu_{mn})} \mathrm{d}\phi\right] \mathrm{d}r \\
&\quad +G_1 \int\limits_0^a J_c(k_r r) \left[\int\limits_0^{2\pi} \cos(c\phi)\cos(\phi) e^{jr\zeta_{mn}\cos(\phi - \nu_{mn})} \mathrm{d}\phi\right] \mathrm{d}r \\
&\quad -G_3 \int\limits_0^a J_c(k_r r) \left[\int\limits_0^{2\pi} \cos(c\phi)\sin(\phi) e^{jr\zeta_{mn}\cos(\phi - \nu_{mn})} \mathrm{d}\phi\right] \mathrm{d}r \\
&= + \left[G_2 G_5 + G_0 G_7\right] \int\limits_0^a r J_c'(k_r r) J_{c-1}(\zeta_{mn} r) \mathrm{d}r \\
&\quad + \left[G_2 G_4 - G_0 G_6\right] \int\limits_0^a r J_c'(k_r r) J_{c+1}(\zeta_{mn} r) \mathrm{d}r \\
&\quad + \left[G_1 G_6 - G_3 G_4\right] \int\limits_0^a J_c(k_r r) J_{c+1}(\zeta_{mn} r) \mathrm{d}r \\
&\quad + \left[G_1 G_7 + G_3 G_5\right] \int\limits_0^a J_c(k_r r) J_{c-1}(\zeta_{mn} r) \mathrm{d}r \qquad (3.80)
\end{aligned}
$$

for odd TM modes, where

$$G_0 = \frac{jk_z k_r \beta_{mn}}{\sqrt{A_s}\zeta_{mn}\sqrt{f_{pe}}},$$

$$G_1 = \frac{jk_z c \beta_{mn}}{\sqrt{A_s}\zeta_{mn}\sqrt{f_{pe}}},$$

$$G_2 = \frac{jk_z k_r \alpha_m}{\sqrt{A_s}\zeta_{mn}\sqrt{f_{pe}}},$$

$$G_3 = \frac{jk_z c \alpha_m}{\sqrt{A_s}\zeta_{mn}\sqrt{f_{pe}}},$$

(3.79) and (3.80) are valid as long as $c \neq 0$. If $c = 0$,

$$
\begin{aligned}
P_{2pmn}^{TM} &= \int_\Omega \boldsymbol{E}_{tp} \cdot \boldsymbol{R}_{2mn}^* \mathrm{d}s \\
&= +G_0 \int_0^a r J_0'(k_r r) \left[\int_0^{2\pi} \cos(\phi) e^{jr\zeta_{mn}\cos(\phi - \nu_{mn})} \mathrm{d}\phi \right] \mathrm{d}r \\
&\quad +G_2 \int_0^a r J_0'(k_r r) \left[\int_0^{2\pi} \sin(\phi) e^{jr\zeta_{mn}\cos(\phi - \nu_{mn})} \mathrm{d}\phi \right] \mathrm{d}r \\
&= j2\pi[G_2 \cos(\nu_{mn}) + G_0 \sin(\nu_{mn})] \int_0^a r J_0'(k_r r) J_1(\zeta_{mn} r) \mathrm{d}r \quad (3.81)
\end{aligned}
$$

for even TM modes, and $P_{2pmn}^{TM} = 0$ for odd TM modes. The integrals in (3.79), (3.80), and (3.81) must be determined numerically.

For TE modes, using (2.4), (2.5), (2.18), (2.27), (2.35), and (2.43) in (2.66) gives

$$
\begin{aligned}
P_{2pmn}^{TE} &= \int_\Omega \boldsymbol{E}_{tp} \cdot \boldsymbol{R}_{2mn}^* \mathrm{d}s \\
&= +G_2 \int_0^a r J_c'(k_r' r) \left[\int_0^{2\pi} \cos(c\phi) \cos(\phi) e^{jr\zeta_{mn}\cos(\phi - \nu_{mn})} \mathrm{d}\phi \right] \mathrm{d}r \\
&\quad -G_0 \int_0^a r J_c'(k_r' r) \left[\int_0^{2\pi} \cos(c\phi) \sin(\phi) e^{jr\zeta_{mn}\cos(\phi - \nu_{mn})} \mathrm{d}\phi \right] \mathrm{d}r \\
&\quad +G_1 \int_0^a J_c(k_r' r) \left[\int_0^{2\pi} \sin(c\phi) \cos(\phi) e^{jr\zeta_{mn}\cos(\phi - \nu_{mn})} \mathrm{d}\phi \right] \mathrm{d}r \\
&\quad +G_3 \int_0^a J_c(k_r' r) \left[\int_0^{2\pi} \sin(c\phi) \sin(\phi) e^{jr\zeta_{mn}\cos(\phi - \nu_{mn})} \mathrm{d}\phi \right] \mathrm{d}r \\
&= +[G_2 G_7 + G_0 G_5] \int_0^a r J_c'(k_r r) J_{c-1}(\zeta_{mn} r) \mathrm{d}r
\end{aligned}
$$

$$+ [G_2 G_6 - G_0 G_4] \int\limits_0^a r J_c'(k_r r) J_{c+1}(\zeta_{mn} r) \mathrm{d}r$$

$$+ [G_1 G_4 - G_3 G_6] \int\limits_0^a J_c(k_r r) J_{c+1}(\zeta_{mn} r) \mathrm{d}r$$

$$+ [G_1 G_5 + G_3 G_7] \int\limits_0^a J_c(k_r r) J_{c-1}(\zeta_{mn} r) \mathrm{d}r \tag{3.82}$$

for even TE modes, and

$$
\begin{aligned}
P_{2pmn}^{TE} &= \int\limits_\Omega \boldsymbol{E}_{tp} \cdot \boldsymbol{R}_{2mn}^* \mathrm{d}s \\
&= + G_2 \int\limits_0^a r J_c'(k_r' r) \left[\int\limits_0^{2\pi} \sin(c\phi) \cos(\phi) e^{jr\zeta_{mn}\cos(\phi - \nu_{mn})} \mathrm{d}\phi \right] \mathrm{d}r \\
&\quad - G_0 \int\limits_0^a r J_c'(k_r' r) \left[\int\limits_0^{2\pi} \sin(c\phi) \sin(\phi) e^{jr\zeta_{mn}\cos(\phi - \nu_{mn})} \mathrm{d}\phi \right] \mathrm{d}r \\
&\quad - G_1 \int\limits_0^a J_c(k_r' r) \left[\int\limits_0^{2\pi} \cos(c\phi) \cos(\phi) e^{jr\zeta_{mn}\cos(\phi - \nu_{mn})} \mathrm{d}\phi \right] \mathrm{d}r \\
&\quad - G_3 \int\limits_0^a J_c(k_r' r) \left[\int\limits_0^{2\pi} \cos(c\phi) \sin(\phi) e^{jr\zeta_{mn}\cos(\phi - \nu_{mn})} \mathrm{d}\phi \right] \mathrm{d}r \\
&= + [G_2 G_5 - G_0 G_7] \int\limits_0^a r J_c'(k_r r) J_{c-1}(\zeta_{mn} r) \mathrm{d}r \\
&\quad + [G_2 G_4 + G_0 G_6] \int\limits_0^a r J_c'(k_r r) J_{c+1}(\zeta_{mn} r) \mathrm{d}r \\
&\quad - [G_1 G_6 + G_3 G_4] \int\limits_0^a J_c(k_r r) J_{c+1}(\zeta_{mn} r) \mathrm{d}r \\
&\quad - [G_1 G_7 - G_3 G_5] \int\limits_0^a J_c(k_r r) J_{c-1}(\zeta_{mn} r) \mathrm{d}r \tag{3.83}
\end{aligned}
$$

for odd TE modes, where

$$G_0 = \frac{j k_z k_r' Z_{hp} \alpha_m}{\sqrt{A_s} \zeta_{mn} \sqrt{f_{ph}}},$$

$$G_1 = \frac{j k_z Z_{hp} c \alpha_m}{\sqrt{A_s} \zeta_{mn} \sqrt{f_{ph}}},$$

60

$$G_2 = \frac{jk_z k_r' Z_{hp}\beta_{mn}}{\sqrt{A_s}\zeta_{mn}\sqrt{f_{ph}}},$$

$$G_3 = \frac{jk_z Z_{hp}c\beta_{mn}}{\sqrt{A_s}\zeta_{mn}\sqrt{f_{ph}}},$$

and $G_4, G_5, G_6,$ and G_7 are defined by (3.71), (3.72), (3.73), and (3.74), respectively. (3.82) and (3.83) are valid as long as $c \neq 0$. If $c = 0$,

$$
\begin{aligned}
P_{2pmn}^{TE} &= \int_\Omega \boldsymbol{E}_{tp} \cdot \boldsymbol{R}_{2mn}^* \mathrm{d}s \\
&= +G_2 \int_0^a rJ_0'(k_r'r) \left[\int_0^{2\pi} \cos(\phi)e^{jr\zeta_{mn}\cos(\phi-\nu_{mn})}\mathrm{d}\phi\right]\mathrm{d}r \\
&\quad -G_0 \int_0^a rJ_0'(k_r'r) \left[\int_0^{2\pi} \sin(\phi)e^{jr\zeta_{mn}\cos(\phi-\nu_{mn})}\mathrm{d}\phi\right]\mathrm{d}r \\
&= j2\pi[G_2\cos(\nu_{mn}) - G_0\sin(\nu_{mn})]\int_0^a rJ_0'(k_r'r)J_1(\zeta_{mn}r)\mathrm{d}r \quad (3.84)
\end{aligned}
$$

for even TE modes, and $P_{2pmn}^{TE} = 0$ for odd TE modes. The integrals in (3.82), (3.83), and (3.84) must be determined numerically.

In order to compute Q_{1pmn} and Q_{2pmn} for TM and TE modes, the formulas are identical to what has been shown for P_{1pmn} and P_{2pmn}. This is true despite the fact that $\boldsymbol{R}_{1mn}$ and $\boldsymbol{R}_{2mn}$ are used to compute Q_{1pmn} and Q_{2pmn} instead of $\boldsymbol{R}_{1mn}^*$ and $\boldsymbol{R}_{2mn}^*$.

3.2.2 Discussion of Results

At this time, numerical results for the circular aperture case are not available.

Table 3.1. Number of modes used to calculate the curves in Figure 3.3.

Thickness (mm)	Modes Used
1.1	60
2.2	60
4.4	60
7.7	30
8.8	30
9.9	30
18.0	6
26.0	4
40.0	2

Table 3.2. Cutoff frequencies for modes of square apertures.

Modes	Cut-off frequency f_c (GHz)
TE_{10}, TE_{01}	41.64
TM_{11}, TE_{11}	58.89
TE_{02}, TE_{20}	83.28
$TM_{12}, TM_{21}, TE_{12}, TE_{21}$	93.11
TM_{22}, TE_{22}	117.77
TE_{03}, TE_{30}	124.91
$TM_{13}, TM_{31}, TE_{13}, TE_{31}$	131.67
$TM_{23}, TM_{32}, TE_{23}, TE_{32}$	150.13
TE_{04}, TE_{40}	166.55
$TM_{14}, TM_{41}, TE_{14}, TE_{41}$	171.68
TM_{33}, TM_{33}	176.66
$TM_{24}, TM_{42}, TE_{24}, TE_{42}$	186.21
$TM_{34}, TM_{43}, TE_{34}, TE_{43}, TE_{05}, TE_{50}$	208.19
$TM_{15}, TM_{51}, TE_{15}, TE_{51}$	212.31
$TM_{25}, TM_{52}, TE_{25}, TE_{52}$	224.23
TM_{44}, TE_{44}	235.54
$TM_{35}, TM_{53}, TE_{35}, TE_{53}$	242.79
$TM_{45}, TM_{54}, TE_{45}, TE_{54}$	266.62
TM_{55}, TE_{55}	294.43
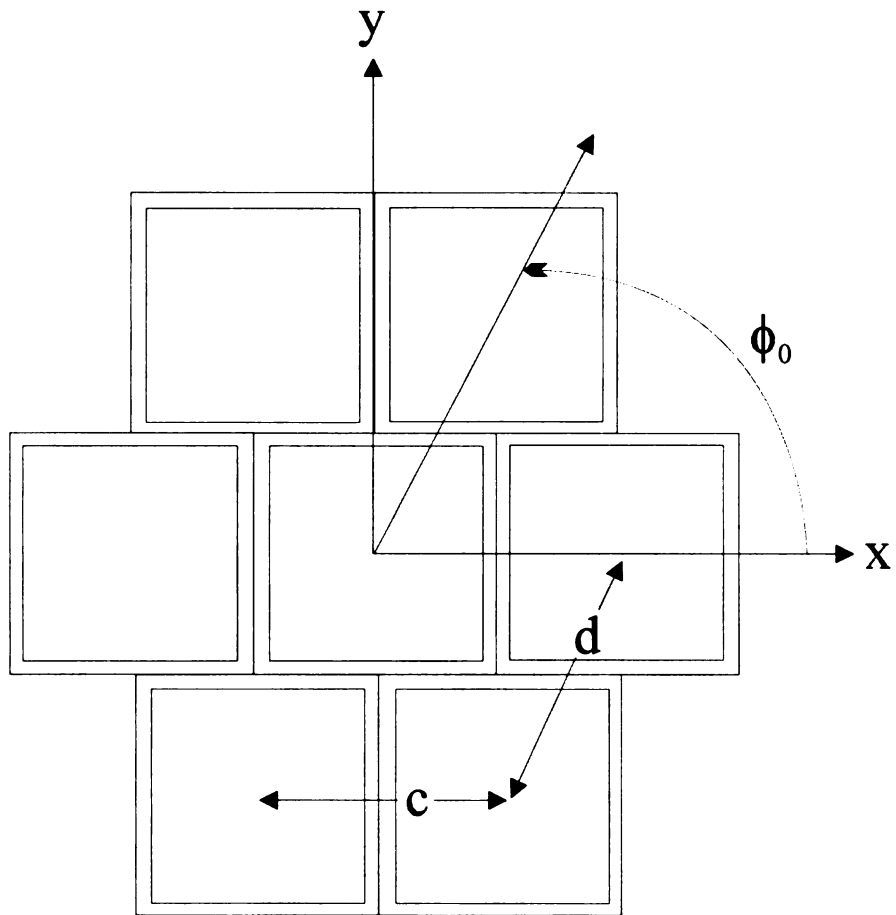
Figure 3.1. Doubly-periodic conducting screen of apertures with rectangular cross-section.
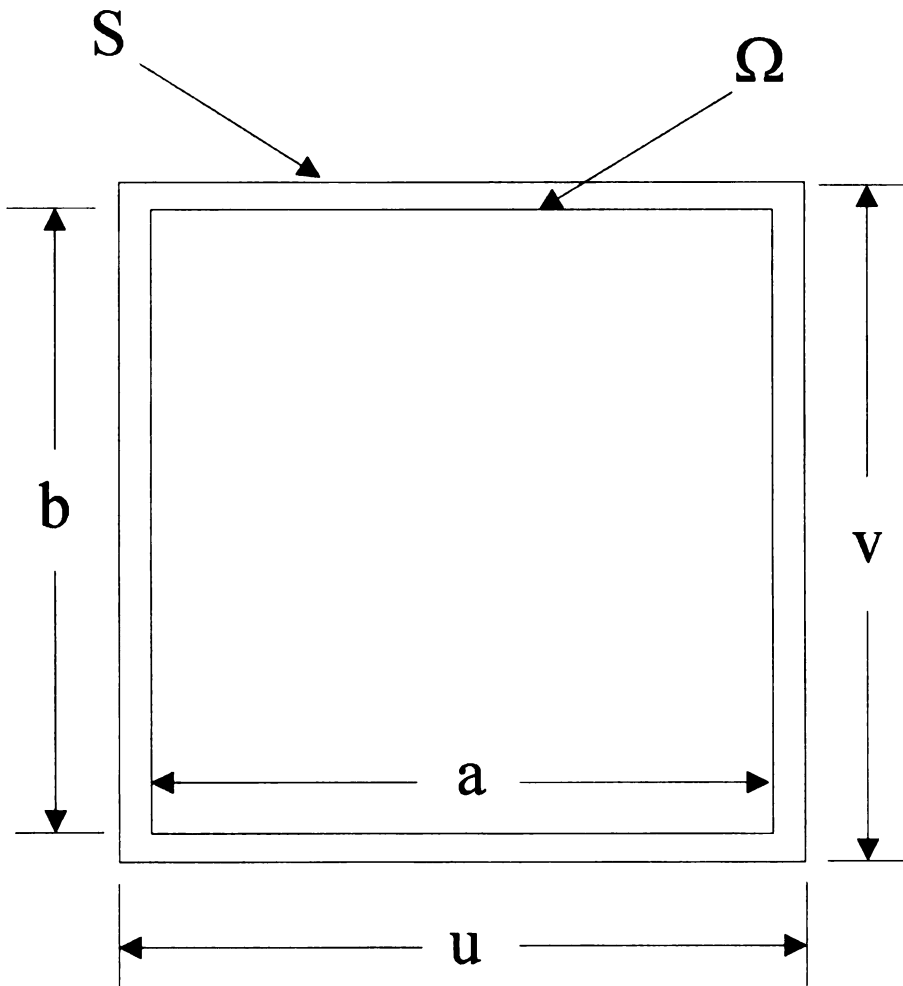
Figure 3.2. Unit cell for a doubly-periodic conducting screen of apertures with rectangular cross-section.
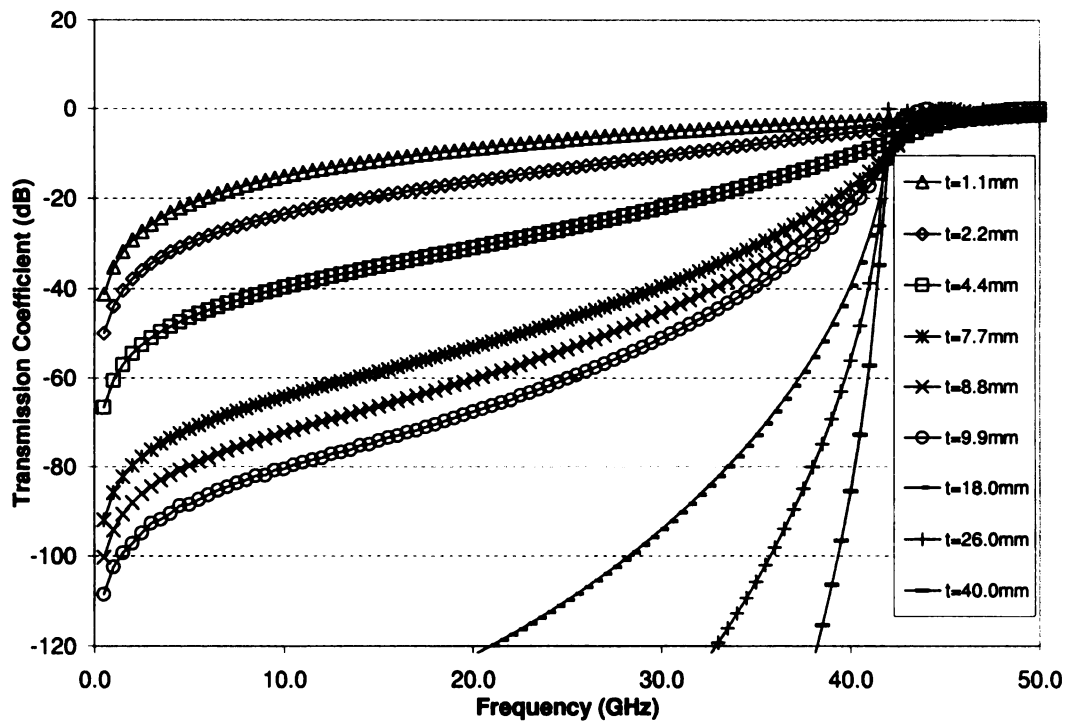
Figure 3.3. Comparison of transmission coefficient for screens of different thicknesses for normally incident TM polarized plane wave.
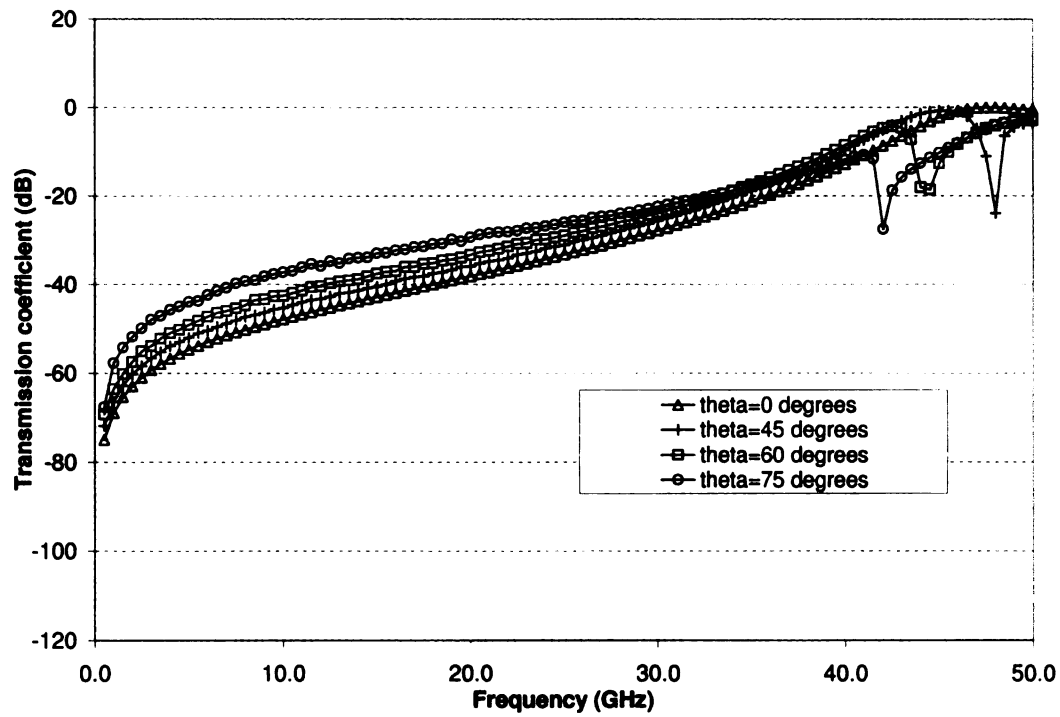
Figure 3.4. Comparison of transmission coefficient versus frequency for various incidence angles when t=5.5 mm for TM polarized incident plane wave.
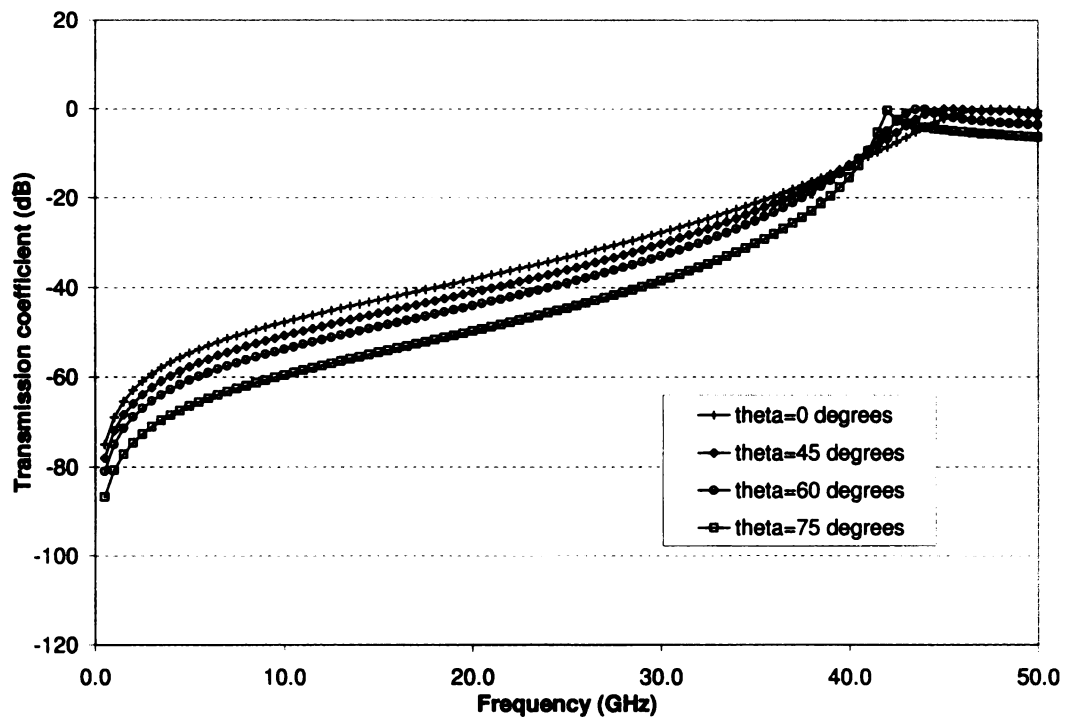
Figure 3.5. Comparison of transmission coefficient versus frequency for various incidence angles when t=5.5 mm for TE polarized incident plane wave.
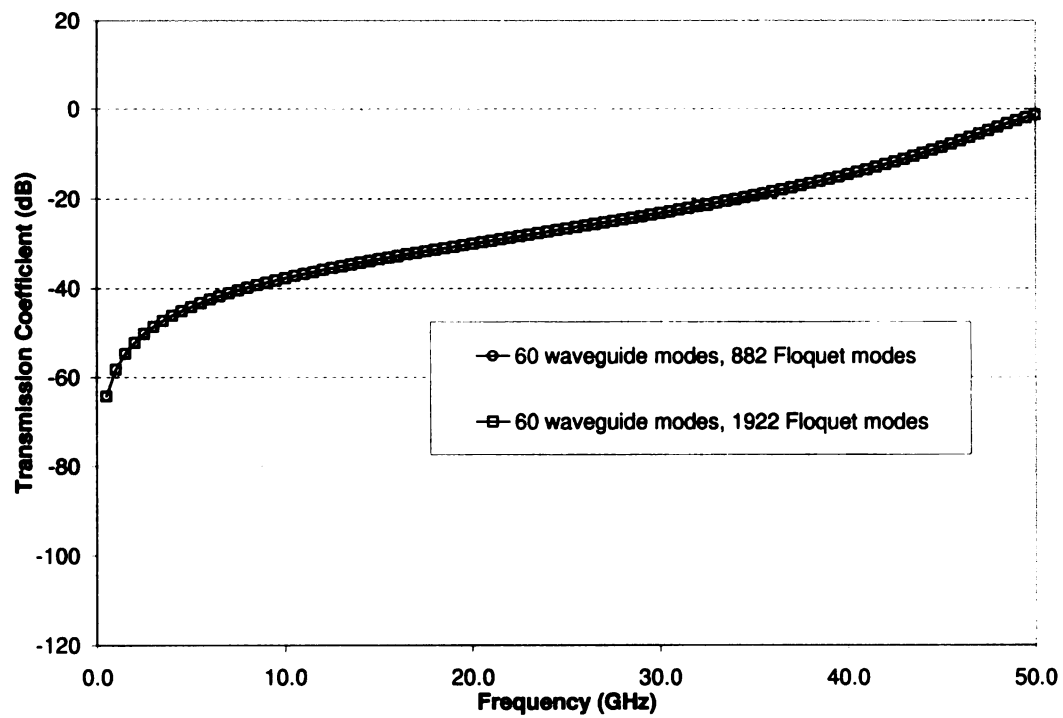
Figure 3.6. Comparison at t=4.4 mm between using 882 Floquet modes vs. 1922 Floquet modes.
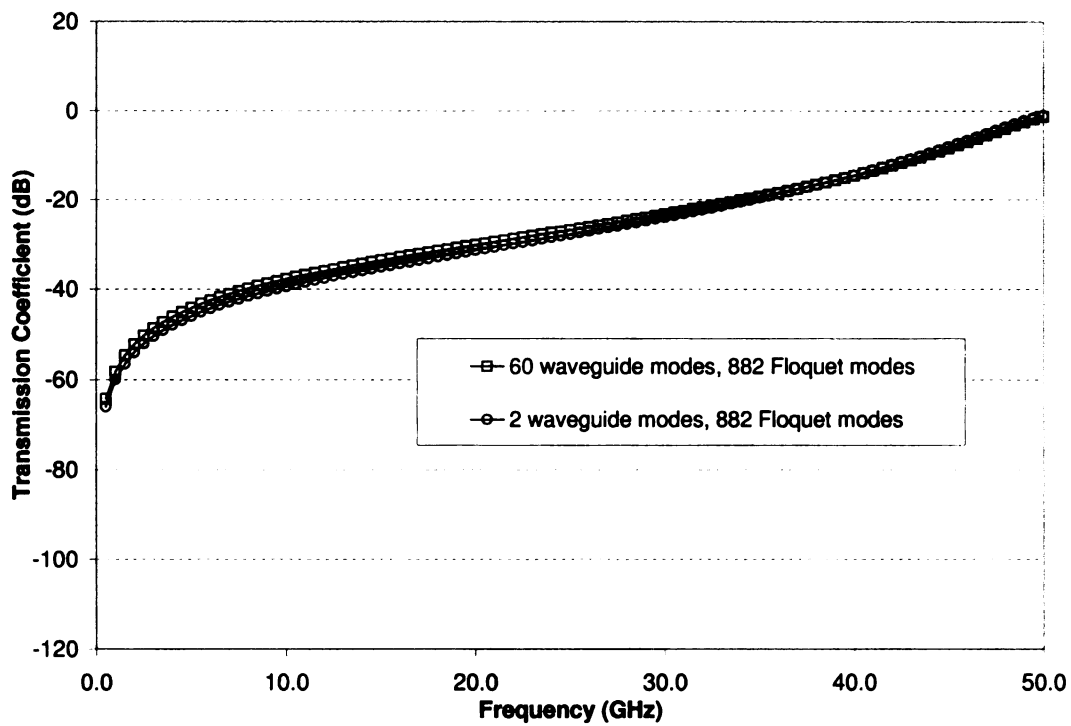
Figure 3.7. Comparison at t=4.4 mm between using 60 waveguide modes vs. 2 waveguide modes.
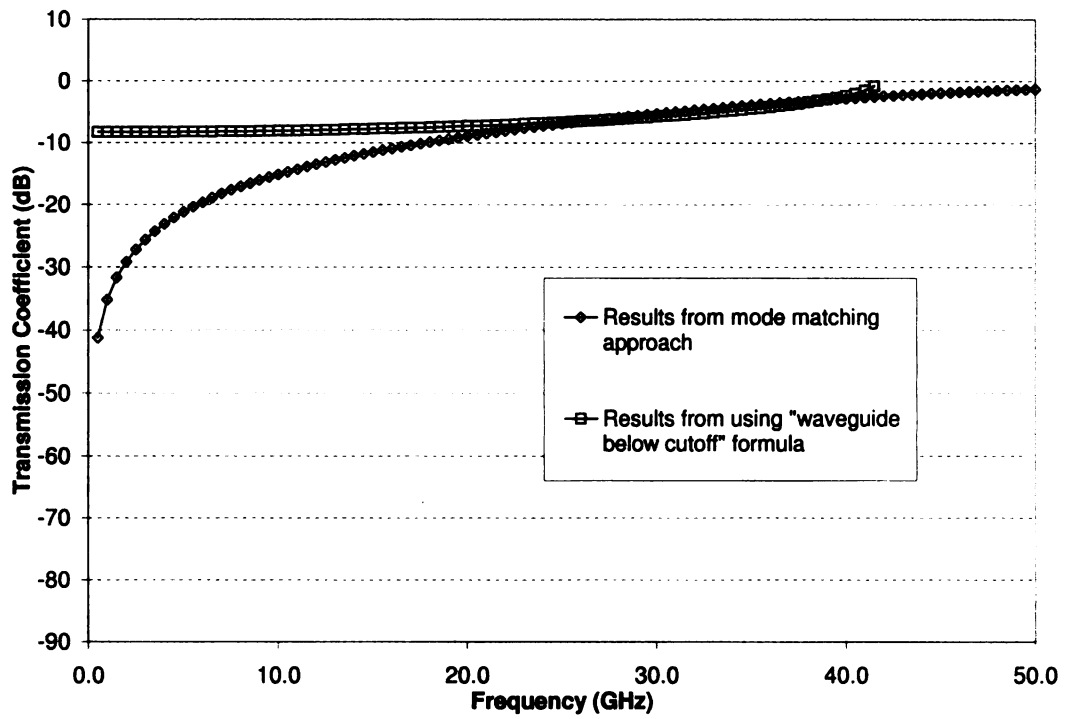
Figure 3.8. Comparison at t=1.1 mm between mode-matching approach and waveguide below cutoff formula.
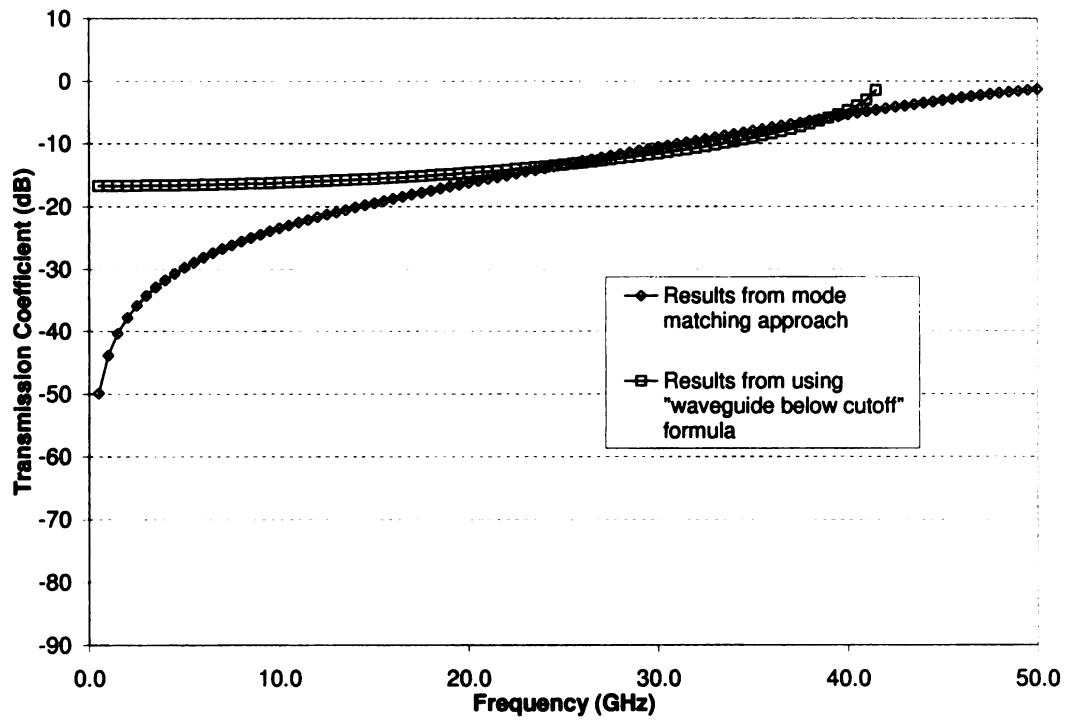
Figure 3.9. Comparison at t=2.2 mm between mode-matching approach and waveguide below cutoff formula.
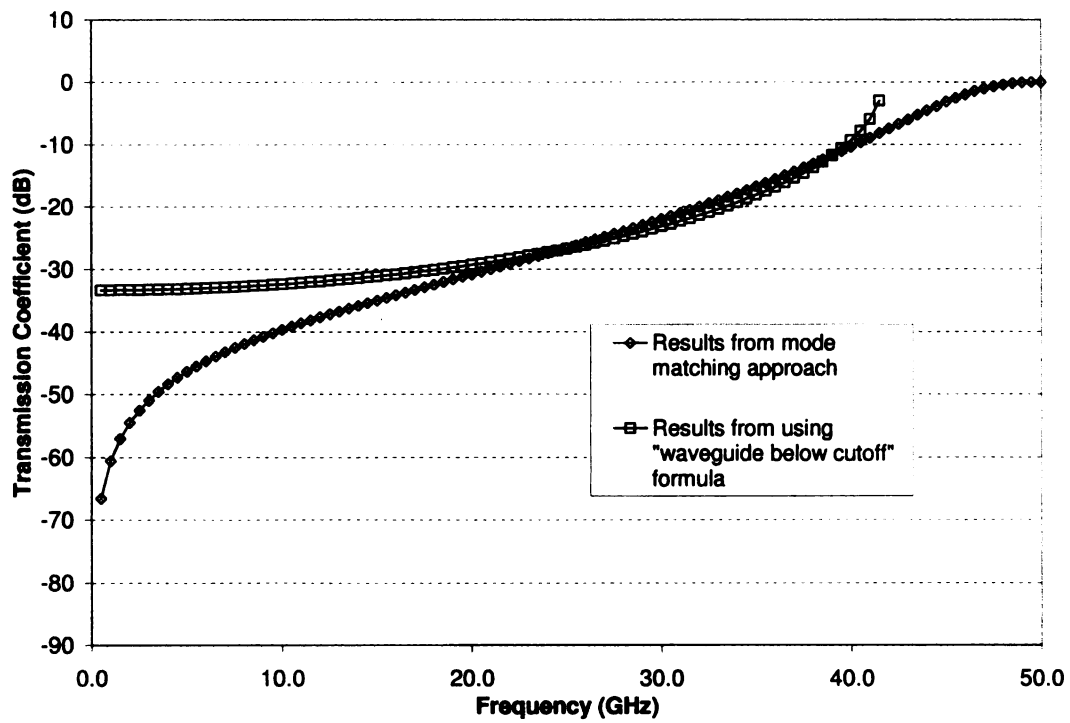
Figure 3.10. Comparison at t=4.4 mm between mode-matching approach and waveguide below cutoff formula.
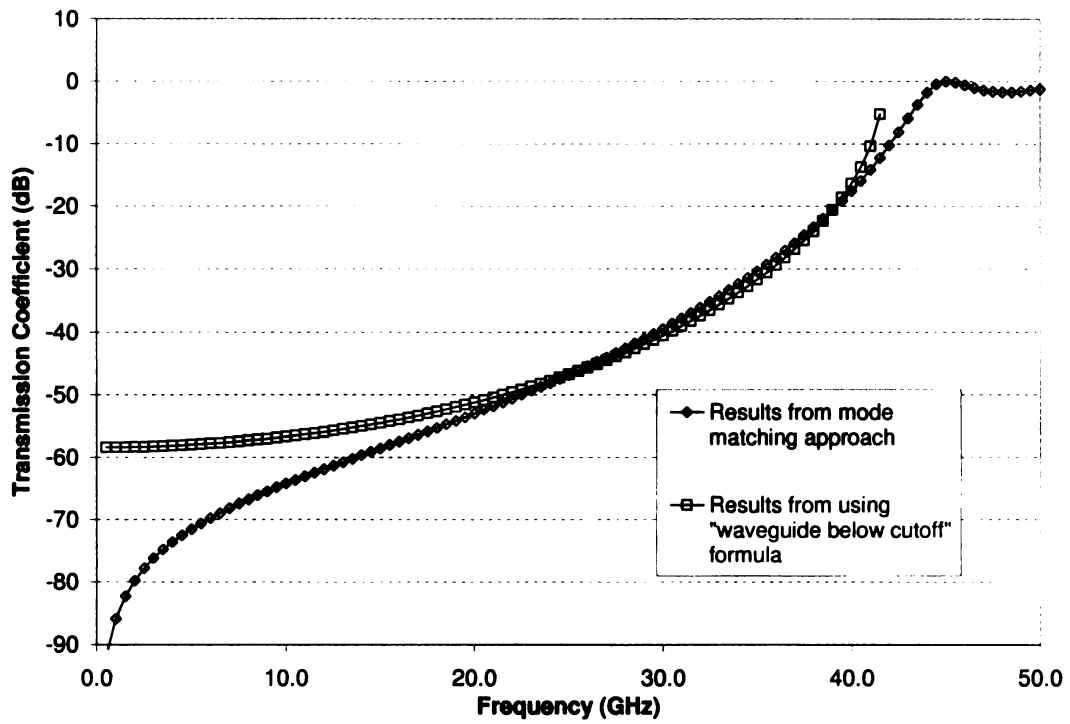
Figure 3.11. Comparison at t=7.7 mm between mode-matching approach and waveguide below cutoff formula.
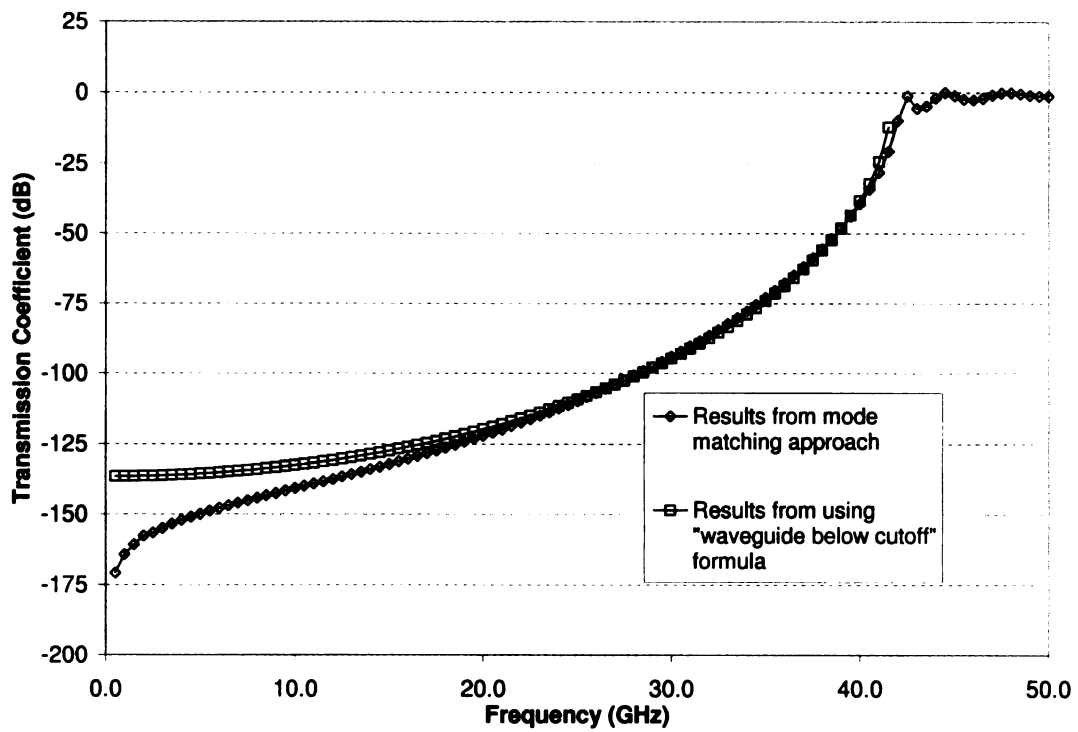
Figure 3.12. Comparison at t=18.0 mm between mode-matching approach and waveguide below cutoff formula.
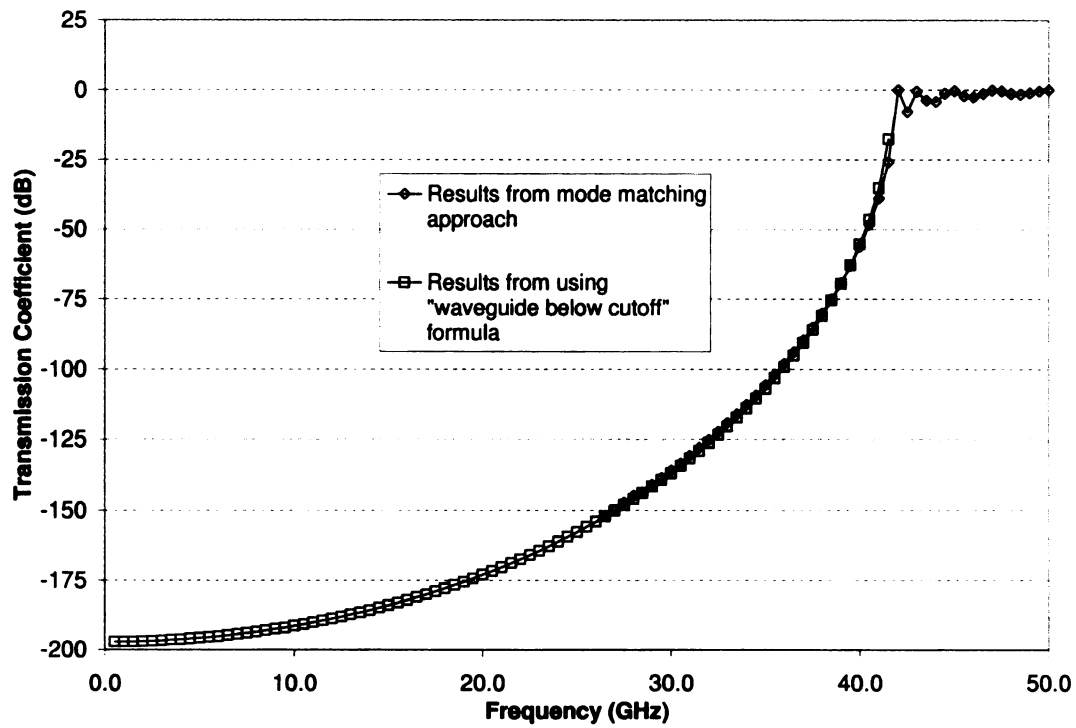
Figure 3.13. Comparison at t=26.0 mm between mode-matching approach and waveguide below cutoff formula.
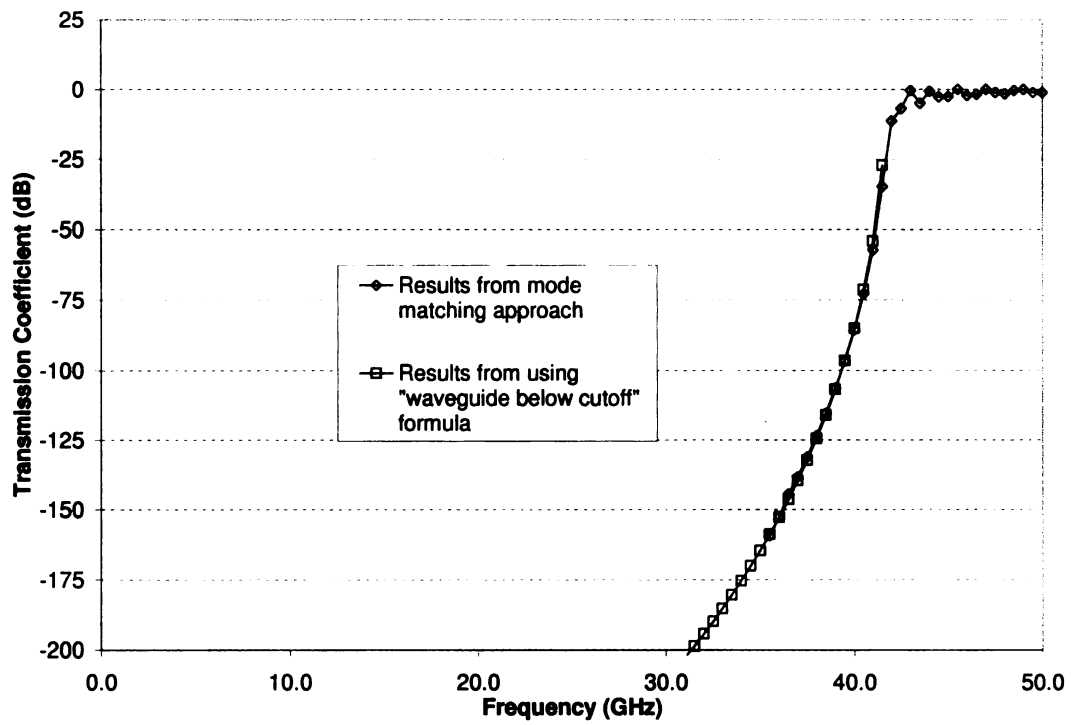
Figure 3.14. Comparison at t=40.0 mm between mode-matching approach and waveguide below cutoff formula.
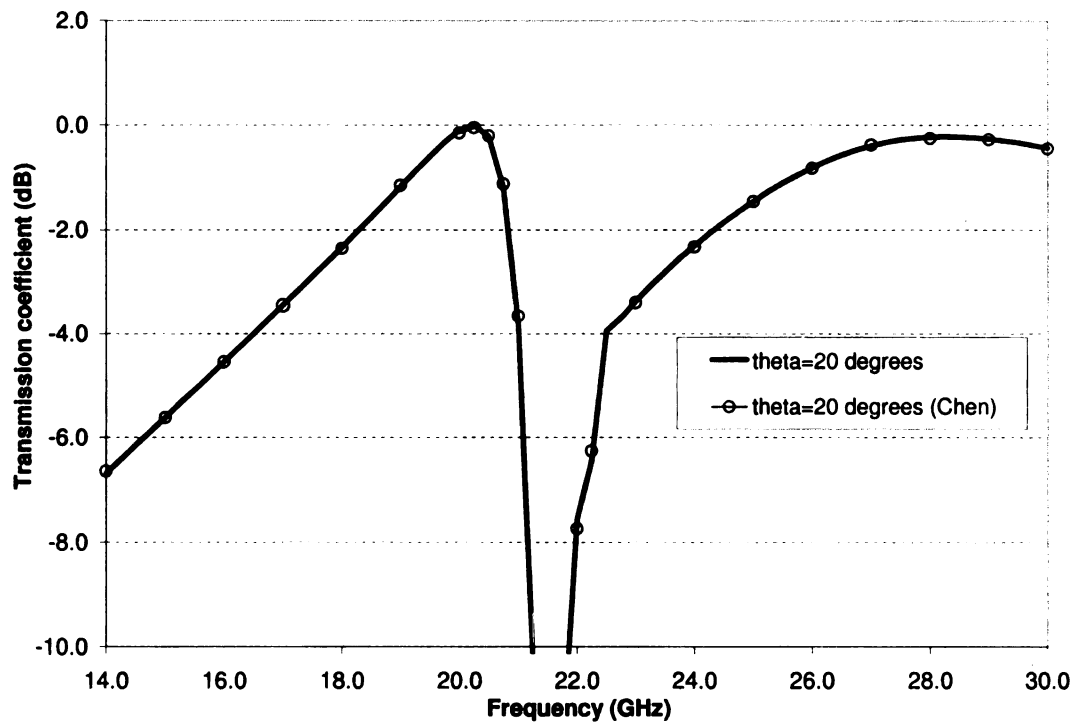
Figure 3.15. Comparison between proposed mode-matching formulation and mode–matching results of Chen using $\theta_i = 20°$ near transmission null (Wood's anomaly). Assumes only (0,0) Floquet mode is propagating.
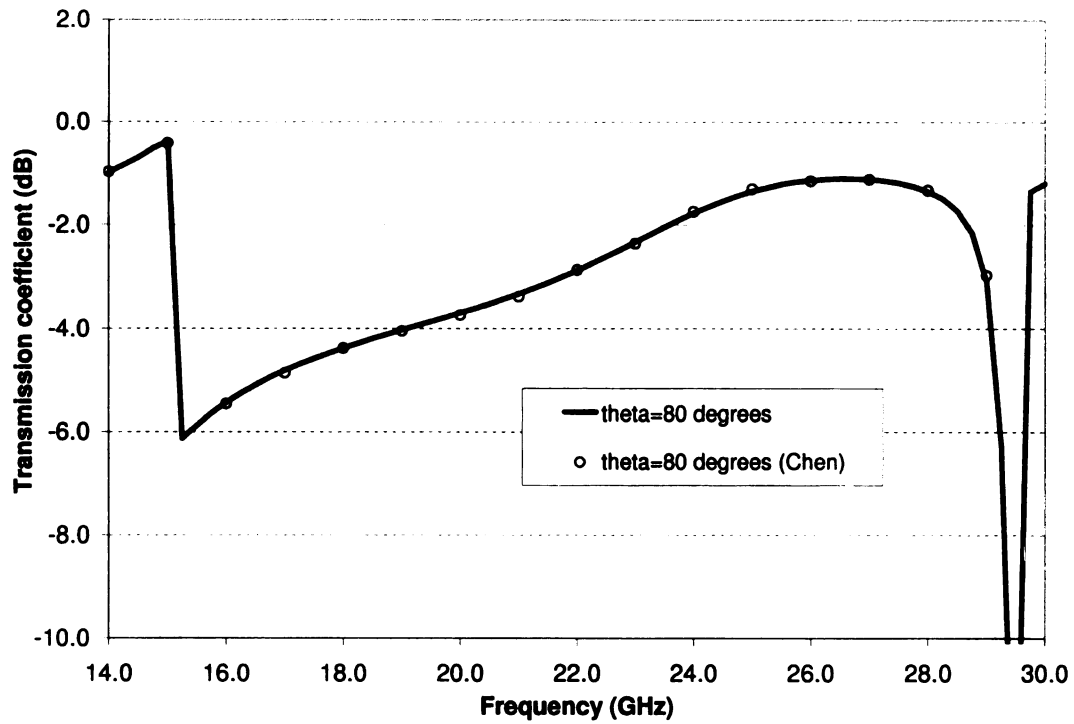
Figure 3.16. Comparison between proposed mode-matching formulation and mode-matching results of Chen using $\theta_i = 80°$ near transmission null (Wood's anomaly). Assumes only (0,0) Floquet mode is propagating.
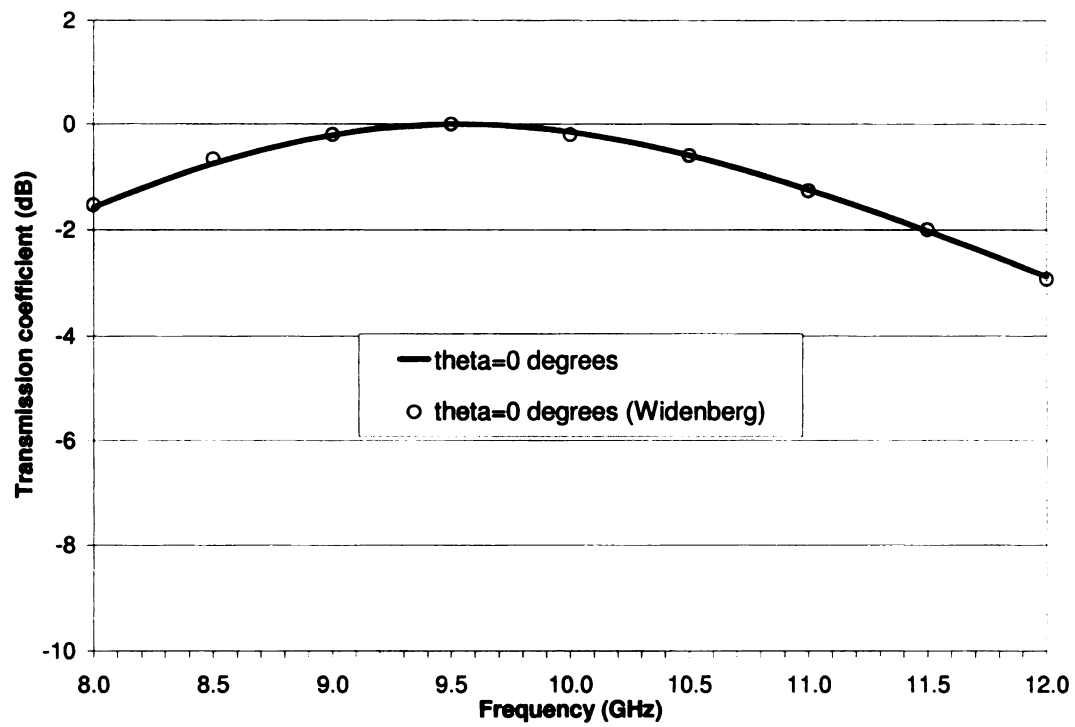
Figure 3.17. Comparison between proposed mode-matching formulation and mode–matching results from Widenberg et al using $\theta_i = 0°$.
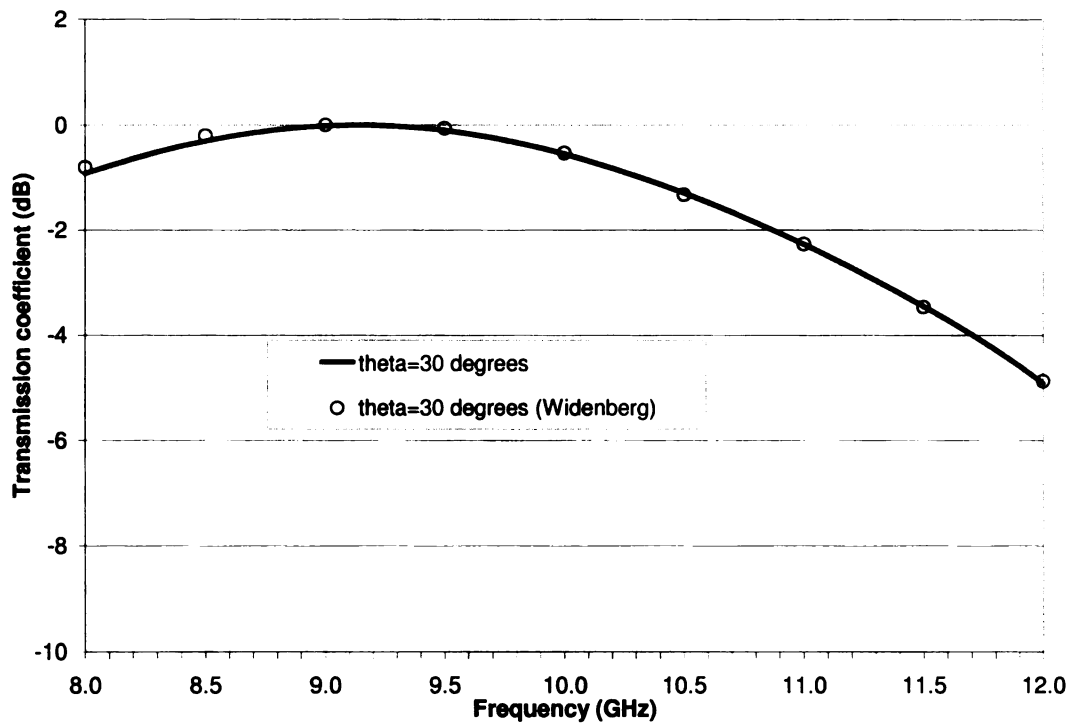
Figure 3.18. Comparison between proposed mode-matching formulation and mode-matching results from Widenberg et al using $\theta_i = 30°$.
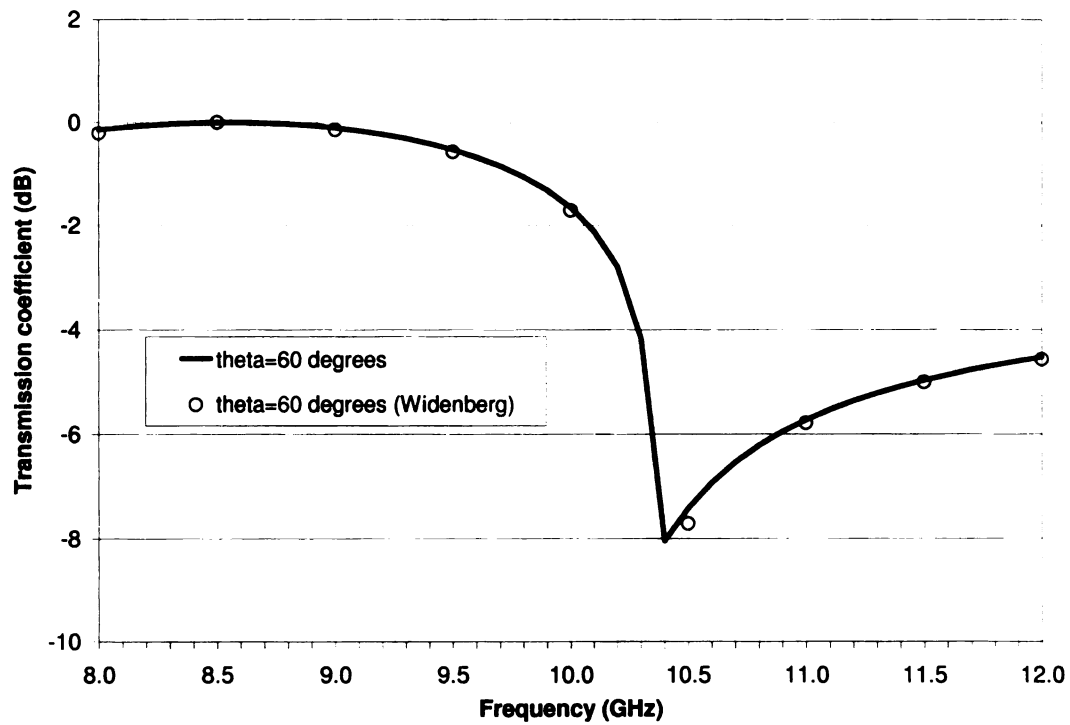
Figure 3.19. Comparison between proposed mode-matching formulation and mode-matching results from Widenberg et al using $\theta_i = 60°$ near transmission null (Wood's anomaly). Assumes only (0,0) Floquet mode is propagating.
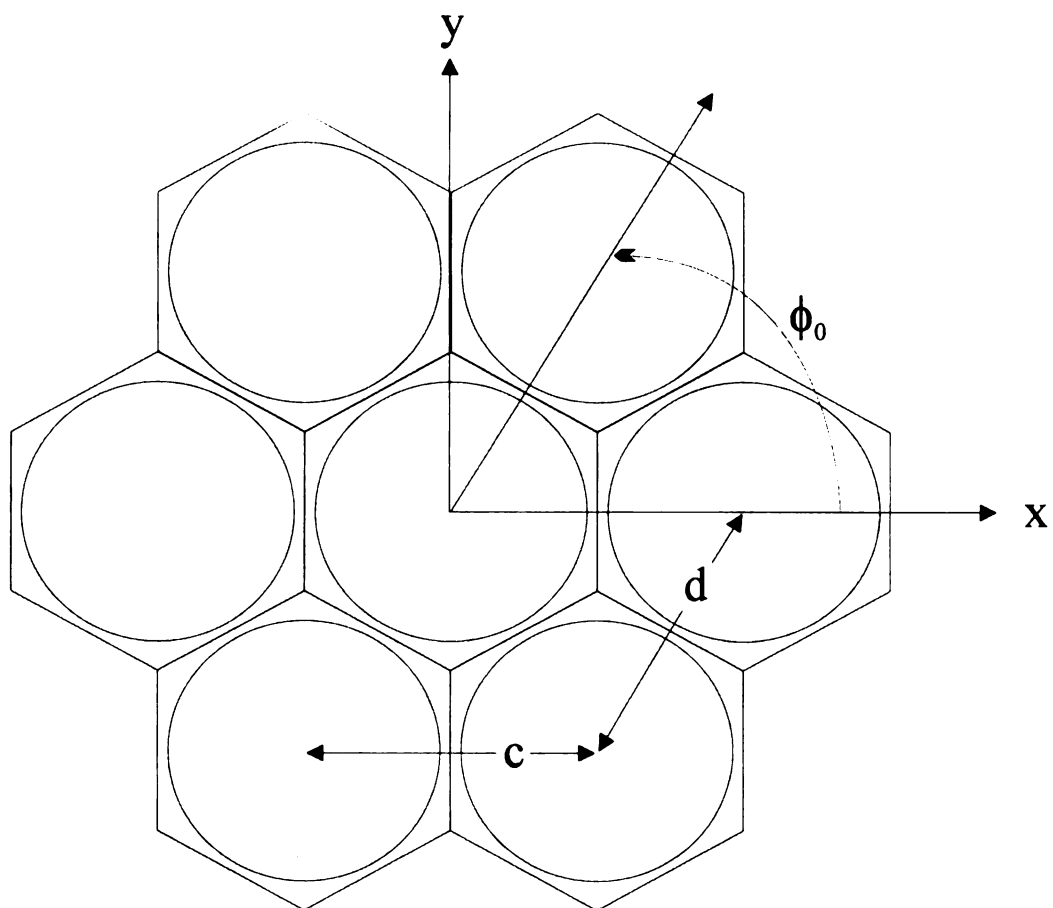
Figure 3.20. Doubly-periodic conducting screen of apertures with circular cross-section.
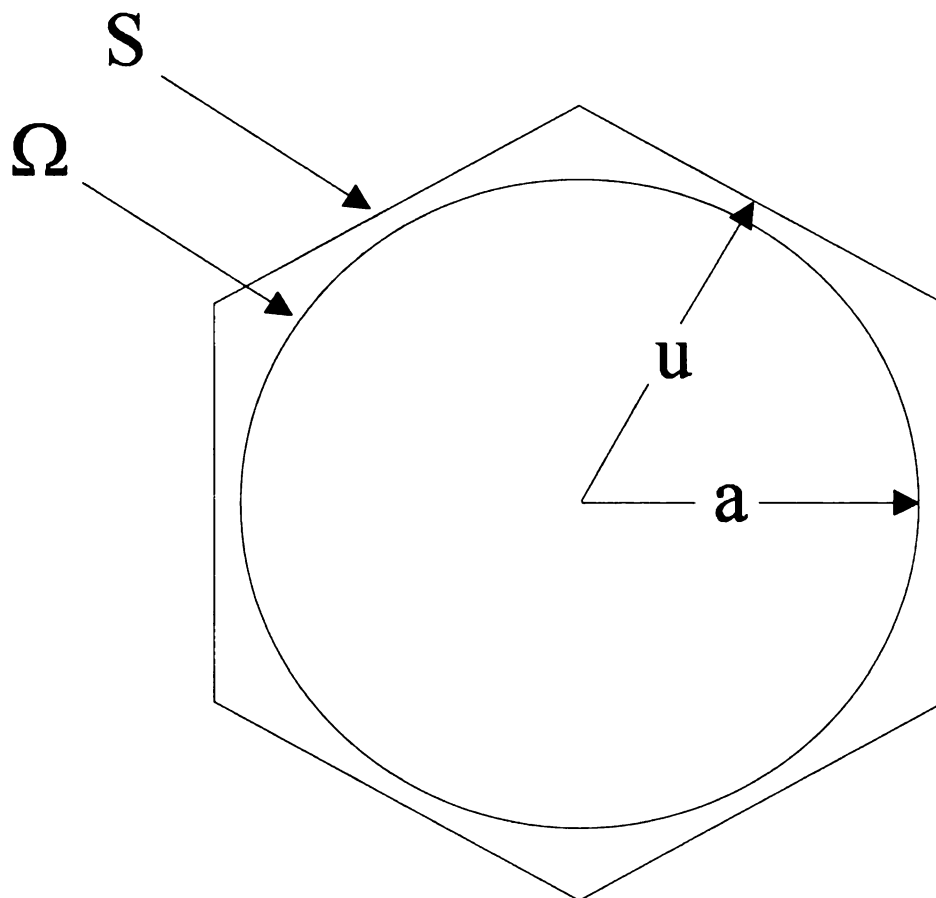
Figure 3.21. Hexagonal unit cell for a doubly-periodic conducting screen of apertures with circular cross-section.

CHAPTER 4

EXPERIMENTAL RESULTS

4.1 Setup

4.1.1 Sample Materials

As a means of comparing the numerical results with measured data, an experiment was set up in order to test the mode-matching approach against actual measurements to determine how well it can predict shielding performance [31]. Samples of commercial-grade aluminum honeycomb were used in the experiment. The honeycomb was available with rectangular apertures and hexagonal apertures. The rectangular aperture sample, which was supplied by Benecor, Inc. of Wichita, KS, is about 2 ft. in length and width, and approximately 1/2 inch in thickness. The apertures are square with about 1/4 inch in length and width. The hexagonal aperture sample, which was supplied by Plascore, Inc. of Zeeland, MI, is about 1 ft. in length and width while the thicknesses is approximately 13/16 in. The aperture cell size is about 3/4 in. The foil thickness for all of the samples is approximately 0.003 in. (3 mils).

4.1.2 Equipment

An HP8510C Network Analyzer was used to perform frequency domain transmission measurements. For samples whose apertures have a dominant mode cut-off frequency in the range of 2-18 GHz, the Michigan State University arch range was used along with American Electronic Laboratories H-1498 horn antennas for transmitting and receiving. Figure 4.1 shows a sketch of the low frequency measurement set-up, including the arch range, the network analyzer, the antennas, and the sample being tested. The arch range, designed and built by the Georgia Tech Research Institute, is a metallic structure 20 ft. in diameter and 4 ft. high. The receiving and transmitting antennas are connected to the network analyzer using coaxial cables, and lenses are

used to collimate the transmit and receive beams. The sample was mounted into an empty window in a styrofoam board, and the rest of the board was covered with aluminum tape (see Figure 4.2 for a description). The board is 4 ft. high, 4 ft. wide, and 1 in. thick. This approach is similar to the one mentioned in [32] to measure the shielding effectiveness of composite material samples. Mounting the sample in a board allowed for reducing the effect of a large beam spot size at low frequencies. The board was then placed onto a styrofoam mount between the transmit and receive antennas.

For samples whose apertures had a dominant mode cut-off frequency in the range of 20-40 GHz, a benchtop set-up was used to conduct the experiment. See Figure 4.3 for a sketch of the high frequency measurement set-up. The 8510C network analyzer was connected to two EMCO 3116 horn antennas with K-type connector cables. Just as with the arch range set-up, the samples were placed into windows in 4' x 4' x 1" styrofoam boards, and the rest of the board was covered with aluminum tape. A styrofoam mount was used to position the board containing the sample. The cables that were used with the high frequency horns were about 3 ft. long, so the transmit and receive antennas were about 2 ft. from each other, with the sample in the middle. For horn antennas to be operating in the far-zone, the wave must travel a distance larger than $z = 2D^2/\lambda_0$, where D is the largest dimension of the antenna and λ_0 is the free-space wavelength at the frequency of interest. For the 2-18 GHz range, the distance $2D^2/\lambda_0$ ranges from 0.7 ft at 2 GHz to 6.34 ft at 18 GHz. The distance between the horn antenna and the sample is approximately 10 ft, so the far-zone requirement is achieved for the low-frequency case. For the 20-40 GHz range, the distance $2D^2/\lambda_0$ ranges from 4.8 ft at 20 GHz to 9.6 ft at 40 GHz. These values are both larger than the distance between the antennas and the sample, so the set-up does not meet the far-zone requirement. However, despite the fact that the horns are not in the far-zone, the agreement between numerical and experimental results is still

pretty good.

4.2 Procedure

4.2.1 Low Frequency Measurements

For all measurements, a two-level calibration was conducted. The first level involved calibrating the network analyzer using the appropriate standards. For the low frequency measurements, the standards were applied to the ends of the 2.4 mm connection cables. From the ends of the 2.4 mm connection cables, connector adapters were used to go from 2.4 mm to 3.5 mm to SMA. Coaxial cables with SMA connectors were used to link the 8510C with the transmit and receive antennas, both of which use SMA connectors. The second level of calibration involved taking two transmission measurements in addition to the sample measurement. The first is an empty measurement, which in this case is a measurement with the window in the board being empty (no sample). The second is a noise measurement, where a board of the same size as the one with the window is used to perform a transmission measurement. This board is completely covered with aluminum tape. The noise measurement includes the effects of diffraction of the transmitted wave around the edges of the measurement board. The use of the three measurements will be explained in the calculations section.

4.2.2 High Frequency Measurements

For all measurements, a two-level calibration was conducted. The first level involved calibrating the network analyzer and cables using the appropriate standards. From the ends of the 2.4 mm connection cables, connector adapters were used to go from 2.4 mm to 3.5 mm to K. Cables with K-type connectors were used to link the 8510C with the transmit and receive antennas, both of which use K-type connectors. And due to the compatibility of 3.5 mm connectors and K-type connectors, 3.5 mm calibration standards were used to calibrate to the ends of the K-type connector cables.

As was the case with the low frequency experiment, the second level of calibration involved taking empty and noise measurements in addition to the sample measurement.

4.3   Calculations

To determine the tranmission coefficient at a particular frequency, the three measurements that are used are

S_{sample} — Measured transmission S-parameter for sample in window,

S_{noise} — Measured transmission S-parameter for blocking plate,

S_{empty} — Measured transmission S-parameter for empty window,

where S_{12} or S_{21} can be used depending on the set-up. Using those three values, the transmission coefficient is defined as

$$T_{dB} = -SE_{dB} = 20 \log_{10} \left| \frac{S_{sample} - S_{noise}}{S_{empty} - S_{noise}} \right|. \tag{4.1}$$

It should be noted that because of the use of S-parameter measurements in (4.1), $20 \log_{10}$ is used instead of $10 \log_{10}$ because S-parameters are analogous to voltage and current measurements. By contrast, (2.77) and (2.78) use $10 \log_{10}$ because power quantities are involved.

4.4   Discussion of Results

Figure 4.4 shows a comparison between numerical and experimental data for a screen of rectangular apertures (Benecor sample). The apertures are square shaped with a width of 1/4 in. (approximately 6 mm). The screen thickness is about 1/2 in. (approximately 13 mm). Overall, there is pretty good agreement in terms of the

transition from low transmission (below -20 dB) to full transmission. This case, as with all others in this section, is for normal incidence.

Figure 4.5 shows a comparison between numerical and experimental data for a screen of hexagonal apertures (Plascore sample). The apertures have a width of 3/4 in. (approximately 19 mm) between parallel sides. The screen thickness is about 13/16 in. (approximately 21 mm). Square apertures of the same width are used to model the hexagonal apeture sample, and the results are in good agreement with the measured data. It is anticipated that once results are available, the use of circular apertures may prove to be even closer to the measured result. It should also be noted that this data was obtained despite large losses in measured power due to attenuation in the coaxial cables.

In both cases, the measured data goes above the 0 dB mark, which at first does not seem reasonable. However, the contribution to transmission due to diffraction around the edges of the screen could lead to that kind of behavior. In general, the measured and numerical data are in good agreement. It is also worth noting that in the context of a shielding application, where the frequency range of operation would be well below the point where full transmission occurs, the effects due to edge diffraction are not expected to be as significant.
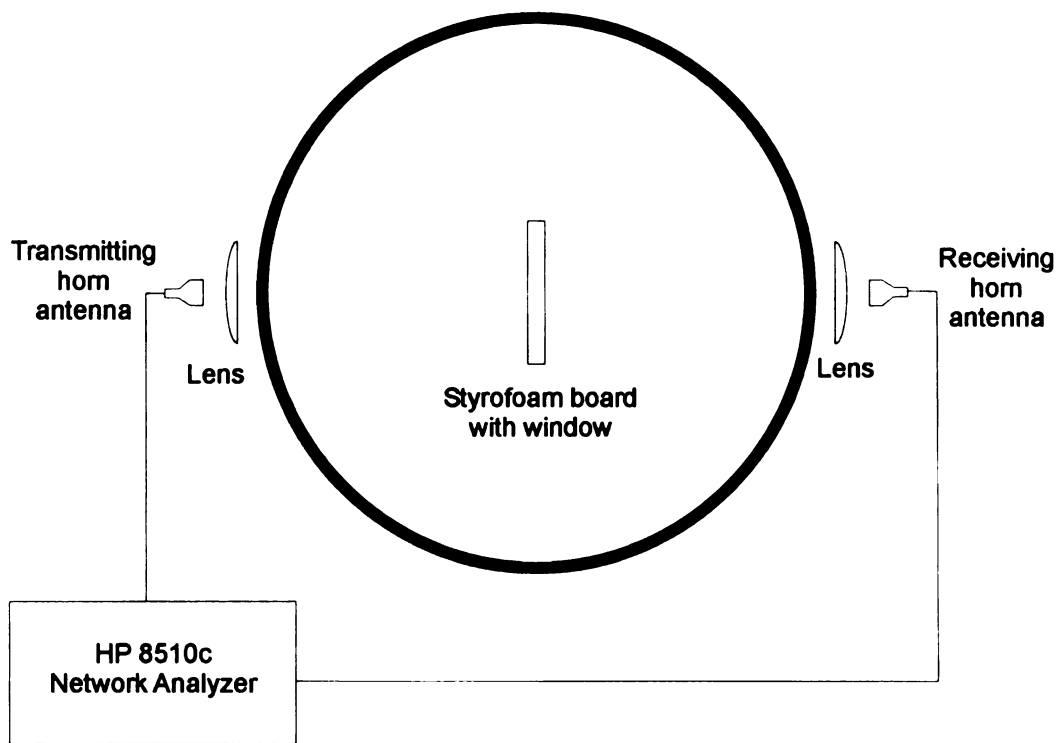
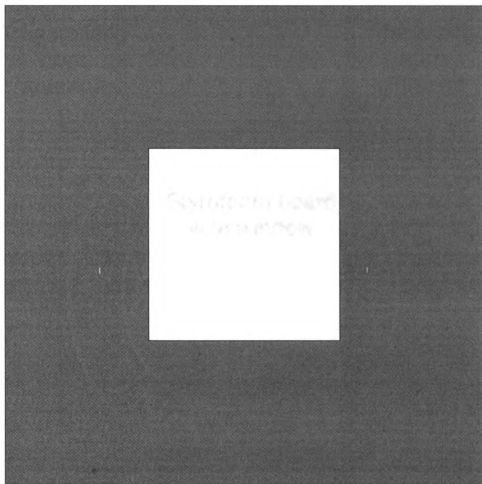Figure 4.1. Equipment arrangement for taking low frequency measurements (2-18 GHz)

Figure 4.2. Styrofoam board with window used to hold aluminum honeycomb samples. The dark grey region is covered with foil tape.
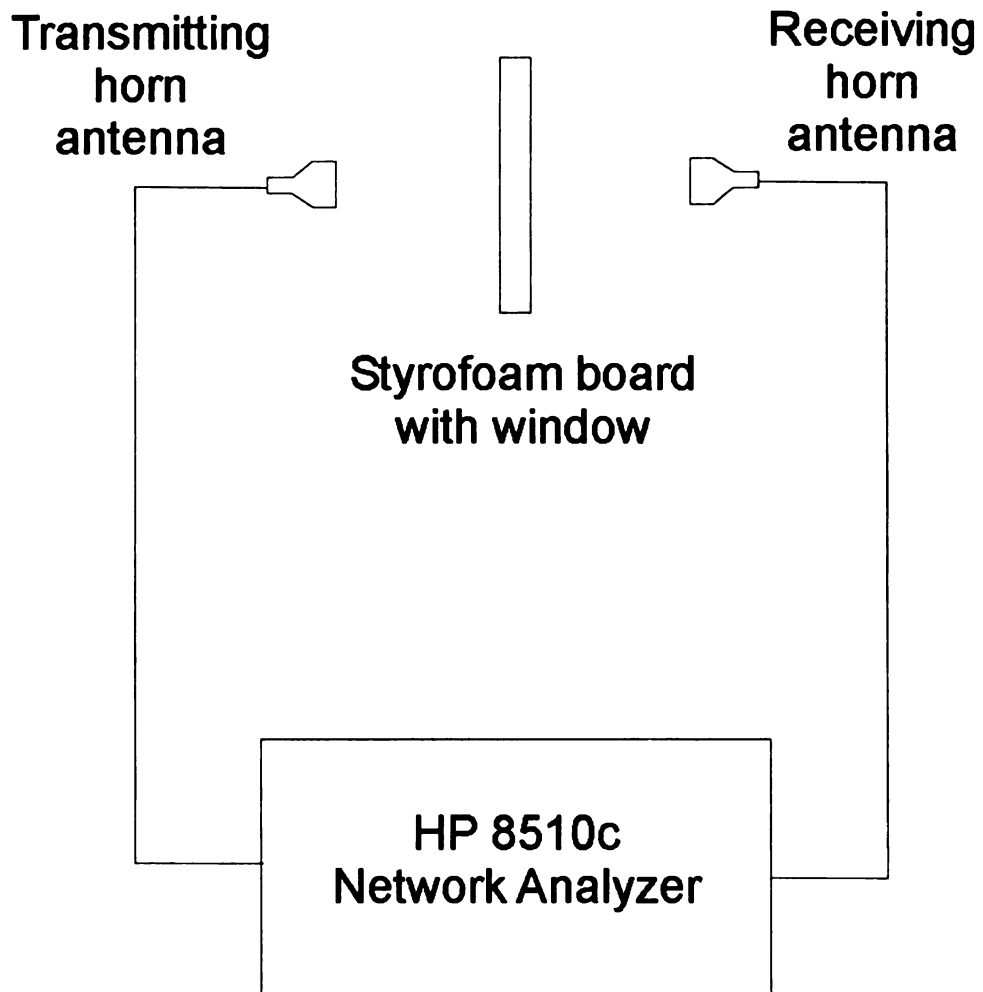
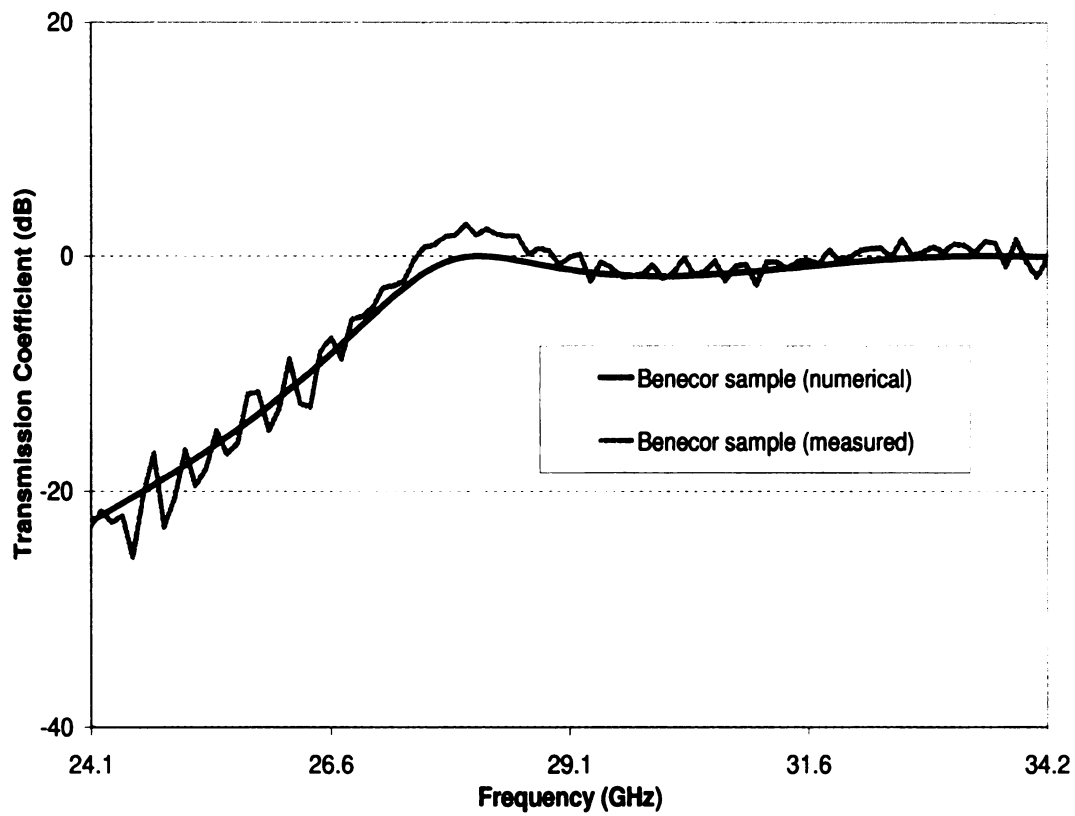Figure 4.3. Equipment arrangement for taking high frequency measurements (20-40 GHz)

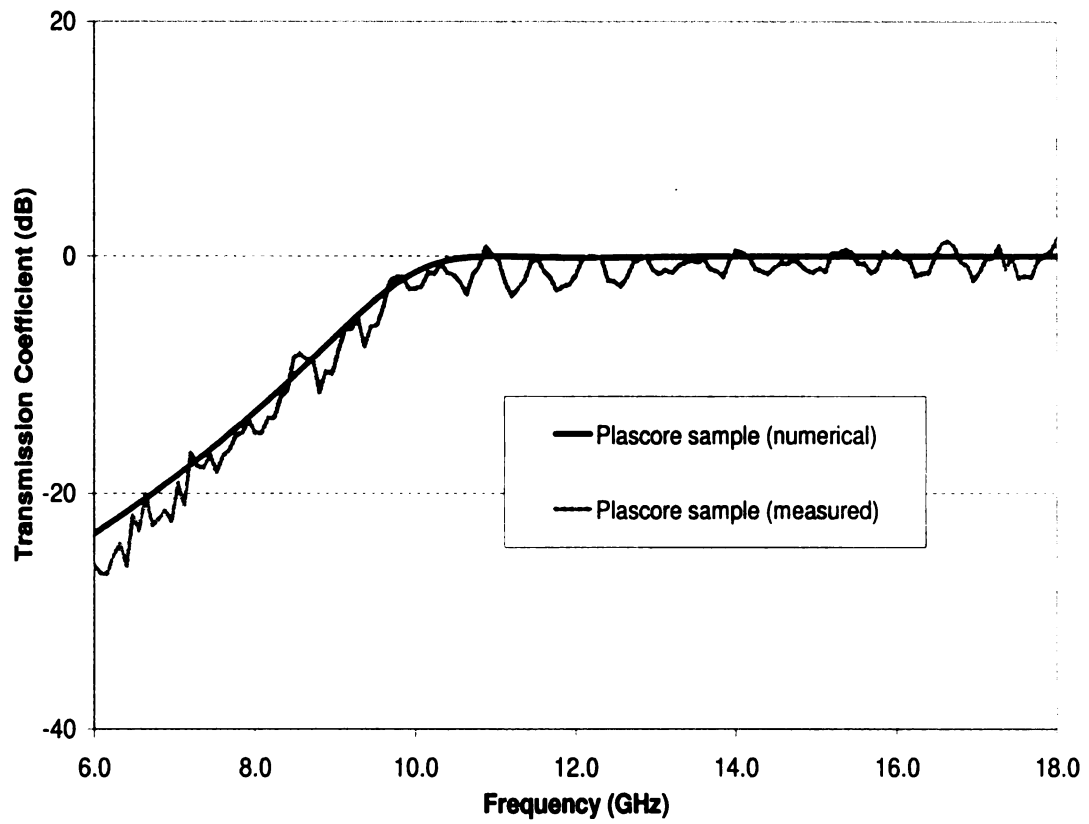Figure 4.4. Comparison of numerical and experimental results for rectangular apertures

Figure 4.5. Comparison of numerical and experimental results for hexagonal apertures

CHAPTER 5

DISCUSSION OF MODE SELECTION

One of the major obstacles in this research was determining why the shielding calculation does not produce useful results for 60 waveguide modes when the screen thickness exceedes 6.6 mm. Originally, the matrix equation was solved using Gaussian Elimination [33]. When the convergence problems arose, Singular Value Decomposition (SVD) [33] was used in order to determine if the increase in thickness caused the square matrix in the matrix equation to become badly conditioned. This was accomplished by computing the condition number of the square matrix versus frequency for all of the thickness values of interest. According to [33], the matrix is badly conditioned once the condition number of the matrix exceeds the accuracy of the computer, which is about 10^{15}. Figure 5.1 shows a plot of the condition number versus frequency for a variety of thickness values, where 60 waveguide modes and 882 Floquet modes were used in each case. There is no absolute threshold where having a condition number lower than that point leads to meaningful solutions. However, at the highest thickness values, the condition number is well past the values that produce useful results. Further, increasing the thickness of the screen does make the condition number higher when using 60 waveguide modes. An attempt was made to use SVD in order to discard small singular values in order to improve matrix conditioning, but the solutions were not any better than before. To deal with the problem, the condition number of the square matrix was reduced by considering less waveguide modes for very thick screens. Modes were removed in order of highest cut-off frequency. The concern was that a significant amount of accuracy would be lost by taking that approach. However, Figure 5.2 shows that for the case of the 4.4 mm thick screen, the use of 60 waveguide modes provides virtually the same result as the use of several

other combinations of waveguide modes, including using only the 2 dominant modes. This would seem to suggest that the use of 60 modes is unnecessary. However, it should be stated that the need to disregard higher-order modes arises from the fact that the increase in thickness attenuates those modes so severely that they need to be removed from consideration. Figure 5.3 shows that even with 60 waveguide modes, the condition number never exceeds 10^{15} for the 4.4 mm thickness case. As was stated before, 10^{15} appears to be a value such that if the condition number is well below that value, the shielding effectiveness calculations will converge. If the condition number far exceeds that value, the calculations generally do not converge.

For the case of the 6.6 mm and 7.7 mm thick screens, a point should be made. Figure 5.4 indicates that the shielding effectiveness converges for all choices of number of waveguide modes used when the thickness is 6.6 mm. Also, Figure 5.6 shows that the shielding effectiveness results do not converge for the 7.7 mm case when using 60 or 40 waveguide modes, but they do converge for 30 or less. However, an interesting observation is that Figure 5.7 shows a condition number at or above 10^{20} for the 7.7 mm thickness when using 60 modes, while 40 modes leads to condition numbers between 10^{13} and 10^{15}. Meanwhile, Figure 5.5 shows condition numbers of between 10^{16} and 10^{19} for the 6.6 mm thickness when using 60 modes. So, despite the fact that the 7.7 mm case with 40 modes has a lower condition number than the 6.6 mm case with 60 modes, the former does not produce practical data while the latter does. This reemphasizes the point that while the condition number does give some indication of how the thickness is affecting the solution of the matrix equation, an absolute point where having a lower or higher condition number guarantees a convergent result was not found.

More examples of the effect of reducing the number of waveguide modes on the convergence of the shielding computation are shown in Figure 5.8 - Figure 5.12 for thicknesses of 8.8 mm, 9.9 mm, 18.0 mm, 26.0 mm, and 40.0 mm. The vertical scales

were adjusted to include the most information possible, but some curves were not included. For example, the 60 waveguide mode case for 9.9 mm thickness is not included in Figure 5.9 because it deviated too much from the curves shown in the figure.
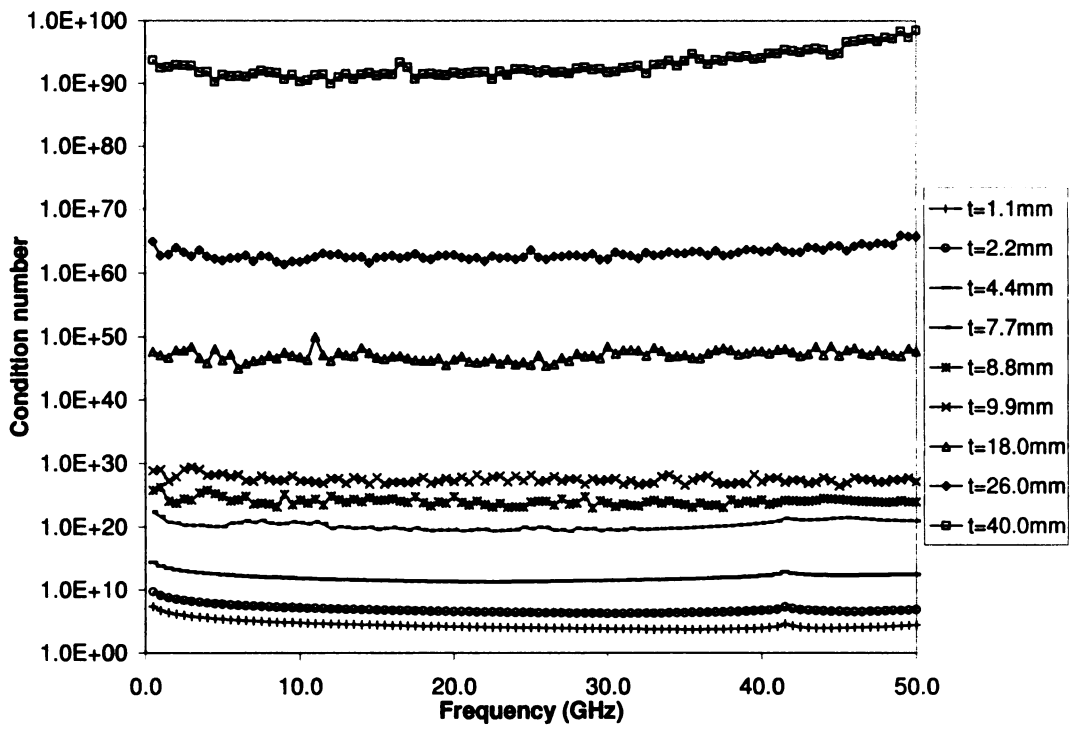
Figure 5.1. Condition number versus frequency for several values of thickness when using 60 waveguide modes and 882 Floquet modes.
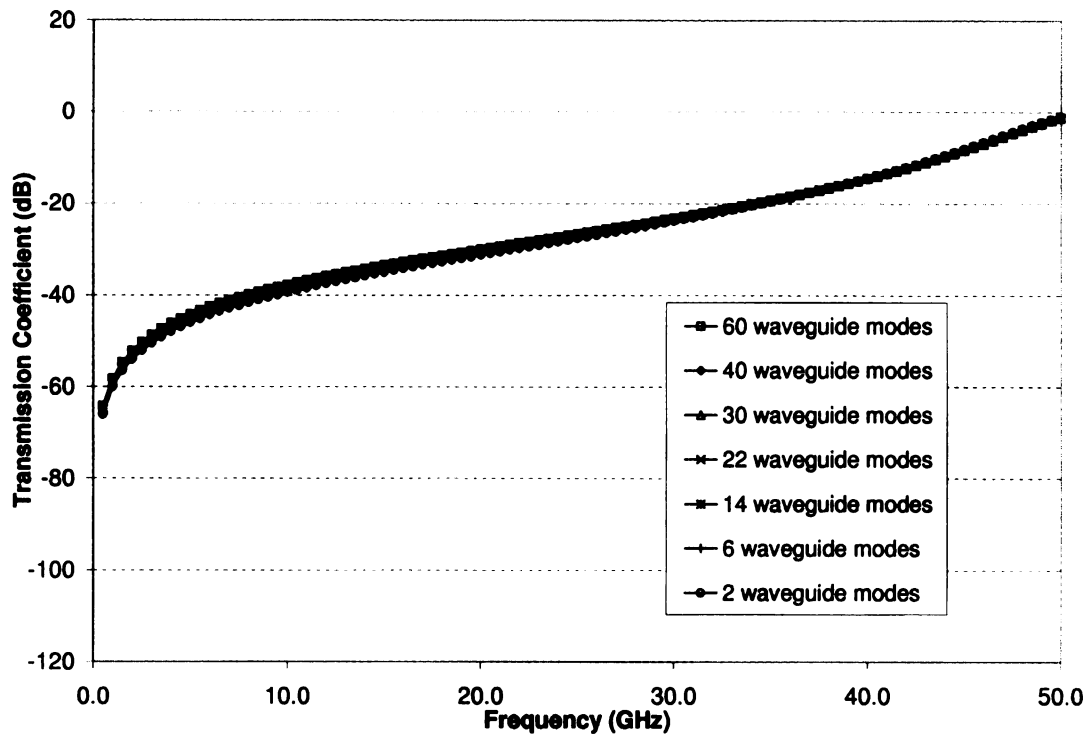
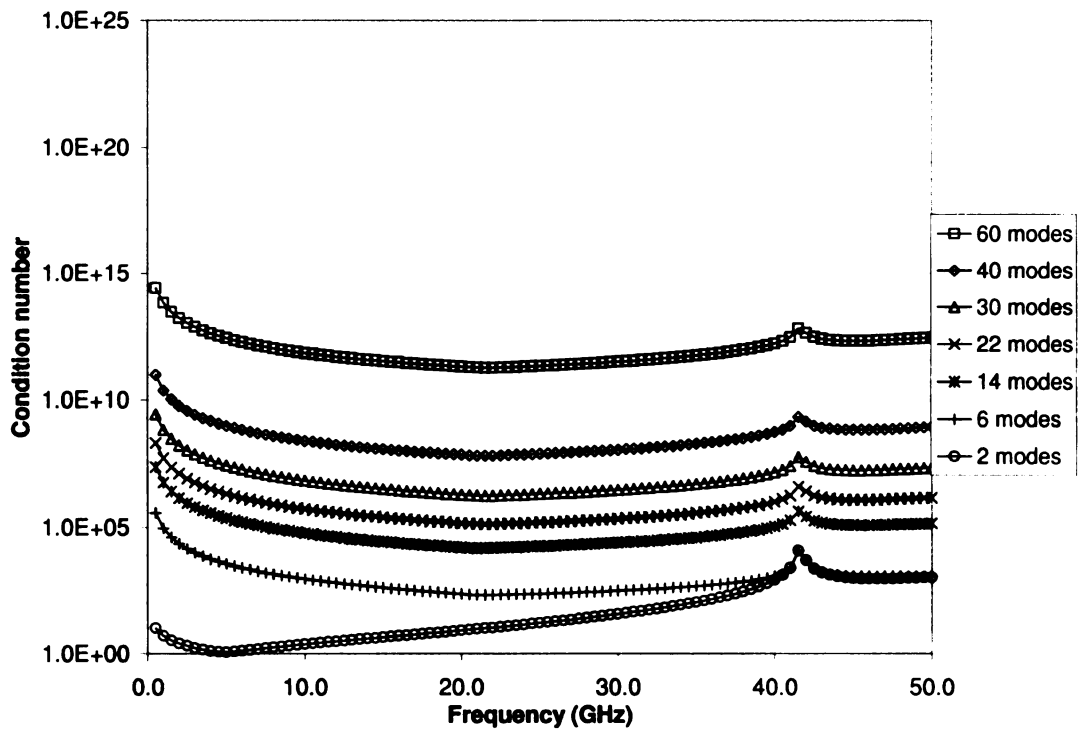Figure 5.2. Plot of shielding effectiveness for t=4.4 mm when varying the number of waveguide modes used.

Figure 5.3. Plot of condition number for t=4.4 mm when varying the number of waveguide modes used.
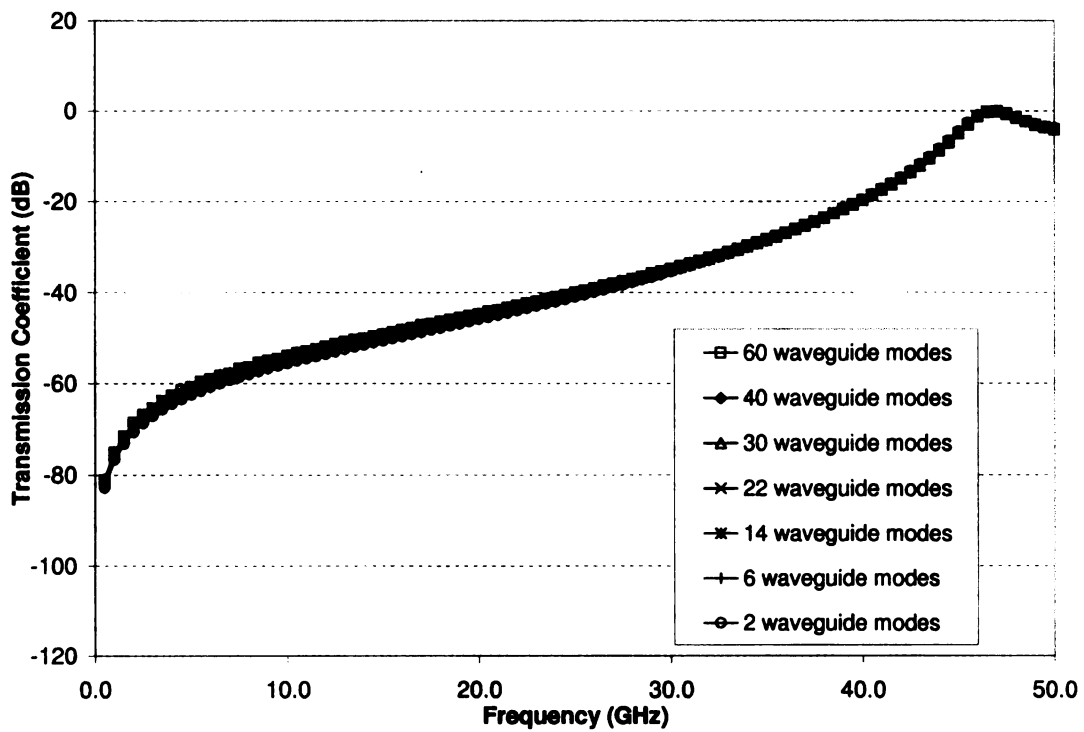
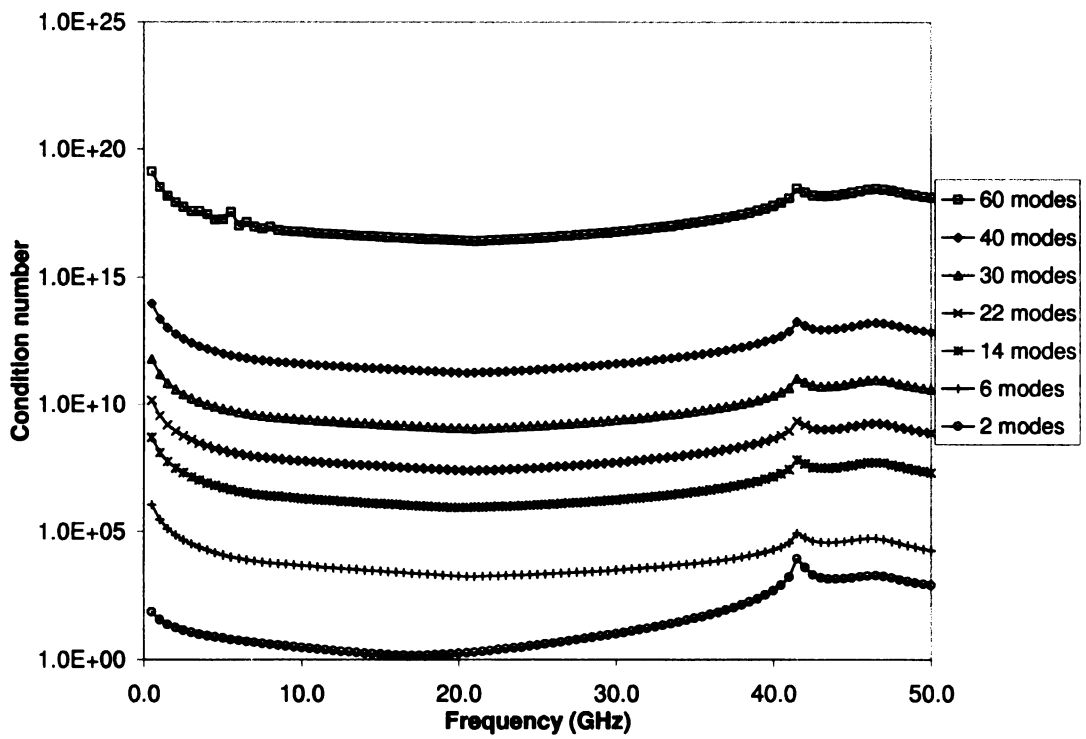Figure 5.4. Plot of shielding effectiveness for t=6.6 mm when varying the number of waveguide modes used.

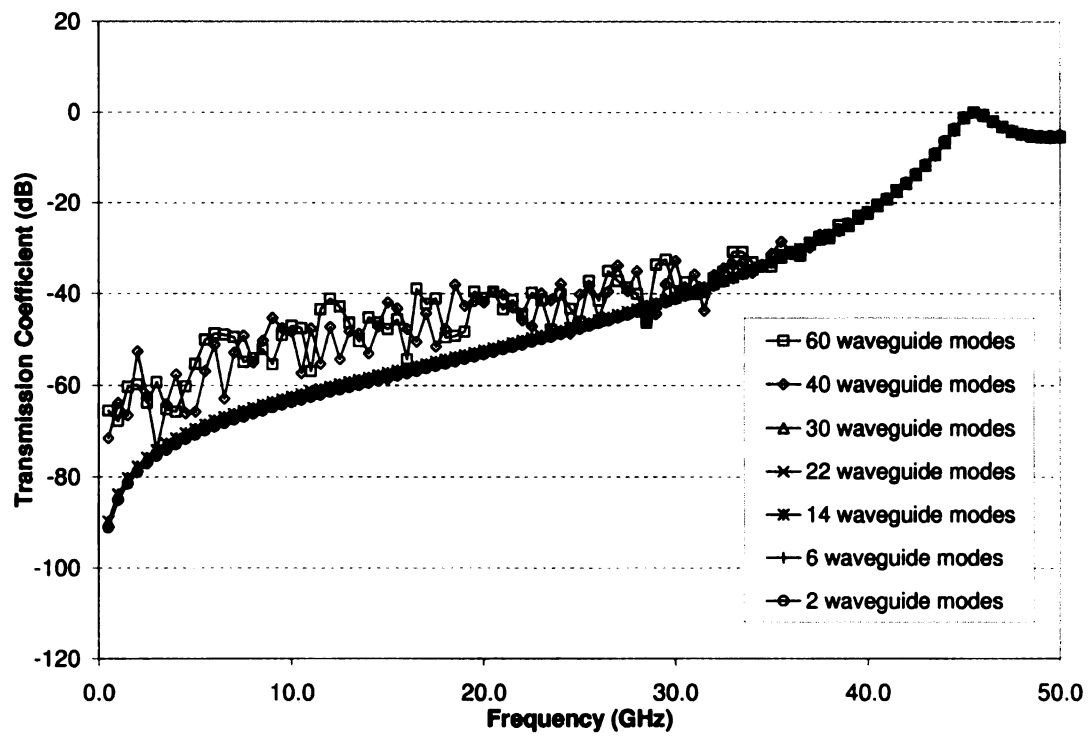Figure 5.5. Plot of condition number for t=6.6 mm when varying the number of waveguide modes used.

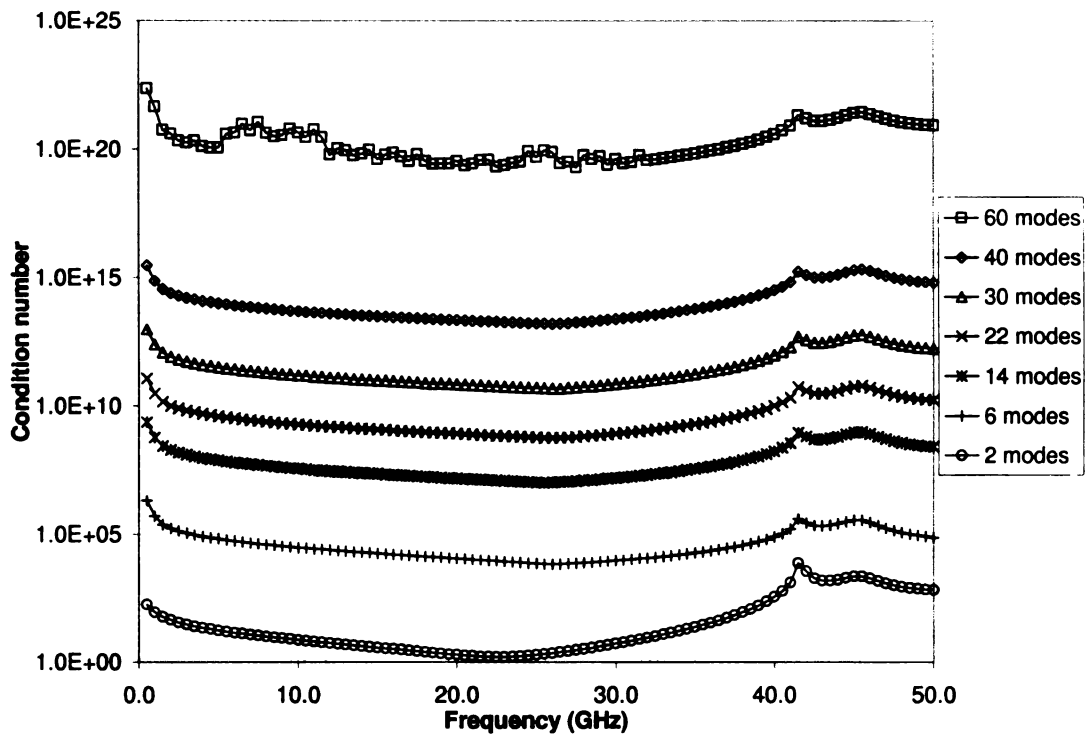Figure 5.6. Plot of shielding effectiveness for t=7.7 mm when varying the number of waveguide modes used.

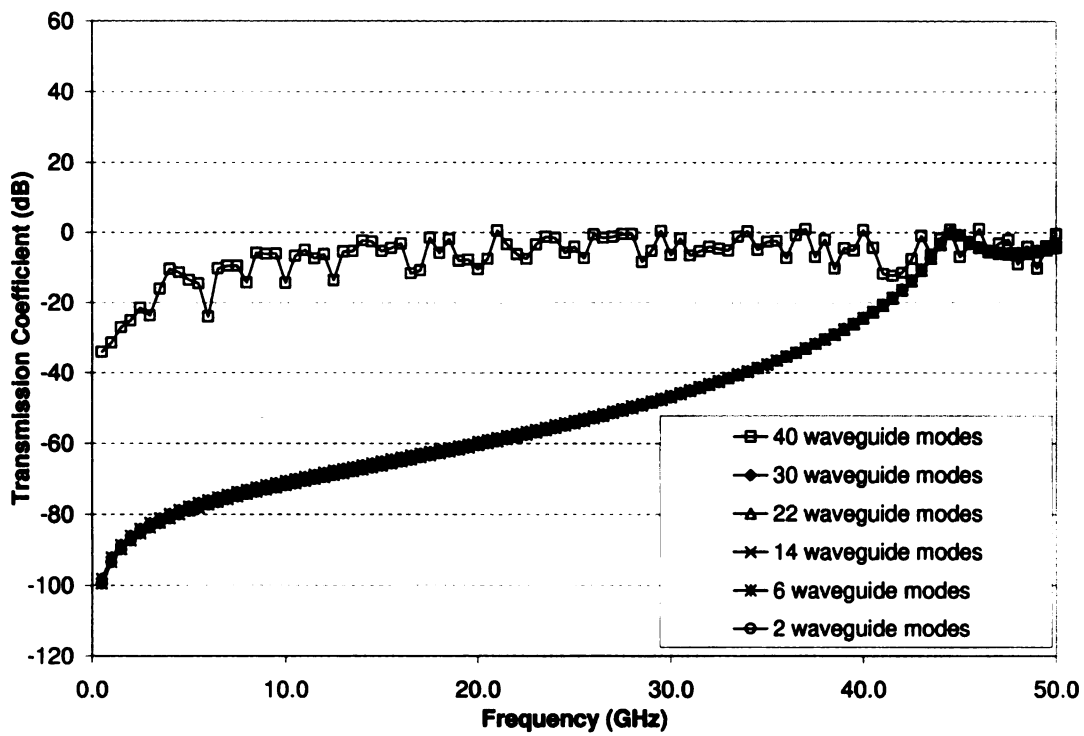Figure 5.7. Plot of condition number for t=7.7 mm when varying the number of waveguide modes used.

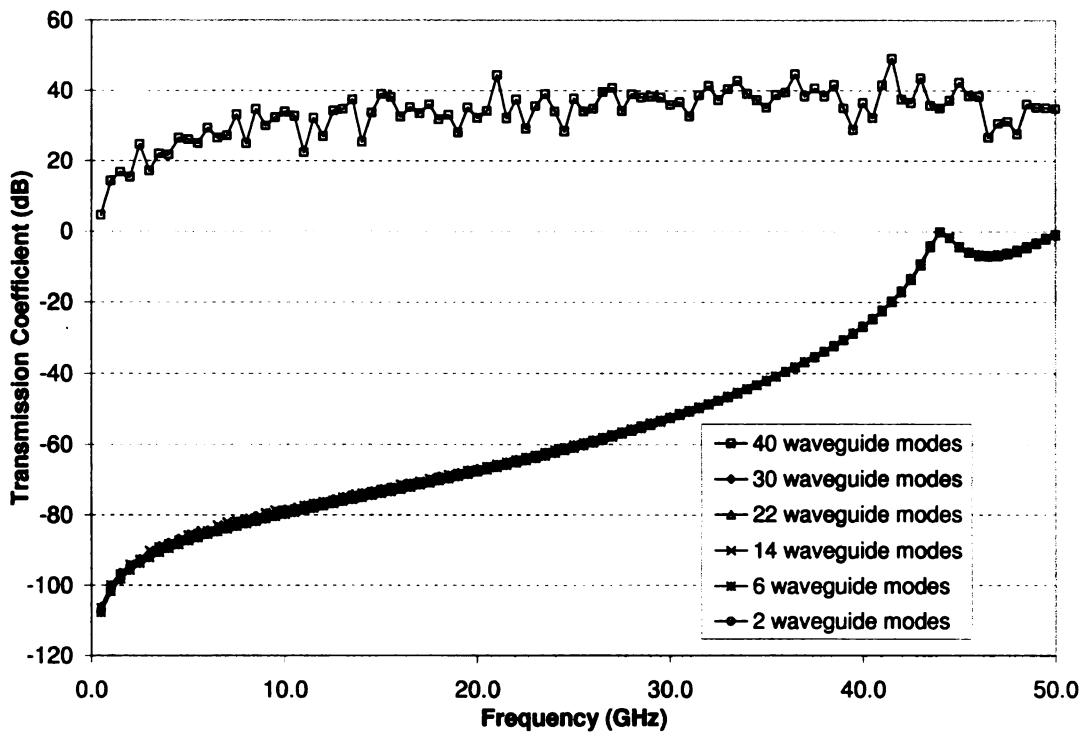Figure 5.8. Plot of shielding effectiveness for t=8.8 mm when varying the number of waveguide modes used.

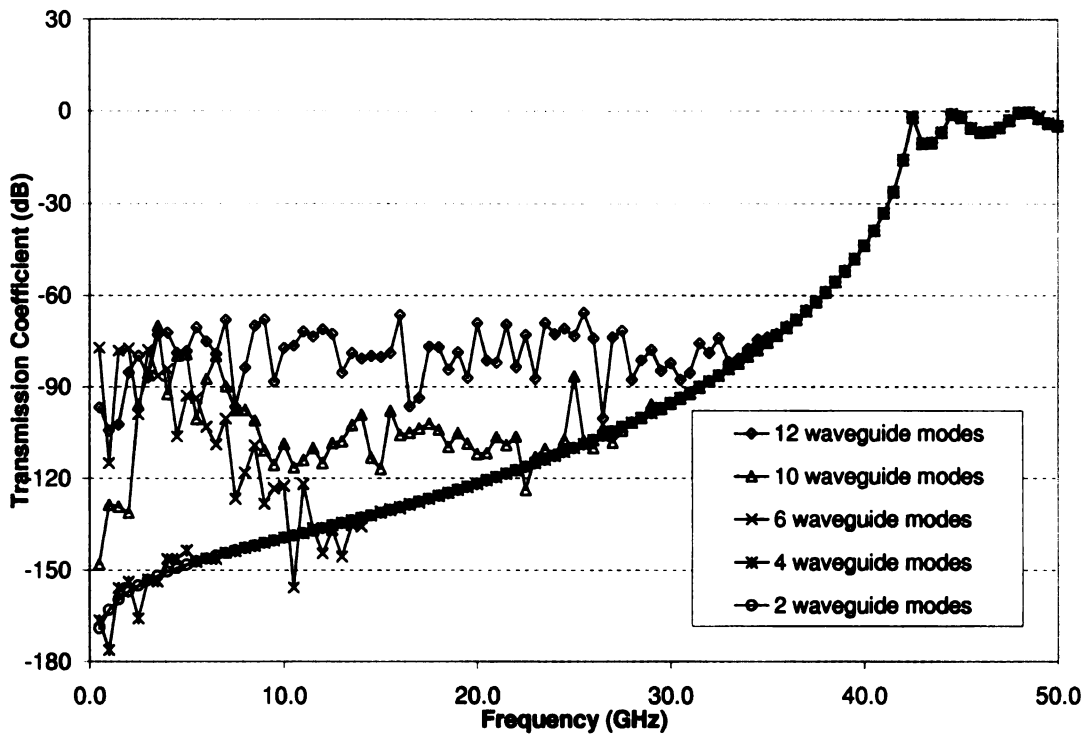Figure 5.9. Plot of shielding effectiveness for t=9.9 mm when varying the number of waveguide modes used.

Figure 5.10. Plot of shielding effectiveness for t=18.0 mm when varying the number of waveguide modes used.
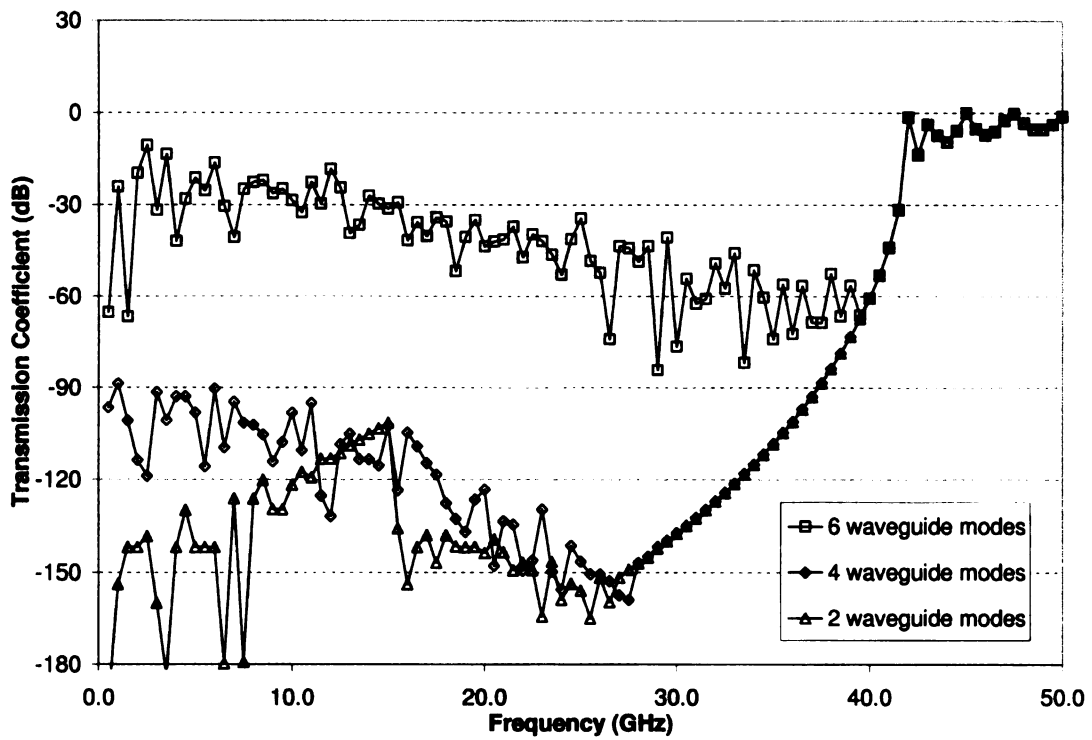
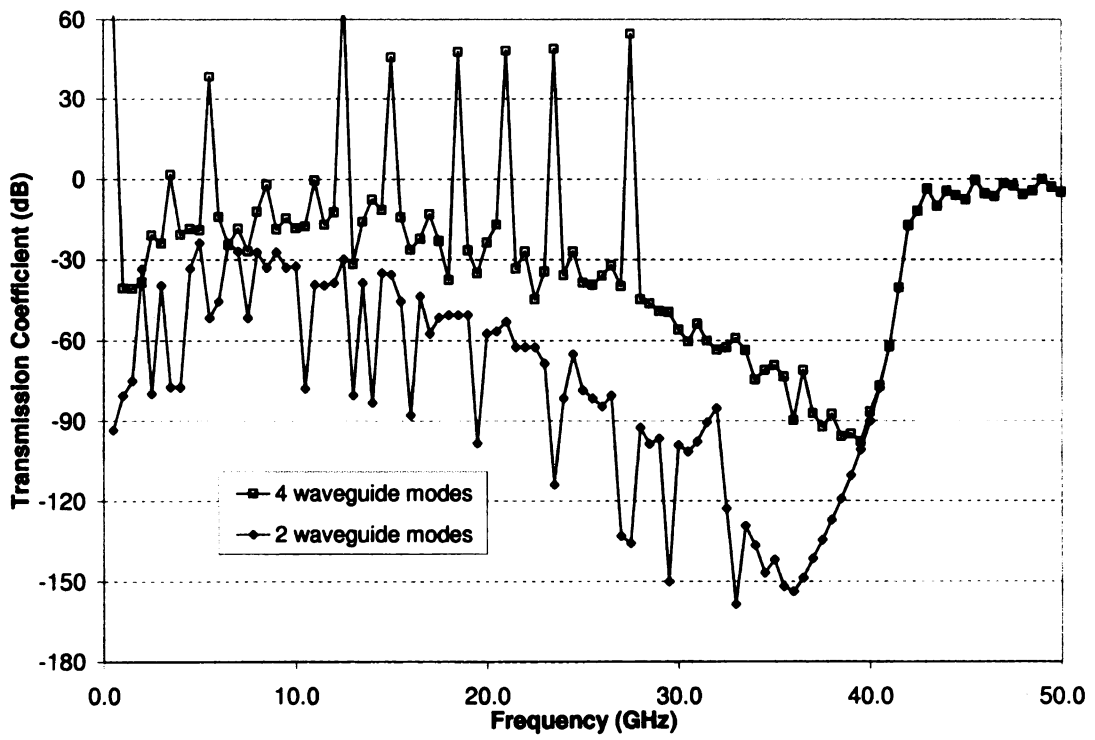Figure 5.11. Plot of shielding effectiveness for t=26.0 mm when varying the number of waveguide modes used.

Figure 5.12. Plot of shielding effectiveness for t=40.0 mm when varying the number of waveguide modes used.

CHAPTER 6

CONCLUSIONS

A mode-matching approach for computing the shielding effectiveness of a doubly-periodic array of apertures in a thick conducting screen has been presented. The effect of choosing thicknesses much larger than the aperture is the expected result of lower transmission of power. Mode-matching has shown some agreement with the waveguide below cutoff formula and strong agreement with other published results using mode-matching. The technique does suffer from an inability to yield meaningful data when the thickness is increased to a point where inaccurate solutions are produced. The use of Singular Value Decomposition led to the conclusion that the condition number is well beyond the accuracy of the computer when the thickness is increased a great deal. To produce useful and accurate solutions, the number of waveguide modes included in the analysis is reduced, which also reduces the condition number.

This dissertation considers mode-matching applied to apertures that are rectangular and circular in shape. Future work will consider hexagonal and other shapes for aperture arrays in thick screens. The shielding prediction is more flexible than the waveguide below cutoff approach, and the result is more exact. Other benefits include observance of the Wood's anomaly, a strong reliance on the well-known principles of waveguide theory, and practical application to the prediction of shielding performance of aluminum honeycomb and other doubly-periodic structures.

The measurements performed as part of this study were successful in confirming some of the results that were predicted numerically. Future work will be done in order to measure the effects of changing the incidence angle, predicting the occurrence and overall effect of the Wood's anomaly, determining the impact of using smaller and

larger sample sizes, and using other measurement techniques.

APPENDICES

APPENDIX A

DERIVATION OF 2-D FOURIER SERIES REPRESENTATION OF A PERIODIC FUNCTION IN SKEWED COORDINATES

Following the method of [34], a Fourier Series expansion is applied to a periodic potential function in a skewed coordinate system. Figure A.1 shows a lattice configuration with periodicity in two directions, one along the y-axis and the other along a direction at an angle θ with respect to the y-axis. If $\boldsymbol{r}$ is defined as

$$\boldsymbol{r} = l_1\boldsymbol{d}_1 + l_2\boldsymbol{d}_2,$$

where l_1 and l_2 are integers, and $\boldsymbol{d}_1$ and $\boldsymbol{d}_2$ are vectors describing the direct lattice, the reciprocal lattice can be defined by the vectors $\boldsymbol{b}_1$ and $\boldsymbol{b}_2$, and they must obey

$$\boldsymbol{b}_i \cdot \boldsymbol{d}_k = \delta_{ik}, \qquad i, k = 1, 2$$

or

$$\boldsymbol{b}_1 \perp \boldsymbol{d}_2$$

and

$$\boldsymbol{b}_2 \perp \boldsymbol{d}_1.$$

Letting

$$\boldsymbol{d}_1 = d_{1x}\hat{x} + d_{1y}\hat{y},$$

$$\boldsymbol{d}_2 = d_{2x}\hat{x} + d_{2y}\hat{y},$$

$$\boldsymbol{b}_1 = b_{1x}\hat{x} + b_{1y}\hat{y},$$

$$\boldsymbol{b}_2 = b_{2x}\hat{x} + b_{2y}\hat{y},$$

and

$$D = \begin{bmatrix} d_{1x} & d_{1y} \\ d_{2x} & d_{2y} \end{bmatrix} \qquad \text{row vectors,} \qquad (A.1)$$

$$B = \begin{bmatrix} b_{1x} & b_{2x} \\ b_{1y} & b_{2y} \end{bmatrix} \qquad \text{column vectors,} \qquad (A.2)$$

then

$$\begin{aligned} DB &= \begin{bmatrix} d_{1x}b_{1x} + d_{1y}b_{1y} & d_{1x}b_{2x} + d_{1y}b_{2y} \\ d_{2x}b_{1x} + d_{2y}b_{1y} & d_{2x}b_{2x} + d_{2y}b_{2y} \end{bmatrix} \qquad (A.3) \\ &= \begin{bmatrix} \boldsymbol{d_1} \cdot \boldsymbol{b_1} & \boldsymbol{d_1} \cdot \boldsymbol{b_2} \\ \boldsymbol{d_2} \cdot \boldsymbol{b_1} & \boldsymbol{d_2} \cdot \boldsymbol{b_2} \end{bmatrix} \\ &= \begin{bmatrix} 1 & 0 \\ 0 & 1 \end{bmatrix}. \end{aligned}$$

Therefore,

$$B = D^{-1},$$

and any point $\boldsymbol{r}$ in the x-y plane can be described using coordinates (ξ_1, ξ_2) such that

$$\boldsymbol{r} = \xi_1 \boldsymbol{d_1} + \xi_2 \boldsymbol{d_2}$$

where

$$\xi_1 = \boldsymbol{r} \cdot \boldsymbol{b_1}, \qquad (A.4)$$

$$\xi_2 = \boldsymbol{r} \cdot \boldsymbol{b_2}. \qquad (A.5)$$

A periodic function $F(x, y)$ in the direct lattice has the same value at the points $\boldsymbol{r} = (x, y)$ and $\boldsymbol{r'} = \boldsymbol{r} + l_1 \boldsymbol{d_1} + l_2 \boldsymbol{d_2}$, where l_1 and l_2 are integers. The Fourier Series

Representation of $F(x, y)$ in skewed coordinates is obtained by using

$$F(x, y) = f(\xi_1, \xi_2) = \sum_{m,n} c_{mn} e^{-2\pi j(m\xi_1 + n\xi_2)}, \qquad (A.6)$$

where m and n are integers, c_{mn} are the Fourier series coefficients, and f has a period of unity in (ξ_1, ξ_2) coordinates. Substituting (A.4) and (A.5) into (A.6) leads to

$$F(x, y) = \sum_{m,n} c_{mn} e^{-2\pi j[m(\boldsymbol{b}_1 \cdot \boldsymbol{r}) + n(\boldsymbol{b}_2 \cdot \boldsymbol{r})]} \qquad (A.7)$$

or

$$F(x, y) = \sum_{m,n} c_{mn} e^{-2\pi j[\boldsymbol{h} \cdot \boldsymbol{r}]},$$

where

$$\boldsymbol{h} = m\boldsymbol{b}_1 + n\boldsymbol{b}_2.$$

Since $dxdy = S_d d\xi_1 d\xi_2$, where S_d is the unit cell area, the Fourier coefficients c_{mn} are found using

$$c_{mn} = \frac{1}{S_d} \int_S F(x, y) e^{+2\pi j[\boldsymbol{h} \cdot \boldsymbol{r}]} dxdy.$$

Using Figure A.2, which was adopted from [19], (A.1) can be rewritten as

$$D = \begin{bmatrix} d_1 & 0 \\ d_2 \cos \phi_0 & d_2 \sin \phi_0 \end{bmatrix} \qquad (A.8)$$

Substituting the elements from (A.8) into (A.3) leads to

$$d_1 b_{1x} + 0 = 1 \Rightarrow b_{1x} = \frac{1}{d_1},$$

$$d_1 b_{2x} + 0 = 0 \Rightarrow b_{2x} = 0,$$

$$d_2 \cos \phi_0 b_{1x} + d_2 \sin \phi_0 b_{1y} = 0 \Rightarrow b_{1y} = \frac{-1}{d_1} \cot \phi_0,$$

114

$$d_2 \cos\phi_0 b_{2x} + d_2 \sin\phi_0 b_{2y} = 1 \Rightarrow b_{2y} = \frac{1}{d_2 \sin\phi_0} = \frac{1}{d_2}\csc\phi_0.$$

Rewriting $\boldsymbol{b}_1$ and $\boldsymbol{b}_2$ gives

$$\boldsymbol{b}_1 = \frac{1}{d_1}\hat{x} - \frac{1}{d_1}\cot\phi_0\hat{y},$$

$$\boldsymbol{b}_2 = \frac{1}{d_2}\csc\phi_0\hat{y},$$

and using those results in (A.3) leads to

$$DB = \begin{bmatrix} d_1 & 0 \\ d_2\cos\phi_0 & d_2\sin\phi_0 \end{bmatrix} \begin{bmatrix} \frac{1}{d_1} & 0 \\ \frac{-1}{d_1}\cot\phi_0 & \frac{1}{d_2}\csc\phi_0 \end{bmatrix}$$

$$= \begin{bmatrix} 1 & 0 \\ 0 & 1 \end{bmatrix}.$$

(A.7) can now be expressed as

$$\begin{aligned}
F(x,y) &= \sum_{m,n} c_{mn} e^{-2\pi j[m(\boldsymbol{b}_1\cdot\boldsymbol{r}) + n(\boldsymbol{b}_2\cdot\boldsymbol{r})]} \\
&= \sum_{m,n} c_{mn} e^{-2\pi j\left[m\left(\left(\frac{1}{d_1}\hat{x} - \frac{1}{d_1}\cot\phi_0\hat{y}\right)\cdot\boldsymbol{r}\right) + n\left(\left(\frac{1}{d_2}\csc\phi_0\hat{y}\right)\cdot\boldsymbol{r}\right)\right]} \\
&= \sum_{m,n} c_{mn} e^{-2\pi j\left[\frac{m}{d_1}x - \frac{m}{d_1}\cot\phi_0 y + \frac{n}{d_2}\csc\phi_0 y\right]}.
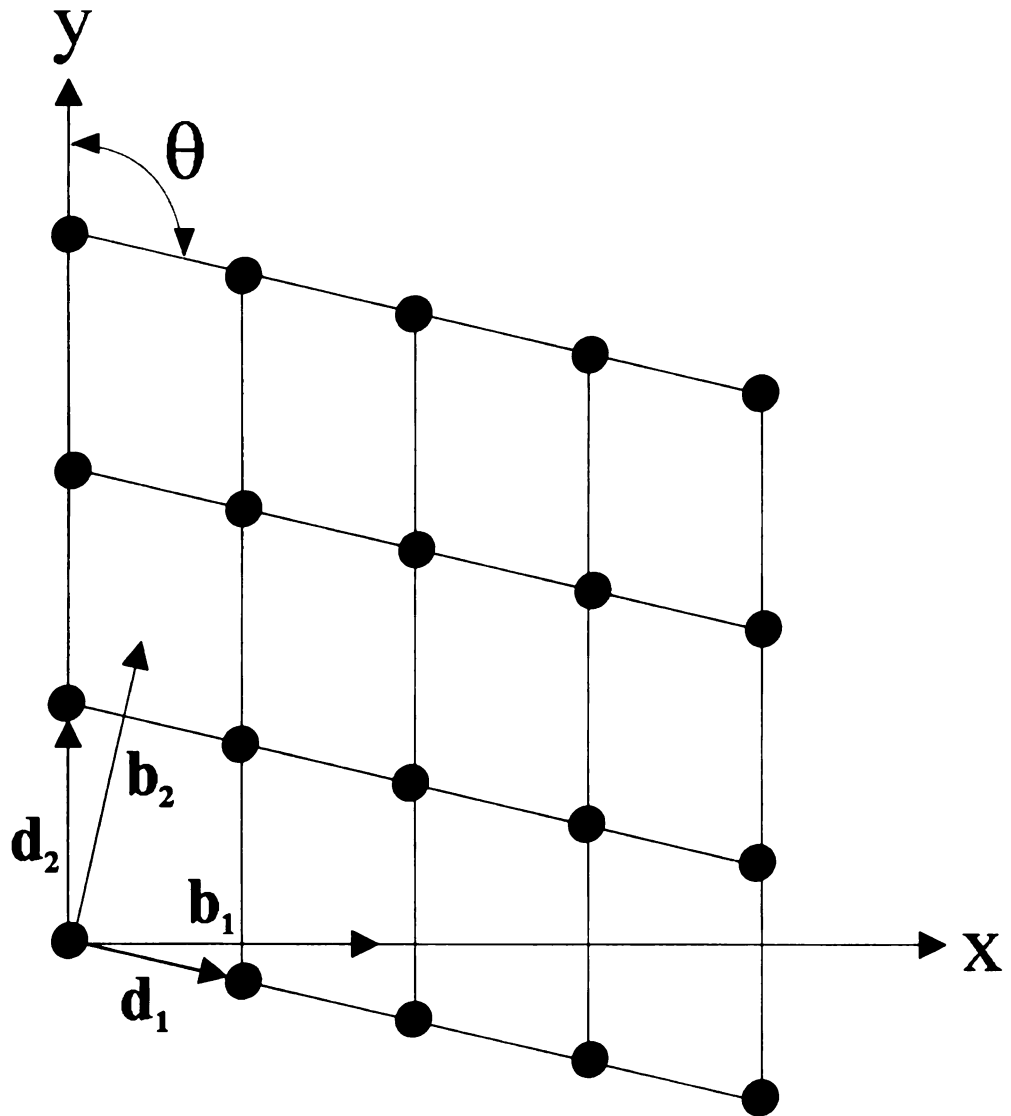\end{aligned}$$

Figure A.1. Doubly-periodic direct lattice

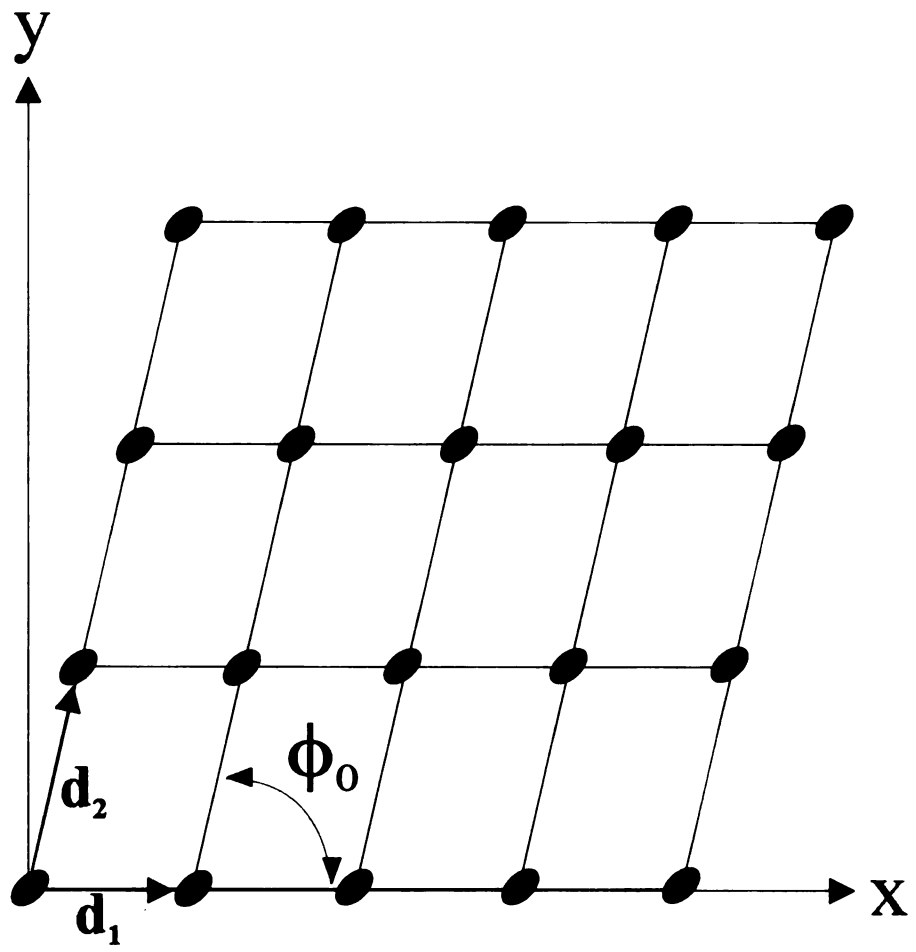Figure A.2. Alternate description of doubly-periodic lattice

BIBLIOGRAPHY

BIBLIOGRAPHY

[1] G. F. Koch and K. S. Kölbig, "The transmission coefficient of elliptical and rectangular apertures for electromagnetic waves," *IEEE Trans. Antennas Propagat.*, vol. AP-16, pp. 78–83, Jan. 1968.

[2] C. J. Bouwkamp, "Theoretical and numerical treatment of diffraction through a circular aperture," *IEEE Trans. Antennas Propagat.*, vol. AP-18, pp. 152–176, Mar. 1970.

[3] J.-L. Lin, W. L. Curtis, and M. C. Vincent, "On the field distribution of an aperture," *IEEE Trans. Antennas Propagat.*, vol. AP-22, pp. 467–471, May 1974.

[4] Y. Rahmat-Samii and R. Mittra, "Electromagnetic coupling through small apertures in a conducting screen," *IEEE Trans. Antennas Propagat.*, vol. AP-25, pp. 180–187, Mar. 1977.

[5] C. C. Chen, "Transmission through a conducting screen perforated periodically with apertures," *IEEE Trans. Microwave Theory Tech.*, vol. MTT-18, pp. 627–632, Sept. 1970.

[6] ——, "Diffraction of electromagnetic waves by a conducting screen perforated periodically with circular holes," *IEEE Trans. Microwave Theory Tech.*, vol. MTT-19, pp. 475–481, May 1971.

[7] S. W. Lee, "Scattering by dielectric-loaded screen," *IEEE Trans. Antennas Propagat.*, vol. AP-19, pp. 656–665, Sept. 1971.

[8] C. C. Chen, "Transmission of microwave through perforated flat plates of finite thickness," *IEEE Trans. Microwave Theory Tech.*, vol. MTT-21, pp. 1–6, Jan. 1973.

[9] R. J. Luebbers and B. A. Munk, "Some effects of dielectric loading on periodic slot arrays," *IEEE Trans. Antennas Propagat.*, vol. AP-26, pp. 536–542, July 1978.

[10] B. J. Rubin, "Scattering from a periodic array of apertures or plates where the conductors have arbitrary shape, thickness, and resistivity," *IEEE Trans. Antennas Propagat.*, vol. AP-34, pp. 1356–1365, Nov. 1986.

[11] A. Roberts and R. C. McPhedran, "Bandpass grids with annular apertures," *IEEE Trans. Antennas Propagat.*, vol. 36, pp. 607–611, May 1988.

[12] H. H. Park and H. J. Eom, "Electromagnetic scattering from multiple rectangular apertures in a thick conducting screen," *IEEE Trans. Antennas Propagat.*, vol. 47, pp. 1056–1060, June 1999.

[13] T. K. Sarkar, M. F. Costa, C.-L. I, and R. F. Harrington, "Electromagnetic transmission through mesh covered apertures and arrays of apertures in a conducting screen," *IEEE Trans. Antennas Propagat.*, vol. AP-32, pp. 908–913, Sept. 1984.

[14] T. Wang, R. F. Harrington, and J. R. Mautz, "Electromagnetic scattering from and transmission through arbitrary apertures in conducting bodies," *IEEE Trans. Antennas Propagat.*, vol. 38, pp. 1805–1814, Nov. 1990.

[15] J.-M. Jin and J. L. Volakis, "Electromagnetic scattering by and transmission through a three-dimensional slot in a thick conducting plane," *IEEE Trans. Antennas Propagat.*, vol. 39, pp. 543–550, Apr. 1991.

[16] R. Luebbers and C. Penney, "Scattering from apertures in infinite ground planes using FDTD," *IEEE Trans. Antennas Propagat.*, vol. 42, pp. 731–736, May 1994.

[17] J. H. Oates, R. T. Shin, and M. J. Tsuk, "Small aperture modeling for EMI applications using the finite-difference time-domain technique," *J. Electromag. Waves Appl.*, vol. 9, pp. 37–69, 1995.

[18] M. Angeli and E. Cardelli, "Numerical analysis of diffracting perforated shields," *IEEE Trans. Magn.*, vol. 33, pp. 1472–1475, Mar. 1997.

[19] B. Widenberg, S. Poulsen, and A. Karlsson, "Scattering from thick frequency selective screens," *J. Electromag. Waves Appl.*, vol. 14, pp. 1303–1328, 2000.

[20] H.-C. Chu and C. H. Chen, "Shielding and reflection properties of periodic fiber-matrix composite structures," *IEEE Trans. Electromagn. Compat.*, vol. 38, pp. 1–6, Feb. 1996.

[21] H.-K. Chiu, H.-C. Chu, and C. H. Chen, "Propagation modeling of periodic laminated composite structures," *IEEE Trans. Electromagn. Compat.*, vol. 40, pp. 218–224, Aug. 1998.

[22] H. Rogier, B. Baekelandt, F. Olyslager, and D. DeZutter, "The FE-BIE technique applied to some 2-D problems relevant to electromagnetic compatibility: Optimal choice of mechanisms to take into account peridocity," *IEEE Trans. Electromagn. Compat.*, vol. 42, pp. 246–256, Aug. 2000.

[23] C. R. Paul, *Introduction to Electromagnetic Compatibility.* New York: John Wiley & Sons, 1992.

[24] L. H. Hemming, "Applying the waveguide below cut-off principle to shielded enclosure design," in *Proc. IEEE Int. Symp. on Electromagnetic Compatibility*, Aug. 17–21, 1992, pp. 287–289.

[25] E. J. Rothwell and M. J. Cloud, *Electromagnetics.* Boca Raton, Florida: CRC Press, 2001.

[26] S. S. Soliman and M. D. Srinath, *Continuous and Discrete Signals and Systems*. Englewood Cliffs, New Jersey: Prentice-Hall, 1990.

[27] S. Ramo, J. Whinnery, and T. Van Duzer, *Fields and Waves in Communication Electronics*. New York: John Wiley & Sons, 1994.

[28] R. F. Harrington, *Time-Harmonic Electromagnetic Fields*. New York: McGraw-Hill, 1961.

[29] R. E. Collin, *Field Theory of Guided Waves*. New York: McGraw-Hill, 1960.

[30] H. L. Bertoni, L.-H. S. Cheo, and T. Tamir, "Frequency-selective reflection and transmission by a periodic dielectric layer," *IEEE Trans. Antennas Propagat.*, vol. 37, pp. 78–83, Jan. 1989.

[31] A. Kurtz, "Electromagnetic material characterization using free field transmission measurements," Master's thesis, Michigan State University, East Lansing, MI, 1997.

[32] P. F. Wilson, M. T. Ma, and J. W. Adams, "Techniques for measuring the electromagnetic shielding effectiveness of materials: Part I: Far-field source simulation," *IEEE Trans. Electromagn. Compat.*, vol. 30, pp. 239–250, Aug. 1988.

[33] W. H. Press, S. A. Teukolsky, W. T. Vetterling, and B. P. Flannery, *Numerical Recipes in FORTRAN: The Art of Scientific Computing*. New York: Cambridge University Press, 1992.

[34] L. Brillouin, *Wave Propagation in Periodic Structures; Electric Filters and Crystal Lattices*. New York: Dover Publications, 1953.